Nickel Isotope Geochemistry in Mine Waste Systems

by

Roberta Parigi

A thesis

presented to the University of Waterloo

in fulfillment of the

thesis requirement for the degree of

Doctor of Philosophy

in

Earth and Environmental Sciences

Waterloo, Ontario, Canada, 2020

Examining Committee Membership

The following served on the Examining Committee for this thesis. The decision of the Examining Committee is by majority vote.

External Examiner	Dr. David Borrok Professor
Supervisor(s)	Dr. David Blowes Professor
Internal Member	Dr. Carol Ptacek Professor
Internal-external Member	Dr. Vassili Karanassios Professor
Other Member(s)	Dr. Richard Amos Assistant Professor

AUTHOR'S DECLARATION

This thesis consists of material all of which I authored or co-authored: see Statement of Contributions included in the thesis. This is a true copy of the thesis, including any required final revisions, as accepted by my examiners.

I understand that my thesis may be made electronically available to the public.

Statement of contributions

This thesis consists of a series of manuscripts either submitted or prepared for submission to peer-reviewed journals. As the first author of each paper, I was responsible for designing and conducting experiments, collecting samples for analysis, interpreting analytical results and writing the papers. Contributions for each chapter are summarized as below:

Chapter 1: This chapter was written solely by Roberta Parigi.

Chapter 2: The experiments were designed and conducted solely by Roberta Parigi with input from David Blowes and Carol Ptacek. Ni isotope method development and analysis were done by Roberta Parigi. Synchrotron-based PXRD analysis was performed by Roberta Parigi, whereas Joel Reid processed the PXRD data. XAS analysis was primarily conducted by Roberta Parigi. EXAFS data processing was done by Roberta Parigi under Ning Chen's supervision. Roberta Parigi interpreted analytical results and wrote the manuscript. All co-authors provided comments and edits to the manuscript.

Chapter 3: The experiments were designed by Roberta Parigi, Eva Pakostova, and Joyce McBeth and conducted by Roberta Parigi, with input from David Blowes and Carol Ptacek. Ni isotope method development and analysis were done by Roberta Parigi. Synchrotron-based PXRD analysis was performed by Joyce McBeth's students, whereas Joel Reid processed the PXRD data. Emily Saurette primarily conducted SEM-EDS analysis. Emily Saurette conducted TEM analysis. Roberta Parigi interpreted analytical results and wrote the manuscript with feedback from all co-authors.

Chapter 4: The experiment was designed and conducted by Roberta Parigi with input from David Blowes and Carol Ptacek. Ni isotope method development and analysis were done by Roberta Parigi. XAS analyses were performed primarily by Roberta Parigi. EXAFS data were processed and interpreted by Ning Chen. Peng Liu handled the micro-XRF data. Roberta Parigi

analyzed the results and wrote the paper. All co-authors provided comments and edits to the manuscript.

Chapter 5: The sample collection was conducted by Roberta Parigi, Jeff Bain, Justin Buis, and other assistants. Ni isotope method development and analysis were done by Roberta Parigi. Laboratory work on core samples was performed by Roberta Parigi and Justin Buis. Roberta Parigi processed Ni-K edge XANES, whereas Emily Saurette processed S-K edge XANES and performed LCF on both S and Ni spectra. Roberta Parigi analyzed the results and wrote the paper. All co-authors provided comments and edits to the manuscript.

Chapter 6: This chapter was written solely by Roberta Parigi.

Abstract

Metal stable isotope analyses have proven to make valuable contributions to the study of the biogeochemical cycling of metals and metalloids in the environment. Processes that control the release, mobility and fate of metals in natural systems often lead to stable isotope fractionation. Before the isotopic signatures of natural samples can be applied as environmental tracers, laboratory-scale studies, focused on the measurement of the magnitude of the isotope fractionation associated with specific processes, are needed. Despite recent studies, Ni stable isotope systematics is still in its infancy, thus further research is required to decipher Ni isotope signatures in complex, natural systems.

Nickel, similar to other metals, is a nutritionally essential trace element for several organisms and plants, however the exposure to highly Ni-polluted environments can result in a variety of pathological effects in living organisms. Some of the Ni compounds are also classified as carcinogenic, thus, the investigation of Ni attenuation processes is of great importance to protect living beings and the environment.

Laboratory batch experiments were conducted to characterize the isotope fractionation during the precipitation of Ni secondary mineral phases: Ni hydroxide, Ni hydroxycarbonate and Ni sulfide. Data were best represented by Rayleigh-type curves, showing fractionation factors $\varepsilon_{\text{Ni-hydroxide}} = -0.40‰$, $\varepsilon_{\text{Ni-hydroxycarbonate}} = -0.50‰$ and, $\varepsilon_{\text{Ni-sulfide}} = -0.73‰$. These values indicate a preferential retention of lighter Ni isotopes by the solid phase in all three systems. Synchrotron-based Powder X-ray diffraction (PXRD), and X-ray absorption spectroscopy (XAS) analyses were performed to characterize the precipitates. The interpretation of isotope results suggests that equilibrium effects are the main mechanisms responsible for the measured Ni isotopic signatures.

As bacterial reduction of sulfate under anaerobic conditions has been successfully applied to the treatment of waste streams contaminated by heavy metals, laboratory batch experiments were performed to evaluate isotopic fractionation of Ni during microbially-mediated Ni sulfide precipitation. The final solid product was characterized by Scanning electron microscopy (SEM), Transmission electron microscopy (TEM), Synchrotron-based Powder X-ray diffraction (PXRD) and X-ray absorption spectroscopy (XAS). The measured isotope data relative to the fraction of Ni in solution and the fraction of Ni associated with the solid phase followed a linear trend which yielded a $\Delta^{60}_{\text{solid-solution}} = -1.99‰$, with lighter Ni isotopes partitioned into the precipitates. Both the results of the solid-phase and isotope analyses suggest a combination of Ni removal mechanisms, including complexation, precipitation, co-precipitation and sorption, thus complicating the interpretation of the isotope data.

Previous studies involving calcite interaction with Ni have shown the potential of calcium carbonate in the sequestration of Ni from impacted aquatic and groundwater environments. A flow-through cell experiment was conducted to assess Ni isotopic fractionation during Ni treatment by calcite. Synthetic Ni-contaminated groundwater was pumped through a custom-made flow-through cell containing crushed natural calcite. Measurements oh pH were conducted on the effluent and aqueous samples were collected for determination of the concentrations of anions and cations and Ni isotope analyses. X-ray absorption spectroscopy (XAS) was performed via a Kapton window in the cell to gather information on the speciation of Ni in the system. Confocal X-ray microfluorescence imaging (CMXFI) analysis was also conducted on Ni-bearing calcite particles from the cell to further characterize the mechanisms of Ni removal. Results indicate that there are multiple processes controlling Ni removal by calcite inside the flow-through cell, and that greater enrichment of

^{60}Ni over ^{58}Ni in the effluent compared to the input solution, is associated with higher rates of Ni removal.

Nickel isotope analysis was conducted on pore water samples extracted from the Moose Lake tailings impoundment as a supportive tool in the characterization of the processes controlling Ni mobility in the tailings within the ML 25 storage facility which are subject to sulfide mineral oxidation. Samples of the tailings material were analyzed using multiple analytical techniques including transmitted and reflected microscopy, X-ray fluorescence, and synchrotron based X-ray absorption spectroscopy (XAS). The highest Ni concentration (578.9 mg L^{1}) in pore water was found to coincide with the depth of the front of active sulfide-mineral oxidation, whereas highest Ni concentrations in the tailings solid material (1473 and 5000 mg kg^{-1}) corresponded to the highest peaks in sulfur content. Results show a good correlation between Ni isotopic signatures of the pore water and the weathering zones characteristic of different depths of the tailings impoundment, thus suggesting the potential of Ni stable isotopes as tracers in environmental geochemistry.

Acknowledgements

Foremost, I would like to express my deep gratitude to Prof. David Blowes, my supervisor, and Prof. Carol Ptacek, my non-official co-supervisor, for their support, broad knowledge, enthusiastic encouragement, and useful critiques of this research work. Their passion for research is inspiring, and I am indebted to them for the opportunities they have provided me. Working in their research group was a great, fulfilling experience!

I would also like to thank Prof. Richard Amos, my committee member, for his time and availability, and also for the insightful comments during the meetings.

Funding for this research was provided by the Natural Sciences and Engineering Research Council of Canada (NSERC) Strategic Grant awarded to D.W. Blowes and C.J. Ptacek, the Natural Sciences and Engineering Research Council of Canada Strategic Partnership Grants for Networks, Toward Environmentally Responsible Resource Extraction Network (NSERC TERRE-NET, NETGP 479708-15) and an Ontario Research Fund Research Excellence Fund grant awarded to D.W. Blowes, C.J. Ptacek, and R.T. Amos. Synchrotron-based techniques were performed at Sector 20 BM and Sector 20 ID at the Advanced Photon Source (APS) and at HXMA, SXRMB, and CMCF beamlines of the Canadian Light Source (CLS). This project used resources of the APS, a U.S. Department of Energy (DOE) Office of Science User Facility operated for the DOE Office of Science by Argonne National Laboratory. CLS is supported by the Canada Foundation for Innovation, NSERC, the University of Saskatchewan, the Government of Saskatchewan, Western Economic Diversification Canada, the National Research Council Canada, and the Canadian Institutes of Health Research. I received funding from the CLS Graduate Student Travel Support Program.

I thank Dr. Ning Chen, Dr. Joel Reid, and Dr. Zou Finfrock for their invaluable support in synchrotron-related parts of this research. I am so grateful I had the chance to work with you.

Many thanks to Dr. Joyce McBeth, Dr. Matt Lindsay, and some of their students for the help provided with syncrothron PXRD analysis and sample storage during my visits to the University of Saskatchewan and CLS.

Thank you to all of the technicians, graduate students, postdocs, researchers, and coop students for assistance in the field and laboratories. In particular, I would like to thank Laura Groza and Joy Hu for being so helpful in research-related and not research-related matters. Thank you to Jeff Bain for always being prompt to help me out with technical and analytical aspects of my study.

I thank past and present GGR members for the stimulating discussions, and the amazing time spent together, in particular Alana Ou Wang, Ying Ying Liu, Peng Liu, Lingyi Kong, Jane Eagling, and Joanne Angai. Huge thanks goes to Heather Shrimpton who took care of the Neptune and taught me a lot about it. I learnt so much from your problem-solving skills. Without assisting you in the clean lab I would not even know what an Allen key is!

I would especially like to thank my fellow labmates and colleagues Justin Buis, Filip Budimir, Emily Saurette, Eva Pakostova, and David Wilson for all the fun we had in the past years. You made my Canadian life so enjoyable! You will always be welcome wherever I will be.

Special thanks to Stephen Romaniello for his broad knowledge and invaluable advice on MC-ICP-MS analysis coupled with the use of APEX-Q desolvator system. You have been my “deus ex machina”!

Warmest thanks to Giuseppe Loglio, a scientist, a professor, and a friend, who always supported me and believed in my science-related potential. I really enjoyed our stimulating conversations about science, and ancient Greek and Latin cultures. I would be happy to become half the scientist you are. You are such an inspiration.

My profound thanks are extended to my parents, sister, grandparents and pets for all the love and support they provided even when we were apart. Thanks also to my parents-in-law who supported and visited us during our Canadian stay.

Finally, I am sincerely grateful to my husband, Adriano, for his support, patience and understanding. You gifted me with the most precious gem: our sweet daughter Electra. You two spice up my life every day and fill it with happiness and love.

Dedication

To Oreste S., Iris, and Maria

my beloved grandparents:

and to Kiba

my dear dog

Table of Contents

List of Figures

List of Tables

List of Abbreviations

SIC	Sudbury igneous comples
DOM	Dissolved organic matter
AMD	Acid mine drainage
PRB	Permeable reactive barrier
PXRD	X-ray powder diffraction
XAS	X-ray absorption spectroscopy
SEM	Scanning electron microscopy
EDS	Energy-dispersive X-ray spectroscopy
TEM	Transmission electron microscopy
SRB	Sulfate-reducing bacteria
FTC	Flow-through cell
EXAFS	Extended X-ray absorption fine structure
XRF	X-ray fluorescence
XANES	X-ray absorption near edge structure
SPE	Solid phase extraction
DMG	Dimethylglyoxime
MC-ICP-MS	Multi-collector inductively coupled plasma mass spectrometry
CLS	Canadian Light Source
CMCF	Canadian Macromolecular Crystallography Facility
HXMA	Hard X-ray microanalysis
CN	Coordination number
σ^2	Debye-Waller parameter
R	Interatomic distance
ΔE^0	Energy offset parameter
SDD	Silicon drift detector
BSE	Back-scattered electron
SE	Secondary electron
FFT	Fast Fourier Transform
Å	Angstrom
EPS	Extracellular polymeric substances
HDPE	High-density polyethylene
ZVI	Zero-valent iron
BET	Brunauer, Emmett and Teller
XAFS	X-ray absorption fine structure
CMXRFI	Confocal micro-X-ray fluorescence imaging
APS	Advanced Photon Source
ML	MooseLake
SXRMB	Soft X-Ray Microcharacterization Beamline
TEY	Total electron yield
PFY	Partial fluorescent yield

CHAPTER 1

Introduction

1.1. INTRODUCTION TO NICKEL

Although unintentional use of Ni has been observed since ancient times (Sigel et al., 2007), Ni was discovered and first described in the Acts of the Royal Academy of Sciences at Stockholm in the 1750's by Cronstedt (Cronstedt, 1770). The name "nickel", which refers to a German evil spirit called Old Nick, probably originated from the name "kupfernickel" that German workers gave to niccolite (NiAs), because the mineral looked like copper but they couldn't get any copper from it (Hausinger, 1993; Sigel et al., 2007). Subsequently, Ni was first isolated by the French geologist Berthier in the early 1800's (Hausinger, 1993).

Nickel has many industrial and commercial applications. It is used in electroplating, electroforming and it is also a constituent of nickel-cadmium batteries and electronic equipment. Nickel also can be found in coins, jewellery and medical prostheses (Denkhaus & Salnikow, 2002). However, the largest use of Ni is the production of stainless steel and other Ni-based alloys characterized by a high corrosion and temperature resistance properties (Sigel et al., 2007; Coman et al., 2013). Due to the vast utilization of Ni-containing products, nickel ores are extensively mined in several countries.

1.1.1. Nickel ores

Nickel is the 24th most abundant element in the Earth crust (Alloway, 1995) and, although constituting about 0.0086% of the crust itself, it is mainly located in the core (at a concentration of 5.8%) and in the mantle (at a concentration of 0.22%) regions of the Earth (Hausinger, 1993).

Nickel is an element with chalcophilic affinities, therefore it is often found associated with sulfur, arsenic and antimony in nature (e.g., NiS, NiAs, $NiAs_{2-3}$, NiAsS, NiSb, NiSbS)(Sigel et al., 2007).

Nickel ores consist of two different types of economically important deposits: sulfide ores and laterites (Betteridge, 1984; Sigel et al., 2007).

- *Sulfide ores*

Major Ni sulfide deposits are related by key aspects involving their genesis: (i) a source of sulfur that saturates the magma, (ii) gravitational segregation of the immiscible sulfide liquid and (iii) concentration of the sulfides in restricted areas (e.g. physical traps or conduits) (Naldrett, 1999; Lightfoot, 2007; Naldrett, 2004).

The Ni-bearing sulfide minerals characteristic of sulfide ores are principally pentlandite [$(Ni,Fe)_9S_8$] and nickeliferous pyrrhotite [roughly $(Ni,Fe)_7S_8$]. Occasionally, millerite (NiS), hazlewoodite (Ni_3S_2) and violarite [$(Ni,Fe)_3S_4$] can also be found (Burkin, 1987). Copper and iron sulfides such as chalcopyrite ($CuFeS_2$) and pyrite (FeS_2) are always present in association with the Ni sulfide minerals (Burkin, 1987).

- *Laterites*

Nickel laterites originate from an intense weathering of olivine-rich ultramafic rocks and their serpentinized equivalents (containing up to 0.4 % on Ni), during which, Ni is taken into solution and then redeposited as complex oxides, hydroxides or silicates (Betteridge, 1984; Butt & Cluzel, 2013).

Most of Ni-laterite deposits consist of two principal units: a lower silicate-rich unit, named saprolite), rich in Mg and Ni-bearing phyllosilicates, and an upper oxide-rich unit, characterized by Ni-bearing iron (oxyhydr)oxides (essentially goethite) and Ni/Co manganese oxides (Dublet et al., 2015).

Although Ni laterites represent 60 to 70% of the world's nickel resources, until 2000 they accounted for less than 40% of global nickel production, due to lower ore grades, complex treatment processes, pricy energy requirements and distance from industrial centers and proper infrastructure (Butt & Cluzel, 2013). Recently, though, as a result of increasing demand, the discovery of new technologies and the decreasing availability of sulfide ores, the production from nickel laterites has increased, exceeding 50% in 2010 (Butt & Cluzel, 2013).

1.1.1.1. Sudbury

Sudbury (Ontario, Canada) is the largest Ni deposit and, along with Noril'sk (Russia) it is also the main Ni producer of the world (Lightfoot, 2007). The discovery of Sudbury Ni-Cu ores dates back to the construction of the Canadian Pacific transcontinental railway that reached Sudbury in 1883 (Naldrett, 2004; Rousell & Brown, 2009), and some of the Sudbury mines have been in continuous operations for 100 years (Lightfoot, 2007).

The Sudbury igneous complex (SIC), dated 1.85 Ga, is an elliptical rock body produced by the impact of a meteorite (Lightfoot, 2007). Impact melting of one of the mafic/ultramafic intrusions dated 2.45 Ga, and the incorporation of the melt in the overall impact melt, could be the cause of the high Ni, Cu and S contents of the SIC (Naldrett, 2004; Rousell & Brown, 2009). Therefore Sudbury Ni deposits are characterized by a unique interconnection of several factors: meteorite-impact, crustal melting, differentiation of a sulfide-saturated magma, segregation of the sulfides and remobilization into the footwall of the SIC (Lightfoot, 2007).

The Ni-Cu ore deposits of the Sudbury area are associated to: (i) SIC-footwall contact deposits, (II) footwall vein deposits, (iii) offset dike deposits, and (iv) sheared deposits (Naldrett, 2004; Rousell & Brown, 2009).

The Strathcona deposit is a typical contact deposit situated in the North Range marginal (contact) deposits. The main zone ore occurs within the footwall breccias and in the footwall fractures (Naldrett, 2004). The Creighton mine is an example of a South Range contact deposit

and it is one of the longest-lived of the Sudbury mines (production started at the beginning of the 20th century). The Creighton mine is also the deepest Ni mine in the world (2500 m) (Naldrett, 2004).

The major sulfide minerals characterizing the Sudbury sulfide ore bodies are pyrrhotite, pentlandite, chalcopyrite and lesser pyrite, while magnetite is an important accessory mineral (Abel et al., 1979; Duke & Naldret, 1976; Peredery, 1990).

1.1.2. Nickel in the environment

Nickel belongs to the transition metal group 10 of the periodic table and its electronic configuration is (Ar) $3d^8$ $4s^2$. Nickel is typically found in the II+ oxidation state, even though the 0, I+ and III+ oxidation states occur under certain circumstances. As Ni easily loses two electrons, Ni^{2+} is the most dominant species in the Eh-pH range of natural waters, even though, in the presence of DOM (dissolved organic matter), Ni is known to form strong complexes with organic ligands (Sigel et al., 2007; Doig & Liber, 2007).

Dissolved Ni^{2+} at neutral pH shows an octahedral structure with six water ligands in the first coordination shell $[Ni(H_2O)_6]^+$ (Liu et al., 2012). Along with the octahedral and tetragonally distorted octahedral structures, which are the most common geometries in the aqueous environment, square planar and tetrahedral arrangements may also occur (Sigel et al., 2007).

Despite natural geological processes, such as weathering and volcanic activity, which cause Ni to be modestly accumulated in natural environments, the sources of Ni contamination are principally related to anthropogenic causes, such as the production and processing of Ni and its by-products, the combustion of fossil fuels, the recycling of Ni-bearing products and disposal of Ni-containing waste (Denkhaus & Salnikow, 2002; Schaumlöffel, 2012).

1.1.2.1. Acid mine drainage

Sulfide minerals are one of the major sources of metals that are commercially extracted (Mason, 2013). The most significant impact of sulfide ore mining operations is the generation

of acid mine drainage which is commonly associated with waste rock and tailings deposition in sub-aerial storage facilities (Gunsinger et al., 2006; Lindsay et al., 2009; Blowes et al., 2014). Acid mine drainage (AMD) is a consequence of the oxidation of sulfide minerals present in mine waste, mill tailings and overburden (Blowes et al., 1991; Evangelou, 1995; Blowes et al., 2014). The dominant sulfide minerals related to mine waste and tailings are pyrite and pyrrhotite, although others can be affected by oxidation too, generating low-pH water, rich in dissolved elements such as Ni, Al, As, Co, Cu, Zn, and Pb that can migrate out of the mine waste and tailings impoundment into nearby water bodies, contaminating them (Blowes et al., 2014; Gunsinger et al., 2006; Moncur et al., 2009).

The oxidation of pyrite and pyrrhotite by atmospheric O_2 can be written respectively as:

$$FeS_{2(s)} + \frac{7}{2}O_2 + H_2O \rightarrow Fe^{2+} + 2SO_4^{2-} + 2H^+$$

$$Fe_{1-x}S_{(s)} + (2 - 0.5x)O_2 + xH_2O \rightarrow (1 - x)Fe^{2+} + SO_4^{2-} + 2xH^+$$

Fe^{2+} can further oxidize to Fe^{3+} resulting in the precipitation of Fe(III) minerals such as goethite [α-FeOOH] and jarosite [$KFe_3(SO_4)_2(OH)_6$] leading to the production of H^+ (Gunsinger et al., 2006). Pyrite and pyrrhotite oxidation by Fe^{3+} is also possible, but the presence of O_2 is fundamental in sustaining the oxidation to Fe^{3+} (Blowes et al., 2014). Additionally, in acidic solution, nonoxidative dissolution of pyrrhotite may also occur (Gunsinger et al., 2006).

The role played by microorganisms colonizing mine-impact waters into the sulfide oxidation processes, is summarized in Table 1.1.

Table 1.1: Common iron- and sulfur-oxidizing prokaryotes that found in mine-impacted waters (Reproduced with permission from Blowes et al., 2014).

	Oxidation of Fe^{2+} S	Carbon assimilation[a]	pH range (approx.)	T-response	Other traits
Acidiferrobacter thiooxydans	+ +	A	1.2 to > 3	T	Reduction of Fe^{3+}
Acidimicrobium ferrooxidans	+ -	A/H	1.3 to > 3	T	Reduction of Fe^{3+}
Acidiphilium acidophilum	- +	A/H	1.5 to 6.5	M	Reduction of Fe^{3+}
Acidithiobacillus caldus	- +	A	1 to 4	T	Reduction of Fe^{3+}
Acidithiobacillus ferrivorans	+ +	A	1.9 to > 3	P	Reduction of Fe^{3+}
Acidithiobacillus ferrooxidans	+ +	A	1.3 to > 3	M	Reduction of Fe^{3+}
Acidithiobacillus thiooxidans	- +	A	0.5 to 5.5	M	Some strains are halotolerant
Ferrimicrobium acidiphilum	+ -	H	1.4 to > 3	M	Reduction of Fe^{3+}
Ferroplasma spp.	+ -	H	0.8 to > 2	T	Reduction of Fe^{3+}
Ferrovum myxofaciens	+ -	A	2 to > 4	P	Copious production of exopolymeric substances
L. ferrooxidans	+ -	A	1.3 to > 2	M	
L. ferriphilum	+ -	A	0.8 to >2	T	
Sulfobacillus spp.	+ +	A/H	1 to >3	T	Reduction of Fe^{3+}
Thiobacillus prosperus	+ +	A	1 to 4.5	M	Halophilic
Thiomonas spp.	- +	A/H	3 to 8	M (T, one species)	Some species oxidize As(III)

[a]Carbon assimilation: A=autotroph, H=heterotroph; T-response: P=psychrotolerant, M=mesophilic, and T=thermotolerant or moderately thermophilic.

A series of pH buffering reactions, involving dissolution of non-sulfide gangue minerals, can consume the acidity produced by sulfide oxidation, slowing down the transport of low-pH water flowing through the mine wastes. According to different studies involving acid neutralization mechanisms in mine tailings (Dubrovsky et al., 1985; Blowes et al., 1991; Johnson et al., 2000; Jurjovec et al., 2002; Blowes et al., 2014), a sequence of pH-buffering plateaus (pHs 6.5, 5.5, 4, and 2.8) has been identified and interpreted as a result of the successive dissolution of calcite, siderite, aluminum hydroxide and ferrihydrite (Johnson et al., 2000).

1.1.2.2. Permeable reactive barriers (PRBs)

Permeable reactive barriers are a recently developed technology used as an alternative to the traditional remediation approaches that usually involve the removal of the contaminant source, the 'Pump and Treat system' (P&T) or the confinement of the source area using low permeability barriers or covers (Blowes et al., 2000; Blowes et al., 2014). PRBs technologies require the emplacement of a permeable barrier made of reactive material across the migrating plume path in order to intercept and treat the contaminants affecting the groundwater (Blowes at al., 2000; Obiri-Nyarko et al., 2014).

The treatment of the contaminants is based on two main categories: (i) destructive biotic or abiotic processes (biodegradation or reductive dechlorination); (ii) non-destructive processes (adsorption, cation exchange, surface complexation, and precipitation) (Obiri-Nyarko et al., 2014).

Depending on the target contaminant, the effectiveness of various reactive materials has been the focus of many studies. Among these materials, the most frequently utilized are: Zero valent iron (ZVI), organic carbon, apatite, zeolites, clays, and calcite/limestone (Blowes et al., 2000; Striegel et al., 2001; Obiri-Nyarko et al., 2014).

Although permeable reactive barriers have been demonstrated to be an effective sustainable groundwater treatment, further research, concerning an in-depth understanding of the mechanisms involved using different reactive materials, is needed in order to improve the PRBs performance and duration over time.

1.1.3. Nickel toxicity

Nickel, in low concentration, is considered an essential micronutrient for plants (Ahmad & Ashraf 2011; Sreekanth et al. 2013; Fabiano et al. 2015) and microorganisms (Hausinger, 1987; Mulrooney & Hausinger, 2003), in contrast, the nutritional requirement for Ni in higher organisms is debatable (Denkhaus & Salnikow, 2002; Merril et al., 2007). Nonetheless, results

from rat experiments have reported that Ni deficiency could cause perinatal mortality, alterations of grooming behavior, liver development, and decreased growth, showing that Ni has an important role in the activity of many enzymes involved in carbohydrate and amino acid metabolism, in the adsorption of Fe from the intestine and in the synthesis of phospholipids (Denkhaus & Salnikow, 2002).

As with other heavy metals, high Ni concentrations can have harmful effects on plants and higher organisms. Excess of Ni has been documented to cause multiple deleterious effects to aquatic life. Blewett and Leonard (2017) reported the impairment of gas exchange, inhibition of ion regulation, and the promotion of oxidative stress as the main consequences of Ni toxicity to aquatic biota. Human exposure to Ni occurs principally via inhalation, ingestion and skin contact (Denkhaus & Salnikow, 2002; Schaumlöffel, 2012). Contact dermatitis, due to Ni allergy, is the most common adverse effect on humans (Denkhaus & Salnikow, 2002; Kasprzak et al., 2003; Schaumlöffel, 2012), however, cases of respiratory tract and nasal cancers have been observed in miners and workers in Ni refineries (Denkhaus & Salnikow, 2002). Furthermore, all Ni compounds included in the oxidic group (nickel oxides, nickel-copper oxide, nickel silicate oxides, and complex oxides), sulfidic group [nickel sulfide (NiS) and nickel subsulfide (Ni_3S_2)] and soluble group (nickel sulfate and nickel chloride), with the exception of the metallic form, are considered carcinogenic (Canadian Environmental Protection act, 2013). Research aimed to shed insights into the Ni cycle and to determine the bioavailability of Ni in natural systems is therefore needed to enhance control measures for Ni to prevent or moderate possible harmful effects on humans and the environment.

1.1.4. Nickel isotopes

Nickel has five stable isotopes: 58, the most abundant (68.077%), 60 (26.223%), 61 (1.1399%), 62 (3.6346%) and 64 (0.9255%). Nickel isotope analysis started getting attention during the first decade of the 2000 (Quitté & Oberli, 2006; Tanimizu & Hirata, 2006), and the first studies

focused almost exclusively on extraterrestrial materials (Cook et al., 2006; Cook et al., 2007; Chen et al., 2009). Since 2009 research on Ni stable isotopes has involved a variety of applications: Ni stable isotope investigations have been carried out on different types of terrestrial rocks (Gall et al., 2012, 2013, and 2017; Gueguen et al., 2013, and 2016) and vegetation (Estrade et al., 2015; Ratié et al., 2019; Zelano et al., 2020), on the influence of microbial activity (Cameron and Vance, 2009; Yang et al., 2020), on adsorption and co-precipitation processes (Wasylenki et al., 2015; Wang and Wasylenki, 2017; Gueguen et al., 2018; Castillo Alvarez et al., 2020; Sorensen et al., 2020), and on environmental samples (Hofmann et al., 2014; Ratié et al., 2015, 2016, 2018, and 2019; Spivak-Birndorf et al., 2018). Mass-dependent Ni isotope data ($\delta^{60/58}$Ni), associated with different geochemical reservoirs, and fractionation factors between co-existing phases ($\Delta^{60/58}Ni_{PhaseA\text{-}PhaseB}$) were compiled and reported by Elliott and Steele (2017).

Despite the recent advances in the characterization of Ni isotope fractionation applied to many scientific fields, Ni stable isotope systematics is still at an early stage of development. Further research, which aims to progress the application of Ni isotopes as biogeochemical tracers, is therefore needed.

1.2. THESIS STRUCTURE

This thesis is presented as a series of four research papers whose purpose is to shed insights into the use of Ni stable isotopes as environmental tracers. Ni stable isotope analysis was applied to discern the mechanisms and the geochemical processes involved in Ni attenuation at mine sites. Within this framework, the present thesis is organized around two main objectives: 1) measurement of Ni isotope fractionation during different removal scenarios and 2) the application of Ni stable isotope analysis to environmental samples.

The first research paper, which is presented as Chapter 2, consists of a series of batch experiments conducted to evaluate Ni isotope fractionation during the precipitation of secondary mineral phases (i.e., Ni hydroxide, Ni hydroxycarbonate and Ni sulfide) which contribute to the attenuation of Ni in the environment. Results from multiple techniques, such as Ni stable isotope determinations, synchrotron-based X-ray powder diffraction (PXRD) and X-ray absorption spectroscopy (XAS), were integrated to better characterize the three investigated systems.

Chapter 3 includes batch experiments performed to determine Ni isotope fractionation associated with microbially-mediated Ni removal from solution. Synchrotron-based PXRD, SEM-EDS, and TEM analyses were conducted to characterize the solid phase. Ni stable isotope signatures were measured on both the solution and the solid samples. Because sulfate reducing bacteria (SRB) provide a cost-effective alternative to traditional remediation methods, SRB culture are implemented in passive treatment techniques to promote the precipitation of heavy metals as sulfides.

Chapter 4 describes a flow-through cell (FTC) experiment conducted to evaluate Ni isotope fractionation during treatment by calcite under saturated flow conditions. Calcite is known to be involved in the scavenging of divalent metals, such as Ni, from the environment. Ni isotope measurements were conducted on effluent samples collected at different times throughout the

FTC experiment. EXAFS data collection was performed on different spots across the FTC Kapton window to detect the changes in Ni speciation during the experiment. Confocal micro-X-ray fluorescence imaging analysis was also conduced to acquire Ni spectra from different depths of single calcite particles collected from the FTC.

Chapter 5 presents the application of Ni stable isotope analysis to environmental samples. Evaluation of Ni isotope fractionation and investigation of Ni mineralogical and geochemical characteristics were conducted on mine tailings sampled at the Strathcona mine site. Ni isotope analysis was performed on pore water extracted from the tailings, whereas XRF, and carbon and sulfur analyses were conducted on tailings solid samples collected at different depths within the tailings impoundment. Tailings solid samples were also analyzed for Ni K-edge and S K-edge XANES to determine the sulfide weathering profile characterizing the impoundment.

Chapter 6 provides a summary of experimental results, scientific contributions, and descriptions of the environmental implications.

CHAPTER 2

Nickel isotope fractionation during precipitation of Ni secondary minerals and synchrotron-based analysis of the precipitates

Roberta Parigi, Ning Chen, Joel W. Reid, Carol J. Ptacek and David W. Blowes

Summary

The determination of fractionation factors associated with important biogeochemical processes controlling Ni availability in the environment is necessary to understand Ni isotope fractionation in natural systems and to use Ni isotope signatures as environmental tracers. In this study we present experimental results on Ni isotope fractionation during the precipitation of Ni hydroxide, Ni hydroxycarbonate and Ni sulfide minerals. In all three systems, Ni isotope determinations show a preferential partition of lighter isotopes into the solid phase with associated fractionation factors ε of -0.40‰, -0.50‰ and -0.73‰ relative to the hydroxide, carbonate and sulfide systems, respectively. Despite uncertainties, we suggest that equilibrium effects are the principal mechanism responsible for the measured Ni isotopic signatures. These findings contribute to the characterization of Ni isotope systematics which is still in the early stages of development.

2.1. INTRODUCTION

Recent improvements in isotope-ratio mass spectrometry have allowed the application of metal stable isotopes to advance (Romanek et al., 2010; Kyser, 2012; Wiederhold, 2015). Many of the processes controlling contaminant mobility in the environment, including oxidation-reduction, precipitation-dissolution, sorption, complexation, evaporation, diffusion, and biological cycling, result in a characteristic change in isotope fractionation; metal stable isotope signatures have been successfully applied as environmental tracers to identify the source and the fate of contaminants (Romanek et al., 2010; Wiederhold, 2015). However, laboratory

studies determining the extent of fractionation for specific processes are paramount before the isotopic signatures of environmental samples can be explained (Wiederhold, 2015).

Nickel stable isotope systematics has developed relatively recently in comparison to other elements (Cameron and Vance, 2014). Much of the work on Ni stable isotopes has focussed on cosmochemical applications, investigating the nucleosynthetic origins of different meteorites (Elliott and Steele, 2017). First data for terrestrial material, exhibiting an average δ^{60}Ni of 0.15 ± 0.12 ‰, were reported by Cameron et al. (2009). These authors were also the first to highlight the potential of Ni stable isotopes as a biogeochemical tracer, measuring Ni isotope fractionation associated with the activity of methanogens (ε^{60}Ni ~ −1‰), that preferentially assimilate light Ni isotopes (Cameron et al., 2009).

Published Ni isotope studies propose magmatic sulfides as the lightest sinks of Ni (δ^{60}Ni = −0.20‰ to −1.03‰) (Gueguen et al., 2013; Hofmann et al., 2014; Estrade et al., 2015), whereas organic-rich marine sediments and ferromanganese crusts are characterized by the heaviest δ^{60}Ni (0.20‰ to 2.50‰, and 0.90‰ to 2.50‰, respectively) (Gall et al., 2013; Porter et al., 2014; Estrade et al., 2015). Nickel shows an average δ^{60}Ni in ocean samples (1.44‰ ± 0.15 ‰) (Cameron and Vance, 2014) that is higher than the average isotopic signature of rivers and of the bulk silicate Earth (0.80‰ and 0.11± 0.01‰, respectively) (Cameron and Vance, 2014; Elliott and Steele, 2017), thus generating mass balance considerations. Either an input that is heavier than riverine isotope values or an isotopically light oceanic sink are required to solve the budget problem of the Ni isotope cycle (Cameron and Vance, 2014). Preliminary isotope results on organic- and sulfide-rich black shales (Pasava et al., 2019) highlight the crucial role played by these sediments, which preferentially incorporate light Ni isotopes, in solving the imbalance. Furthermore, research conducted on laterites, important ultramafic Ni deposits, shows that heavy Ni isotopes are preferentially released into solution during weathering (Gall et al., 2013; Ratié et al., 2015; Ratié et al., 2018; Spivak-Birndorf et al., 2018), therefore contributing to the ‘heavy’ Ni flux to the oceans.

Despite recent studies involving Ni isotopic fractionation during interaction with vegetation (Estrade et al., 2015; Zelano et al., 2018; Ratié et al., 2019), organic acids (Zelano et al., 2018), iron oxy-hydroxides (Wasylenki et al., 2015; Wang and Wasylenki, 2017; Gueguen et al., 2018), calcite (Castillo Alvarez et al., 2020), and birnessite (Sorensen et al., 2020), further research, that aims to identify the Ni isotope signatures of biogeochemical processes, is needed to confidently apply nickel isotopes as environmental tracers.

Nickel is one of the most widely used metals in the world (Denkhaus and Salnikow, 2002; Kasprzak et al., 2003; Nieminem et al., 2007), consequently high Ni concentrations can be found close to industrial areas and mine sites. Chemical precipitation is one of the most common approaches used to recover metals from wastewaters (Costodes and Lewis, 2006; Reis et al., 2013; Salcedo et al., 2016). Nevertheless, chemical precipitation may also occur naturally if the conditions (i.e., pH, Eh, and supersaturation of the solution) are favourable.

The objective of this study is to provide new insight into Ni isotope fractionation during precipitation of secondary mineral phases (i.e., Ni hydroxide, Ni hydroxycarbonate and Ni sulfide) involved in Ni attenuation from the environment, further contributing to the characterization of Ni stable isotope systematics.

2.2. MATERIALS AND METHODS

2.2.1. Precipitation experiments.

Preliminary time-dependent batch experiments were conducted to determine the chemical and isotopic time to equilibrium for the following systems: Ni hydroxide, Ni hydroxycarbonate and Ni sulfide. Details can be found in the Supporting Information (Tables S2.1-S2.3). A second set of batch experiments were performed by mixing Ni-bearing and counteranion-bearing stock solutions in various proportions, to alter the fraction of Ni precipitating from solution (Table S2.4). Nickel hydroxide and Ni hydroxycarbonate were synthesized by mixing 0.05 M $NiCl_2$ with 0.05 M KOH and 0.05M K_2CO_3 stock solutions, respectively. Alternatively, Ni sulfide was precipitated by using 0.05 M $NiSO_4$ and 0.05 M Na_2S stock solutions.

Sacrificial sampling was adopted for both series of batch experiments. Determination of pH was performed on unfiltered subsamples immediately after collection. Filtered samples were collected using 0.2 μm filters (Acrodisc, Pall, UK) and polyethylene syringes (BD, Franklin Lakes, NJ) and used for cations, anions, and Ni isotope analysis. Samples for cation concentration and Ni isotopes determination were also acidified with concentrated HNO_3 (Omnitrace ultra, EMD Millipore).

The batch experiments were carried out in an anaerobic chamber (Coy Laboratory Products Inc., Grass Lake, MI) to avoid oxidation of sulfide and CO_2 interaction with the samples. The reagents used were of analytical grade and prepared using high resistivity (18.2 MΩ cm) ultra-pure water. The input solutions were bubbled with ultra-pure argon gas and left to equilibrate for 24 h inside the anoxic glovebox before performing the experiments.

2.2.2. Sample purification.

The chemical purification of nickel followed a two-step chromatography separation procedure. During the first step, a 3 mL solid-phase extraction (SPE) column was loaded with 2.2 mL pre-cleaned, Bio Rad AG MP-1M (100–200 mesh, chloride form), anion exchange resin. This resin retains Cu, Fe and Zn, whereas Ni is readily eluted and collected. Samples were subsequently dried and dissolved in 1 mL of 7M HCl, then evaporated again and dissolved in 5 mL of 1M HCl. 1 mL of 1M ammonium citrate was added and the pH adjusted to 8-9 with concentrated, ultrapure NH_4OH.

The second step of ion-exchange chromatography columns was modified from Cameron et al. (2009) and involved the use of a Ni-specific resin (Eichrom Technologies). Ni is retained by this resin forming Ni- Dimethylglyoxime (DMG) complexes which are eluted, collected and oxidized for Ni separation.

The purified fractions were evaporated to dryness and finally dissolved in 3% HNO_3 for isotope analysis.

2.2.3. Isotope analysis.

Before preconcentration for Ni isotope analysis, acidified samples were amended with aliquots of $^{61}Ni - ^{62}Ni$ double-spike solution made by mixing ^{61}Ni and ^{62}Ni spikes obtained from Isoflex USA. The optimal $^{61}Ni - ^{62}Ni$ and spike-sample ratios were derived from the algorithm of Rudge et al. (2009).

Nickel isotope analysis was performed on a MC-ICP-MS (Thermo Scientific Neptune) coupled with an APEXQ desolvation introduction system (ESI).^{58}Ni, ^{60}Ni, ^{61}Ni and ^{62}Ni isotopes were measured simultaneously and ^{57}Fe was monitored to correct for potential interference from ^{58}Fe on ^{58}Ni. Off-center peak measurements were conducted in high resolution mode to minimize argide and oxide polyatomic interferences. Data reduction was performed using a double-nested iterative procedure (Siebert et al., 2001).

Ni isotopic compositions are expressed as $\delta^{60}Ni$ in per mill (‰) relative to NIST SRM 986:

$$\delta^{60}\mathrm{Ni} = \left[\frac{(^{60}\mathrm{Ni}/^{58}\mathrm{Ni})_{\mathrm{sample}}}{(^{60}\mathrm{Ni}/^{58}\mathrm{Ni})_{\mathrm{SRM986}}} - 1\right] \mathrm{x}\, 1000 \qquad (1)$$

Results were normalized to the average value of NIST SRM 986 measured before and after each sample and having the same concentration and spike-to-standard ratio as the samples.

The long-term analytical reproducibility of the standard NIST SRM986 was determined to be ±0.05‰ (2SD, n = 105). The external reproducibility was assessed by measuring two reference materials, USGS Nod A1 and Nod P1. The results of 1.06 ± 0.09‰ (n = 10) and 0.33 ± 0.04‰ (n = 10), respectively, are in agreement with published data (Gueguen etal., 2013; Ratié et al., 2015; Wang and Wasylenki, 2017; Ciscato et al., 2018; Wang et al., 2019).

Isotope results, which are reported in the tables, represent the average of three replicate measurements. When the 2SD value of these measurements was lower than the long-term analytical reproducibility, the value of the long-term analytical reproducibility (0.05‰) was adopted.

The measured $\delta^{60}Ni$ values for the input solutions $NiCl_2$ and $NiSO_4$ were −0.17‰ ± 0.06‰ and

−0.52‰ ± 0.05‰, respectively. For the purposes of data interpretation and comparison between the three systems, all samples were normalized to the input solution values, yielding $\delta^{60}Ni_{NiCl2}$ = 0.00 ± 0.06‰ and $\delta^{60}Ni_{NiSO4}$ = 0.00 ±0.05‰.

The isotope results for each investigated system were fit using the Rayleigh equation (2):

$$\frac{R_R}{R_{R0}} = f^{(\alpha-1)} \quad (2)$$

where R_R is the $^{60}Ni/^{58}Ni$ isotope ratio of the residual reactant, R_{R0} is the $^{60}Ni/^{58}Ni$ isotope ratio of the initial reactant (stock solution), α is the fractionation factor, and *f* is the fraction of Ni remaining in solution (Hayes, 2004). For convenience, as α values are close to unity, the extent of fractionation was expressed with the fractionation factor epsilon (ε):

$$\varepsilon = (\alpha - 1)\, x\, 1000\ (‰) \quad (3)$$

2.2.4. Solid-Phase Characterization.

Ni precipitates were centrifuged and washed with ultrapure water before collection and subsequently frozen, freeze-dried and stored in the anaerobic chamber until analysis. Subsamples of the freeze-dried solid material were mounted in 0.5 mm ID Kapton capillaries (Cole-Parmer: 95820-04), which were sealed at both ends with glue (Loctite 454). Synchrotron-based Powder X-ray diffraction (PXRD) was performed at the Canadian Light Source (CLS), Canadian Macromolecular Crystallography Facility (CMCF) bending magnet beamline (08B1-1; Fodje et al., 2014). Two-dimensional (2D) diffraction data were collected on a Rayonix MX300HE detector, using a wavelength (λ) of 0.688 Å (photon energy ~ 18keV). The PXRD patterns were calibrated and integrated (2 to 40°, 2θ) using the GSASII software package (Toby and Von Dreele, 2013). Calibration was performed using a lanthanum hexaboride (LaB6) standard reference material (NIST SRM 660a LaB6). Search/match phase identification was carried out with the Powder Diffraction File, PDF-4+ software (ICDD, 2019).

The remaining solid material was mounted on aluminum sample holders and transported to the hard X-ray microanalysis (HXMA) beamline at the CLS synchrotron facility, for X-ray absorption near edge structure (XANES) and extended X-ray absorption fine structure (EXAFS) characterization. During Ni spectra collection, the CLS storage ring was operated under 250 mA operation mode with three injections per day. The HXMA beamline operated in focus mode, and a Rh mirror was used to collimate and focus the X-ray beam. The monochromatic X-ray beam was produced by using a double crystal Si (220) monochromator. The second crystal was detuned by 50% at the end of the scan to depress high harmonic contamination in the beam. The scan step sizes for the pre-edge, XANES, and EXAFS regions were 10 eV/step, 0.25 eV/step, and 0.05$Å^{-1}$/step, respectively. Multiple scans were collected for each sample to improve the signal to noise ratio and provide more reliable EXAFS data analysis. The spectra were collected in transmission mode. The initial monochromator energy was calibrated at 8333 eV (Ni K-edge) by using Ni metallic foil from EXAFS Materials (http://exafsmaterials.com/). The same Ni metallic foil was set between two ion chamber detectors I1 and I2 downstream of the sample throughout the entire experiment. Thus, in-step energy calibration was achievable for each individual scan. Through the experiment the ion chamber detectors were filled with pure He gas to maintain the linearity of the detecting system. The EXAFS data reduction, including the standard procedures of energy calibration, multiple scan averaging, background subtraction, normalization, etc. was performed using the Athena software package (Ravel and Newville, 2005). Theoretical phase and backscattering amplitude were calculated with FEFF7.02 (Rehr and Albers, 2000). Ni EXAFS data R space curve fitting was carried out using WinXAS version 2.3 (Ressler, 1997).

2.3. RESULTS

2.3.1. Ni removal

The precipitation of Ni hydroxide, Ni hydroxycarbonate and Ni sulfide occurred instantaneously upon mixing of the stock solutions containing Ni and the selected

counteranions (Fig. 2.1A). Decreasing Ni/OH, Ni/CO_3, and Ni/S molar ratios resulted in a greater degree of removal of Ni from solution. Time-dependent experiments show that chemical and isotopic equilibrium was attained within 24 hours in all three systems (Fig. 2.1A and 2.1B). Based on these results, the sampling time for the hydroxide and the carbonate system experiments involving the precipitation of different fractions of Ni was set to 24 hours. A sampling time of 72 hours was chosen for the sulfide system due to greater pH fluctuations during the first two days of the experiment (Table S2.3).

Despite uncertainties regarding the reliability of the thermodynamic data associated with aqueous speciation and solubility of Ni at ambient conditions (Hummel and Curti, 2003), aqueous species distribution in all three systems was calculated using PHREEQC (Parkhurst and Appelo, 1999) together with the wateq4f database, derived from WATEQ4F (Ball and Nordstrom, 1991). The stability constants reported by Baeyens et al. (2003) were used for $NiCO_3$ and $NiHCO_3^+$ aqueous species. Results indicate Ni^{2+} accounted for more than 99% of the aqueous Ni species in all three systems at our experimental conditions.

2.3.2. $Ni(OH)_2$ precipitate characterization

$Ni(OH)_2$ exists as two pseudo polymorphs, α- and β-$Ni(OH)_2$ (Hall et al., 2014). β-$Ni(OH)_2$ occurs naturally as the mineral theophrastite and it is characterized by stacking $Ni(OH)_2$ brucite ($Mg(OH)_2$)-like sheets which are parallel to the crystallographic *ab* plane (Coudun et al., 2006; Hall et al., 2014). The α-$Ni(OH)_2$ polymorph is constituted by layers of β-$Ni(OH)_2$ intercalated by water molecules. This structure can incorporate foreign ions (Hall et al., 2014). X-ray diffraction patterns of the nickel hydroxide precipitated during the 24-hour and 1460-hour (2 months) experiments are shown in Fig. 2.2A. X-ray diffraction results confirmed the precipitation of a β-type $Ni(OH)_2$. EXAFS fitting results for the 24-hour and 2-month $Ni(OH)_2$ samples are shown in Table 2.1. The 2-month data display an increase in coordination number (CN) together with a decrease in the Debye-Waller parameter (σ^2) compared to the 24-hour sample.

2.3.3. $NiCO_3$ precipitate characterization

Fig. 2.2B shows the X-ray diffraction patterns of the nickel hydroxycarbonate samples collected at 72 hours and 1460 hours (2 months). Although the X-ray diffraction patterns of the Ni hydroxycarbonate precipitates formed during this study were compared to a $Ni_2(CO_3)(OH)_2 \bullet 4H_2O$ data set, similar diffraction patterns have been assigned to other nickel-carbonate phases, such as nullaginite [$Ni_2(CO_3)(OH)_2$] (Karadas et al., 2011; Ballesteros et al., 2016; Salcedo et al., 2016) and otwayite [$Ni_2(CO_3)(OH)_2 \bullet H_2O$] (Bhojane et al., 2019). Despite some studies involving the Ni hydroxycarbonate minerals, nullaginite and otwayite (Nickel et al., 1979; Nickel and Berry, 1981), the structural arrangement of these minerals remains unknown. In contrast to the hydroxide and sulfide systems, EXAFS modeling was not attempted for the carbonate system due to the previously mentioned lack of crystallographic data relative to Ni hydroxycarbonate minerals.

2.3.4. NiS precipitate characterization

PXRD results from the NiS precipitation experiment, specifically the 72-hour and the 2-month samples, are presented in Fig. 2.2C. The X-ray diffraction patterns of these samples show broad amorphous peaks at ~14 degrees (d = ~ 2.8 Å) and ~22 degrees (d = ~1.8 Å). These features are consistent with PXRD results obtained by Jeong and Manthiram (2001) and Huang et al. (2009) for Ni sulfides synthesized under similar conditions.

EXAFS fitting results for the 72-hour and 2-month NiS samples are shown in Table 2.2. Because the R space curve fitting based on the sole structure of millerite was not able to fully address the experimental data, the data were fit considering a hybrid NiS-$Ni(OH)_2$ structural model.

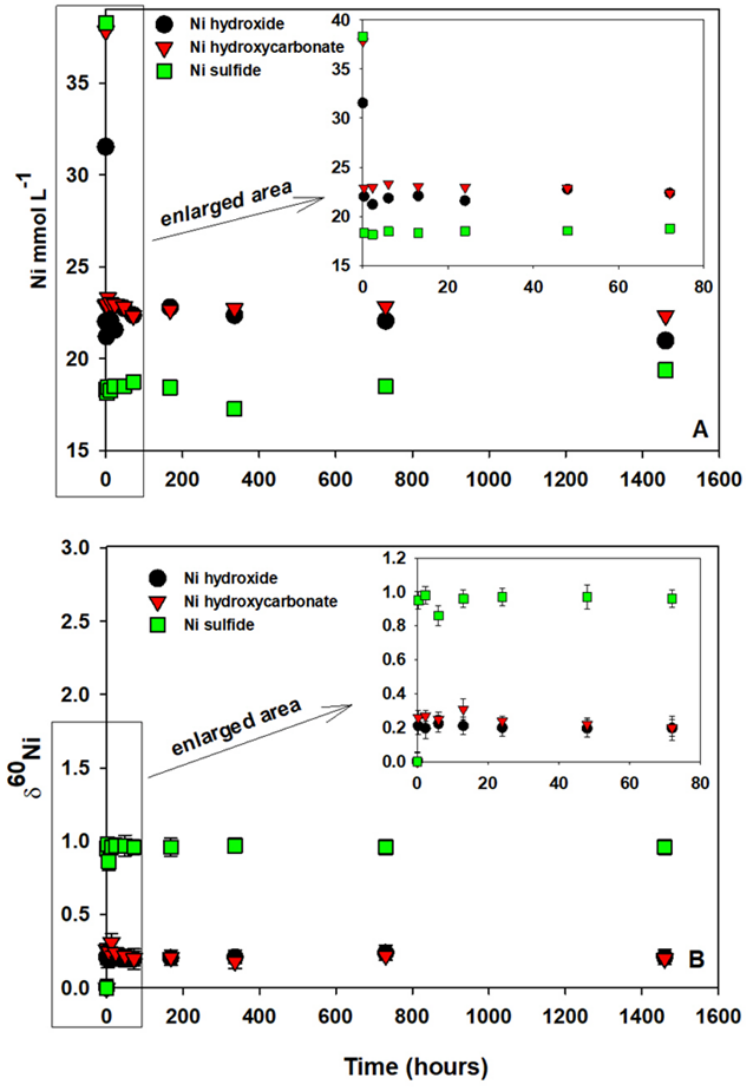

Figure 2.1: A) Time-dependent precipitation of Ni hydroxide, Ni hydroxycarbonate and Ni sulfide. The used molar ratios were [Ni:OH] = 1.5:1, [Ni:CO_3] = 2:1 and [Ni:S] = 2:1, respectively. B) Isotope results of selected samples showing that Ni isotope equilibrium was obtained immediately during the precipitation of Ni hydroxide, Ni hydroxycarbonate and Ni sulfide. The error bars represent 2σ from three analytical events.

2.3.5. Ni isotope ratios

Isotope measurements from experiments with varying Ni/counteranion ratios followed Rayleigh curves as is commonly found in precipitation experiments under certain conditions (Wiesli et al., 2004; Wiederhold, 2015). The isotope fractionation factors (ε) calculated for the Ni-hydroxide, carbonate and sulfide systems were −0.40‰ (R^2=0.955), −0.50‰ (R^2=0.986) and −0.73‰ (R^2=0.956), respectively. Nickel isotope fractionation followed similar trends in all three systems, displaying an increase in the δ^{60}Ni of the solution with decreasing

Ni/counteranion ratios (Fig. 2.3A, 2.3B, and 2.3C). The enrichment of ^{60}Ni with respect to ^{58}Ni, relative to the fraction of Ni remaining in solution during precipitation, indicated that light Ni isotopes were preferentially retained by the solid phases. Recent studies also highlighted the preferential incorporation of light Ni isotopes during coprecipitation with Fe oxyhydroxides (Wasylenki et al., 2015; Wang and Wasylenki, 2017; Gueguen et al., 2018) and calcite (Castillo Alvarez, 2019).

2.4. DISCUSSION

2.4.1. $Ni(OH)_2$ solid phase

The structural order and crystallinity of the $Ni(OH)_2$ precipitates increased with increasing sampling time. Broadening of the peaks involving the c-axis is common for $Ni(OH)_2$ XRD patterns (Delmas and Tessier, 1997; Hall et al., 2012) and is linked to crystallite-size effects (thin platelet morphology; Casas-Cabanas et al., 2005) and crystal defects (stacking faults, vacancies, incorporation of water and foreign ions and interstratified phases) (Song et al., 2002). The early precipitate (24 hours) showed a high degree of broadening of the peaks associated with the (001), (101) and (102) crystallographic planes due to lower crystallinity, higher structural defects and higher water content compared to the 2-month precipitate sample. The 24-hour sample also displayed a splitting of the first peak (001) which Ramesh and Kamath, (2006) attributed to the interstratification of α- type $Ni(OH)_2$ motifs in the matrix of β-type $Ni(OH)_2$. It is known that α-$Ni(OH)_2$ transforms to the more stable and ordered β-$Ni(OH)_2$ with chemical ageing (Faure et al., 1991; Ramesh and Kamath, 2006; Hall et al., 2014). EXAFS fitting results also confirmed the increase in structural order and crystallinity with increasing ageing time (Table 2.1).

In the hydroxide system the enrichment of lighter Ni isotopes associated with the solid phases is expected to be related to longer and weaker Ni-O bond lengths in the precipitates compared to the solution, as Ni occurs in an octahedral configuration both in solution and in the minerals. Ni-O bond lengths, relative to aqueous Ni(II), were estimated to be in the range of 2.04-2.05 Å

(Xu et al., 2007; Yuan Tian et al., 2012; Qiang et al., 2017). EXAFS modeling performed on $Ni(OH)_2$ samples resulted in a Ni-O bond length of 2.05 Å for the 72-hour sample and 2.06 Å for the 2-month sample (Table 2.1). The estimated values are in agreement with previously published data (Defontaine et al., 2003; Wilkin and Rogers, 2010; Bin Han et al., 2019). The observed Ni-O bond lengths of the hydroxide samples are the same as or slightly greater than the Ni-O lengths associated with Ni in solution, thus it is problematic to confidently attribute the measured Ni isotopic fractionation during Ni hydroxide precipitation to bond-length differences. Another explanation for the observed fractionation ($\varepsilon = -0.40‰$) could be related to the distortion of the Ni-O octahedra in the $Ni(OH)_2$ precipitates, which favours the incorporation of the lighter isotopes in the solid phase (Mavromatis et al., 2012). Distortions of the octahedral geometry are known to affect $Ni(OH)_2$ species (Hall et al., 2014), and the turbostratic nature of an early-formed $Ni(OH)_2$ precipitate (Hall et al., 2014), could support this hypothesis. Furthermore, the coordination number obtained from EXAFS fitting and the PXRD pattern relative to the 24-hour $Ni(OH)_2$ sample indicates a defective, less crystalline, and less stable structure compared to the 2-month sample.

Table 2.1: Ni K-edge EXAFS fit parameter results for 24-hour and 2-month Ni hydroxide samples.

Sample	Path	CN	R(Å)	σ^2 (Å^2)	ΔE^0 (eV)
$Ni(OH)_2$ 24 hours	Ni-O	6.0	2.05	0.0092	-1.8
	Ni-Ni	5.2	3.12	0.0098	
$Ni(OH)_2$ 2 months	Ni-O	6.0	2.06	0.0067	-0.9
	Ni-Ni	6.0	3.13	0.0073	

CN, coordination number; R, interatomic distance; σ^2, Debye–Waller parameter; ΔE^0, energy offset parameter

2.4.2. $NiCO_3$ solid phase

Although it can be hydrothermally synthesized, pure gaspeite ($NiCO_3$) does not occur naturally (Isaacs, 1963). Natural gaspeite occurs as a Ni-Mg carbonate solid solution (Villegas-Jiménez et al., 2010). At room temperature the formation of hydrated $NiCO_3$ is favored (Patterson et al.,

1977) and precipitation in the nickel-carbonate system is strictly related to the nickel hydroxide solubility domain (Guillard and Lewis, 2001). Consequently, the solid phase formed in the Ni-OH-CO_3 system is usually a mixed complex of nickel hydroxy-carbonates, with characteristics dependent upon the parameters of the synthesis process (Villegas-Jiménez et al., 2010).

The diffraction patterns of all the Ni carbonate hydroxide phases previously mentioned [$Ni_2(CO_3)(OH)_2 \bullet 4H_2O$, nullaginite, and otwayite] are characterized by broad peaks which have been attributed to nanocrystallinity, low crystal structure symmetry, and structural defects of the solid phase (Karadas et al., 2011; Jia et al., 2013; Ballesteros et al., 2016; Salcedo et al., 2016; Bhojane et al., 2019).

Nullaginite, similar to other $Me_2^{2+}(CO_3)(OH)_2$, can be included in the malachite-rosasite group and, although the mineral crystal structure has not yet been resolved, it can be assumed nullaginite exhibits the structure-type of the mineral rosasite (Perchiazzi and Merlino, 2006). As a result of the paucity of studies on Ni hydroxycarbonates, thermodynamic data relative to these minerals have not been determined (Gamsjäger et al., 2005).

Ni isotope fractionation in the carbonate system ($\varepsilon = -0.50‰$) can be interpreted in a manner that is similar to the $Ni(OH)_2$. Although the structural arrangement of Ni hydroxycarbonate minerals remains unknown, it is possible to make a reasonable assumption based on studies involving hydroxycarbonate minerals of elements with characteristics similar to Ni, such as Co, Cu, Zn and Mg. Secondary minerals with general formula $Me^{2+}{}_2(CO_3)(OH)_2$ can be grouped in the malachite-rosasite structural group (Perchiazzi, 2006; Perchiazzi and Merlino, 2006; Perchiazzi et al., 2017). Both malachite- and rosasite-type crystal structures are characterized by the occurrence of the metal in an octahedral environment, with Me1 connected to two hydroxyl and four oxygen atoms, whereas Me2 is linked to four hydroxyl and two oxygen atoms (Perchiazzi et al., 2017). Both the Me1 and Me2 polyhedra may display different degrees of distortion (Perchiazzi and Merlino, 2006; Perchiazzi et al., 2017). Mavromatis et al. (2012)

attributed the enrichment of lighter Mg isotopes into Mg hydroxycarbonate precipitates to the distortion of MgO_6 octahedra in the structure of hydrous Mg carbonate minerals.

The ε value of −0.50‰ associated with the precipitation of Ni hydroxycarbonate is very close to the equilibrium isotope fractionation factor $\Delta^{60}Ni_{calcite\text{-}fluid} = -0.52 \pm 0.16$ ‰ related to the adsorption of Ni onto calcite, as reported by Castillo Alvarez et al. (2020).

2.4.3. NiS solid phase

Nickel sulfides are characterized by complex structural, compositional and magnetic properties which make them valuable for a variety of technological applications (Jeong and Manthiram, 2001; Balayevaa et al., 2016). The initial conditions of the synthetic process (i.e., sulfide source, reaction time, temperature, and pH) play a considerable role in the production of different Ni sulfide phases, such as: Ni_3S_2, Ni_3S_4, Ni_7S_6, Ni_9S_8, NiS_2, and NiS (Olivas et al., 1998; Balayevaa et al., 2016; Gervas et al., 2017).

Huang et al. (2009) defined the solid phase characterized by the two broad amorphous peaks at ~14 degrees (d = ~ 2.8 Å) and ~22 degrees (d = ~1.8 Å) as a hydrated nanoparticulate material characterized by a crystalline millerite (NiS) core surrounded by a hydrate shell. The material, with an approximate formula $NiS•1.5H_2O$, was shown to transform to polydymite (Ni_3S_4) at pH < 7 (Huang et al., 2009). The diffraction patterns of precipitate samples (Fig. 2.2C) indicate that polydymite may be present, in small amounts, after 72 hours. The presence of polydymite increased over time, leading to polydymite-related peaks becoming sharper. The 72-hour sample is also characterized by peaks corresponding to nickelhexahydrite $[Ni(SO_4)•(H_2O)_6]$, the salt used to prepare the $NiSO_4$ stock solution.

The inclusion of $Ni(OH)_2$ together with NiS species considerably improved the quality of the EXAFS fit. Huang (2008) hypothesized the potential precipitation of either a $Ni(OH)_2$-like phase or a hybrid material composed of both millerite and theophrastite structural components in similar studies due to a slight excess of Ni over S in the Ni:S ratio of the hydrated NiS solid phase.

Table 2.2: Ni K-edge EXAFS fit parameter results for 72-hour and 2-month Ni sulfide samples.

Ni species	NiS 72 hours				NiS 2 months		
	Path	CN	*R*(Å)	σ^2 (Å^2)	CN	*R*(Å)	σ^2 (Å^2)
NiS	Ni-S	4.9	2.22	0.0095	5.2	2.22	0.0095
	Ni-Ni	1.7	2.78	0.0098	1.2	2.77	0.0098
	Ni-Ni	2.2	3.03	0.0096	2.0	3.02	0.0096
$Ni(OH)_2$	Ni-O	5.6	2.18	0.0095	6.0	2.19	0.0085
	Ni-Ni	0.8	3.12	0.0096	1.1	3.14	0.0096
	ΔE^0 (eV) = 4.9				ΔE^0 (eV) = 3.2		

CN, coordination number; R, interatomic distance; σ^2, Debye–Waller parameter; ΔE^0, energy offset parameter

Ni isotope fractionation during Ni sulfide precipitation, which resulted in a ε value of −0.73‰, could be associated with a change in coordination environment, from Ni-O to Ni-S.

Fujii et al. (2011; 2014) estimated the equilibrium fractionation factor between the dissolved species Ni^{2+} and $Ni(HS)^+$ to be $\Delta^{60}Ni_{Ni2+\text{-}Ni(HS)+}$ =+0.68‰ and $\Delta^{60}Ni_{Ni2+\text{-}\ Ni(HS)+}$ =+0.66‰ at 25°C, respectively. Considering the analytical uncertainties, the measured fractionation factor is in good agreement with the calculated values. Furthermore, the measured Ni isotope fractionation did not significantly change over the course of the 2-month time-dependant batch experiments. These observations suggest that the fractionation associated with the sulfide system occurred between ligands in solution prior to mineral nucleation, as also previously been observed by other researchers during FeS and HgS precipitation experiments (Wiesli et al., 2004; Smith et al., 2015).

It is worth noting that the transformation of β-NiS to Ni_3S_4, despite associated with changes in the structure and coordination environment, did not seem to affect the measured Ni isotope fractionation. It is possible that the magnitude of the transformation in the smaller reservoir (i.e., solid phase) was not sufficient to shift the fractionation of Ni isotopes in solution (i.e., larger reservoir).

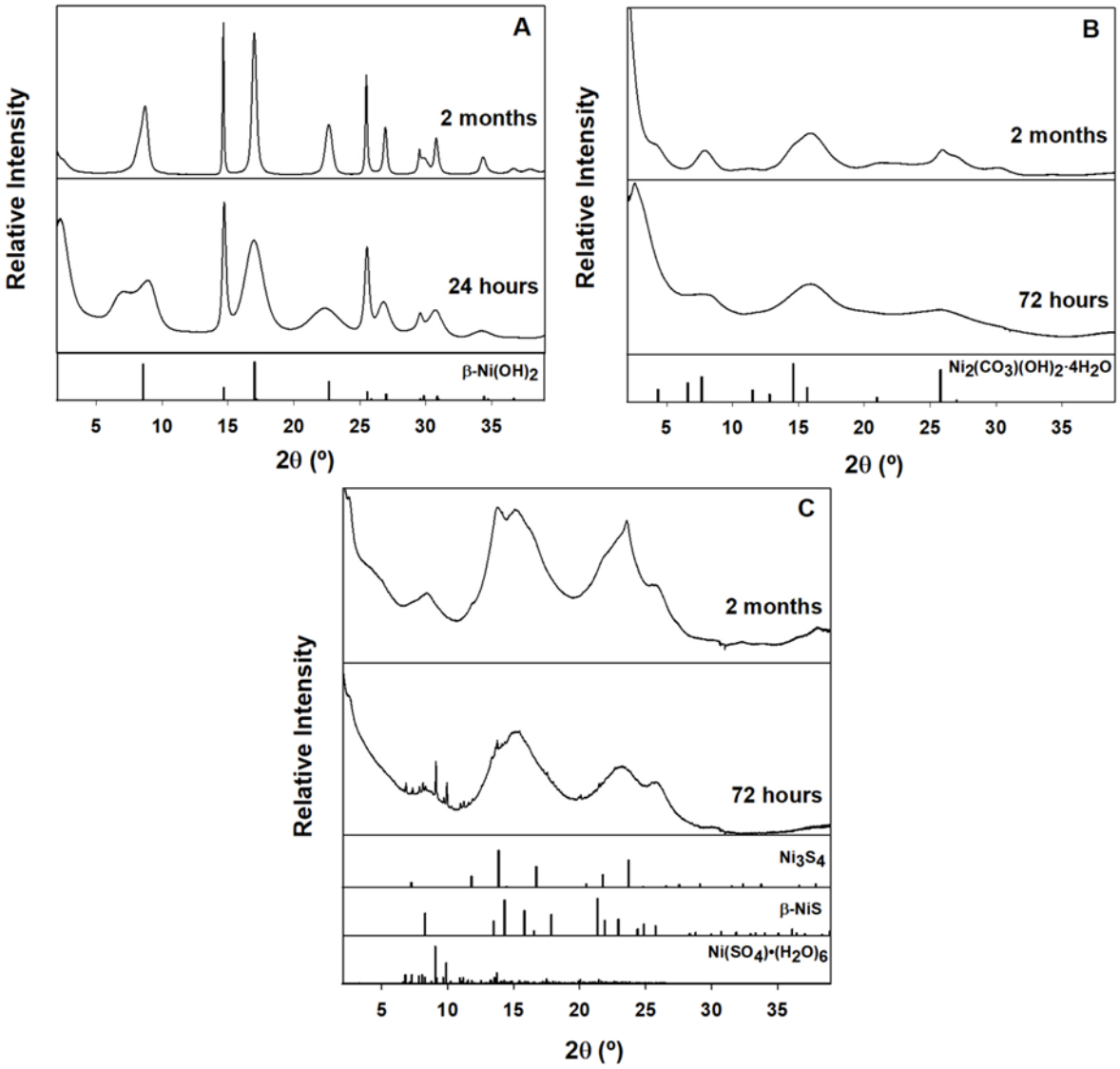

Figure 2.2: X-ray diffraction patterns of Ni precipitates: A) Ni hydroxide sampled after 24 hours and 1460 hours (2 months). B) Ni hydroxycarbonate sampled after 72 hours and 1460 hours (2 months). C) Ni sulfide sampled after 72 hours and 1460 hours (2 months). Powder Diffraction data files shown for β-$Ni(OH)_2$(01-073-1520), $Ni_2(CO_3)(OH)_2 \cdot 4H_2O$ (00-038-0714), millerite β-NiS (04-014-3037), polydymite Ni_3S_4 (04-004-5623) and $Ni(SO_4)(H_2O)_6$ (04-015-6154).

2.4.4. Kinetic versus equilibrium Ni isotope fractionation.

Isotope results from the time-dependant experiments suggest that Ni isotopic equilibrium was rapidly attained during the precipitation of Ni hydroxide, Ni hydroxycarbonate and Ni sulfide (Fig. 2.1B). The increase in crystallinity with longer ageing time did not seem to affect Ni isotope fractionation in either the hydroxide or carbonate systems.

A rapid isotopic equilibrium was also observed for Zn precipitates during similar batch experiments (Veeramani et al., 2015).

When mineral precipitation occurs, the associated isotope fractionation can be controlled by either kinetic or equilibrium effects which are often difficult to discern (Wiederhold, 2015). The time-dependant experiments showed analogous trends in Ni isotope fractionation to the experiments involving varying Ni/counteranion ratios. Furthermore, comparable results involving Zn-isotope fractionation associated equilibrium effects with similar precipitation experiments (Veeramani et al., 2015). Nickel isotope fractionation was generally constant over the 2-month period in all three systems analyzed, without detectable changes over time; in contrast to, the variation encountered by Butler et al. (2005) during the course of FeS precipitation experiments. Therefore, we are inclined to attribute the magnitude of Ni isotope fractionation measured in the present studies to equilibrium effects. If the results represent kinetic isotope fractionation effects, the constancy of the fractionation with time would indicate that reaching equilibrium is a very slow process.

2.4.5. Relationship between Ni isotopic fractionation and chemical bonds

At equilibrium, isotope fractionation between two phases is influenced by changes in redox conditions, coordination and bonding environment (Wasylenki et al., 2015; Wiederhold, 2015). Heavier isotopes tend to partition into species with higher oxidation state and form the stiffest bonds (i.e., the shortest and strongest chemical bonds) (Schauble, 2004; Wasylenki et al., 2015; Wiederhold, 2015; Gueguen et al., 2018). As previously discussed for the Ni hydroxide and Ni

hydroxycarbonate systems, changes in bond lengths and/or distortions of structural sites can induce isotope fractionation between dissolved Ni and Ni-bound to the solid phase, especially when coordination and bonding environment do not vary during the reactions. Gueguen et al. (2018) suggested the formation of weak surface complexes could be responsible for the enrichment of light Ni isotopes during Ni sorption to ferrihydrite and goethite experiments, which resulted in fractionation factors $\Delta^{60}Ni_{min\text{-}aq}$ of −0.35 ± 0.08‰, and −0.77 ± 0.23‰, respectively. Variations of the Ni fractionation factors ($\Delta^{60}Ni_{min\text{-}aq}$ ranging from −2.76‰ to −3.35‰) observed in experiments involving Ni sorption to birnessite at different pH were reported to be affected by differences in Ni-O bond lengths (Sorensen et al., 2020). Furthermore, Wang and Wasylenki (2017) indicated the incorporation of lighter Ni isotopes during hematite formation being related to the distortion of Ni-O octahedra in the hematite structure. The extent of the isotope fractionation calculated for the Ni-hydroxide and carbonate systems (ε of −0.40‰ and −0.50‰, respectively; Fig 2.3A and 2.3B), is within the range of the values of Ni isotope fractionation associated with changes in Ni structural configuration reported by other researchers (Wasylenki et al., 2015; Wang and Wasylenki, 2017; Gueguen et al., 2018; Castillo Alvarez et al., 2020; Sorensen et al., 2020). As the structural arrangements of Ni hydroxide and Ni hydroxycarbonate minerals are strictly connected, it is reasonable to find the magnitude of Ni isotope fractionation in the two systems is similar.

The extent of fractionation associated with Ni sulfide precipitation (ε = −0.73‰; Fig. 2.3C), which was found to be comparable to the fractionation estimated by Fujii et al. (2011; 2014) for Ni^{2+} and $Ni(HS)^{+}$ dissolved species, was linked to the change in coordination environment (from Ni-O to Ni-S) developing in solution. A similar explanation was also adopted by Vance et al. (2017) who related the fractionation factor ε = −0.70‰, associated with Ni isotope data from the Black Sea at a depth $\geqslant$ 300 m, to isotope exchanges taking place between a dissolved Ni pool and Ni sulfidized species subsequently removed from solution.

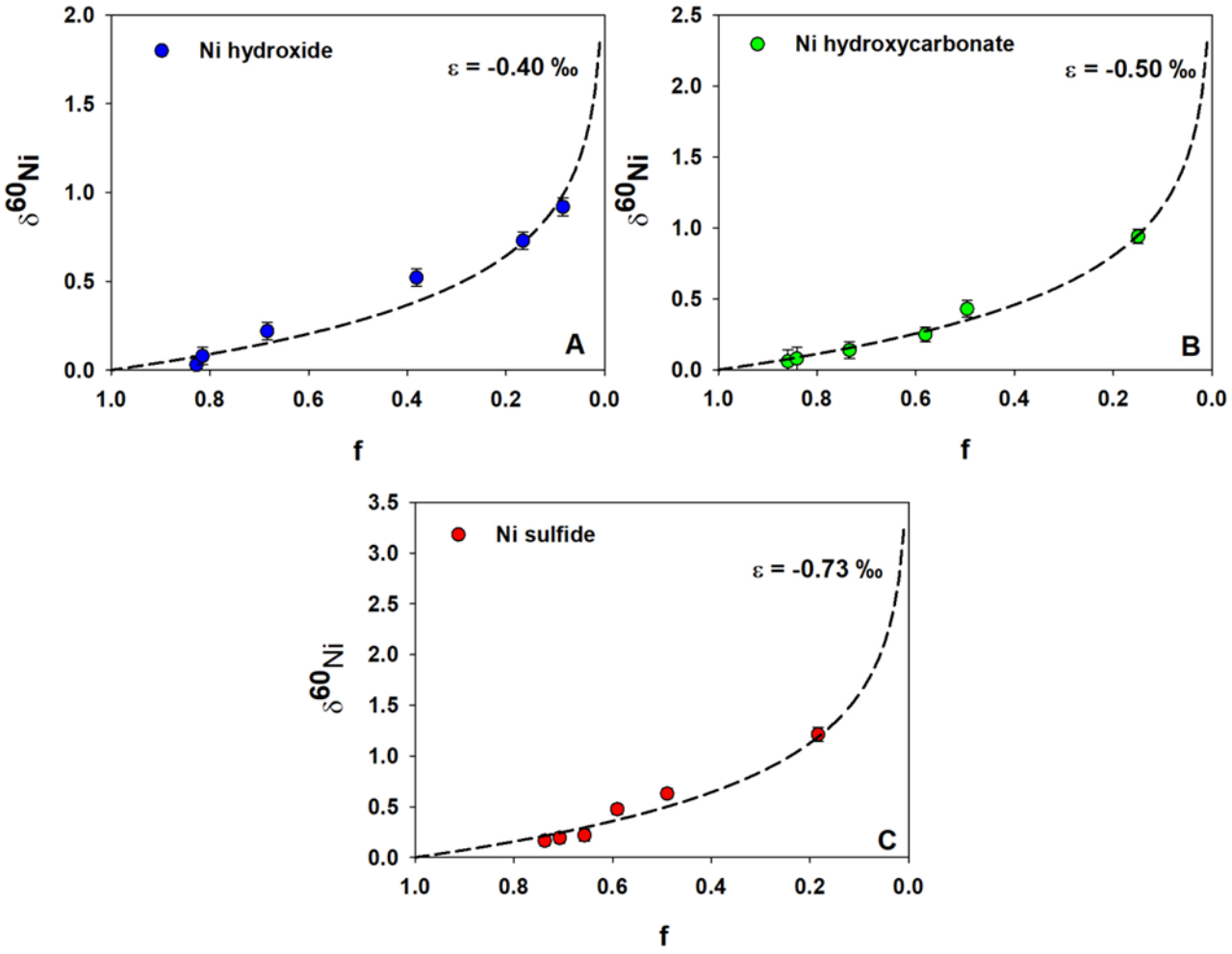

Figure 2.3: Isotope fractionation (δ^{60}) of Ni relative to the input solutions versus the fraction of Ni remaining in solution (f) during precipitation of Ni hydroxide (A) Ni hydroxycarbonate (B), and Ni sulfide (C). The error bars represent 2σ from three analytical events. The dashed lines show the best-fit Rayleigh models with R^2=0.955, R^2=0.986, and R^2=0.956 for Ni hydroxide (blue), Ni hydroxycarbonate (green), and Ni sulfide (red) systems, respectively.

2.4.6. Implications for field studies

Secondary minerals play a decisive role in the natural attenuation of heavy metals, thus the assessment of the contribution of Ni isotopic signature during mineral precipitation is crucial to the application of Ni stable isotopes as environmental tracers. Although the determination of fractionation factors in laboratory studies is fundamental to the comprehensive understanding of Ni isotope systematics (Wiederhold, 2015), chemical and physical processes in complex environmental systems may be difficult to address through Ni isotope measurements. Furthermore, the fractionation factors, especially the ones related to the hydroxide and carbonate precipitation experiments, are very similar. Consequently, it could be challenging to

uniquely quantify the isotopic contribution of each system to the overall degree of fractionation observed in field samples. As the magnitude of fractionation could be affected by experimental conditions, further studies should be conducted that aim to delineate the role of other variables on Ni isotope fractionation, such as: pH, temperature, solution concentrations, and the presence of biota or other Ni-competing elements in the system.

2.5. SUMMARY OF RESEARCH RESULTS

The present study provides constraints on Ni isotope fractionation during the precipitation of Ni secondary minerals at ambient conditions in abiotic systems. Results from this study offer valuable information to the characterization of Ni isotope systematics aimed to the use of Ni isotopes as environmental tracers. The major findings can be summarized as follows:

(1) Time-dependant experiments indicate that Ni chemical and isotopic equilibrium was rapidly attained during the precipitation of Ni hydroxide, Ni hydroxycarbonate and Ni sulfide minerals.

(2) Nickel isotope fractionation followed similar Rayleigh trends in all three experimental Ni-hydroxide, carbonate and sulfide systems, yielding fractionation factors ε of −0.40‰, −0.50‰, and −0.73‰, respectively.

(3) Distortion of the Ni-O octahedra constituting the Ni-hydroxide and Ni-hydroxycarbonate structures related with the preferential incorporation of light Ni isotopes into these solid phases. In contrast, the transition from Ni-O to Ni-S coordination environment in solution was indicated to induce the fractionation associated with the Ni sulfide system.

CHAPTER 3

Microbially-mediated removal of Ni from synthetic, contaminated groundwater and associated Ni isotope fractionation

Roberta Parigi, Eva Pakostova, Joel W. Reid, Emily M. Saurette, Joyce M. McBeth, Carol J. Ptacek and David W. Blowes

Summary

Microbially-mediated sulfate reduction is a promising cost-effective and sustainable alternative utilized in permeable reactive barriers (PRBs) and constructed wetlands to treat mine wastewater. Batch experiments were performed to evaluate Ni isotope fractionation associated with precipitation of Ni-sulfides in the presence of the sulfate-reducing bacterium (SRB) *Desulfovibrio desulfuricans* ^{T} (DSM-642).

Precipitates were collected anaerobically and characterized by synchrotron powder X-ray diffraction (PXRD), scanning electron microscopy combined with energy-dispersive X-ray spectroscopy (SEM-EDS) and transmission electron microscopy (TEM). Solid-phase analyses showed the precipitates associated with bacteria biofilm systems were characterized by increased size and crystallinity. Lighter Ni isotopes were preferentially concentrated in the solid phase, whereas the solution was enriched in heavier Ni isotopes when compared to the input solution. Removal of Ni from solution appeared to follow closed-system equilibrium isotope fractionation, yielding a fractionation factor of $\Delta^{60}Ni_{solid\text{-}aq} = -1.99‰$. The results from the present research suggest the measured Ni isotope fractionation is influenced by multiple Ni reaction mechanisms which take place in the investigated system during complex SRB-Ni interactions.

1.1 INTRODUCTION

The extensive industrial use of Ni has led to the release of this heavy metal into the environment. Although Ni is considered an essential micronutrient for plants and many other

biota, high Ni concentrations can have harmful effects on plants, micro-organisms, animals and humans (Denkhaus and Salnikow, 2002; Kasprzak et al., 2003; Niemen et al., 2007; Schaumlöffel,2012; Das et al., 2019).

Metal sulfide precipitation as a remediation technique has been successfully applied to treat acid mine drainage and industrial wastewaters (Lewis, 2010). Sulfide precipitation has been shown to be more effective than traditional metal hydroxide precipitation (Lewis and van Hille, 2006; Lewis, 2010). The main advantages of sulfide precipitation include: the low solubility of sulfide phases, the high rate of removal at low pH, and the potential recovery of metals from the precipitates. Sulfide precipitates are also characterized by more rapid settling rates and superior dewatering properties compared to hydroxides (Lewis and van Hille, 2006; Lewis, 2010). Research involving Ni sulfide precipitation at low temperature has included both biotic (Ferris et al., 1987; Fortin et al., 1994; Sitte et al., 2013; Qian et al., 2015; Mokone et al., 2012; Mansoret al., 2019) and abiotic (Olivas et al., 1998; Jeong and Manthiram, 2001; Huang et al., 2009; Wilkin and Rogers, 2010; Balayeva et al., 2016; Barim et al., 2018) experiments that have resulted in the formation of a variety of Ni sulfide phases, such as α-NiS, β-NiS, Ni_3S_4, NiS_2, Ni_3S_2, Ni_7S_6, Ni_9S_8, depending on the experimental conditions (i.e., pH, sulfur source, reaction time) (Olivas et al., 1998; Jeong and Manthiram, 2001; Balayeva et al., 2016; Barim et al., 2018).

Microbially-mediated reduction of sulfate under anaerobic conditions plays an important role in the treatment of waste streams contaminated by heavy metals (Fortin et al., 1994; Gramp et al., 2007; Sitte et al., 2013; Qian et al., 2015; Mokone et al., 2012). Sulfate-reducing bacteria (SRB) are able to reduce dissolved sulfate coupled with the oxidation of organic compounds resulting in the attenuation of metals through the precipitation of metal sulfides (Blowes et al., 2000):

$$2CH_2O_{(s)} + SO_4^{2-}{}_{(aq)} + 2H^+_{(aq)} \rightarrow H_2S_{(aq)} + 2CO_{2\,(aq)} + H_2O_{(l)} \quad (1)$$

$$Me^{2+}_{(aq)} + H_2S_{(aq)} \rightarrow MeS_{(s)} + 2H^{+}_{(aq)} \quad (2)$$

In contrast with abiotic sulfide precipitation, the microbially-mediated process has the capacity to simultaneously remove dissolved sulfate and heavy metals, which are often major problematic constituents of mining and industrial wastewaters, at low cost and reduced risk (Huisman et al., 2006). Because of these aspects, SRB have been utilized in passive remediation systems, such as permeable reactive barriers (PRBs), with positive outcomes (Benner et al., 1997, 1999 and 2002; Blowes et al., 2000).

Metal stable isotope analysis has become a valuable tool in the field of environmental geochemistry with applications focussing on tracing the source and cycling of metals in the environment (Wiederhold, 2015). Studies on Ni isotope fractionation have focused on terrestrial materials, and recently have highlighted the potential of Ni isotope signatures to be used as bio-geochemical tracers. Investigations conducted on microbial activity (Cameron et al., 2009), type of vegetation (Estrade et al., 2015; Ratié et al., 2019), weathering (Ratié et al., 2015 and 2018; Spivak-Birndorf et al., 2018), adsorption (Wasylenki et al., 2015; Wang and Wasylenki, 2017; Gueguen et al., 2018; Castillo Alvarez et al., 2020; Sorensen et al., 2020) and the formation of secondary minerals[33,34,38] (Wasylenki et al., 2015; Wang and Wasylenki, 2017; Parigi et a., Chapter 2) have pointed out how these factors induce significant Ni isotope fractionation. For example, recent studies have shown a preferential uptake of lighter Ni isotopes by minerals during adsorption onto calcite ($\Delta^{60}Ni_{min\text{-}aq} = -0.52‰$))[36], and birnessite ($\Delta^{60}Ni_{min\text{-}aq} = -2.76$ to $-3.35‰$) (Sorensen et al., 2020). Furthermore, research involving the precipitation of Ni-hydroxide, Ni-hydroxycarbonate and Ni-sulfide has shown that lighter Ni isotopes are incorporated into the solid phases, resulting in fractionation factors $\varepsilon = -0.40‰$, $-0.50‰$ and $-0.73‰$, respectively (Parigi et al., Chapter 2).

The purpose of this study was to determine the mechanisms responsible for Ni removal from solution under biologically-mediated sulfate reduction, and to measure Ni isotope fractionation associated with these processes. Assessment of Ni isotope signatures resulting from

microbially-mediated attenuation of Ni in contaminated groundwater is of great importance for the application of isotope analysis to trace the cycle of Ni in natural systems and to determine the fate and bioavailability of Ni in the environment. Due to the important role SRB play in many passive remediation systems, exploring their role is an important first step in understanding microbial processes influencing Ni isotope fractionation in mine-waste impacted systems.

3.1. MATERIALS AND METHOD

3.1.1. Batch experiments.

Desulfovibrio desulfuricans^{T} (strain Essex 6, DSM-642) was cultured in Postgate B medium (Postgate, 1984) which contained the following, per liter of distilled water: 0.5 g K_2HPO_4, 1.0 g $CaSO_4$, 1.0 g NH_4Cl, 2.0 g $MgSO_4 \cdot 7H_2O$, 3.5 g Na lactate, 1.0 g yeast extract, 0.1 g ascorbic acid, 0.1 g thioglycolic acid, and 0.5 g $FeSO_4 \cdot .7H_2O$. The medium was bubbled with Ar gas before the addition of $FeSO_4 \cdot 7H_2O$. The pH of the complete medium was adjusted to 7.4 with 10M NaOH. The medium (75 mL aliquots) was transferred to 100 mL serum bottles, and briefly bubbled with the same gas. The serum bottles were capped and crimped before autoclaving (121 °C, 30 min). After cooling, the bottles were inoculated with *D. desulfuricans*, and cultivated at room temperature for 6 days (without agitation) before subculturing (~10% inoculum) into fresh Postgate B medium.

Postgate C medium (Postgate, 1984), containing in g L^{-1}: 0.5 KH_2PO_4, 1.0 NH_4Cl, 4.5 Na_2SO_4, 0.04 $CaCl_2.2H_2O$, 0.06 $MgSO_4.7H_2O$; 6.0 Na lactate, 1.0 yeast extract, 0.004 $FeSO_4 \cdot 7H_2O$, and 0.3 sodium citrate$\cdot 2H_2O$; pH~7.5, was transferred into 40 mL serum bottles and bubbled with Ar gas. The serum bottles were capped, crimped and then autoclaved. Once cooled, Postgate C medium was inoculated with the second-generation Postgate B culture (~1 mL) and then incubated at 27°C.

After several subcultures, 1 mL aliquots of *D. desulfuricans* at late logarithmic phase (~24 h) were inoculated and cultivated at 27°C in 40 mL serum bottles filled with modified Postgate C medium (pH~6.8) characterized by the absence of Fe and sodium citrate.

Filter-sterilized aliquots of 1M $NiCl_2$ stock solution, bubbled with Ar, were injected into the 40 mL serum bottles containing *D. desulfuricans* grown in modified Postgate C medium for 4 days. The initial concentrations of Ni in solution were 10, 15, 20, 25, 30, and 40 mM. Sacrificial sampling was conducted at 1 hour, 1 day, and 1 week after the addition of Ni. Aqueous samples were filtered using 0.2 μm filters (Acrodisc, Pall, UK) and polyethylene syringes (BD, Franklin Lakes, NJ), with the exception of the subsamples on which pH measurement was performed. Samples for cation and Ni isotope analyses were acidified with concentrated HNO_3 (Omnitrace ultra, EMD Millipore). Solid samples were centrifuged and collected in an anaerobic chamber (Coy Laboratory Products Inc., Grass Lake, MI) to avoid oxidation. Solid subsamples for isotope analysis were washed multiple times with ultrapure water then frozen, freeze-dried and digested with aqua regia. Subsamples for solid-phase characterization were also frozen and freeze-dried but not washed.

Parallel batch tests using the same conditions as adopted in the main experiment were conducted to evaluate the bacterial viability. After the exposure of SRB to different Ni concentrations (10, 15, 20, 25, 30, and 40 mM) at different times (1 hour, 1 day, and 1 week), 1 mL of solution was injected into fresh Postgate B medium to assess the potential toxicity of Ni to the microorganisms.

3.1.2. Isotope measurements.

Sample preparation and Ni isotope analysis were conducted following Parigi et al., in submission [38]. Briefly, acidified samples were spiked with a $^{61}Ni - ^{62}Ni$ double-spike solution and purified following a two-step chromatography procedure. First, the samples were loaded onto Bio Rad AG MP-1M (100–200 mesh, chloride form) anion exchange resin to separate Ni from Fe, Zn and Cu. Afterwards, a Ni-specific resin from Eichrom Technologies was used to

ensure a clean sample. Eluted Ni fractions were evaporated and finally dissolved in 3% HNO_3 for MC-ICP-MS analyses.

Nickel isotope ratios were determined on a Thermo Scientific Neptune MC-ICP-MS with an APEXQ desolvation introduction system (ESI). Measurements were made in high resolution mode on the low mass shoulders of the peaks to avoid polyatomic interferences. The raw data were processed following the method described by Siebert et al. (2001), and the true isotopic composition of the samples was expressed as δ^{60}Ni in per mill (‰) relative to the NIST SRM 986 Ni isotope standard:

$$\delta^{60}\mathrm{Ni} = \left[\frac{(^{60}\mathrm{Ni}/^{58}\mathrm{Ni})_{\mathrm{sample}}}{(^{60}\mathrm{Ni}/^{58}\mathrm{Ni})_{\mathrm{standard}}} - 1\right] \mathrm{x}\, 1000 \qquad (3)$$

Results were normalized to the average value of NIST SRM 986 measured before and after each sample. The long-term analytical reproducibility of the standard NIST SRM986 was determined to be ±0.05‰ (2SD, n = 167). A 2SD value of 0.05‰ (long-term reproducibility) was used when the 2SD related to three data points for each sample was <0.05‰.

The measured Ni for the input solution $NiCl_2$ was -0.17‰ ± 0.05‰. For the purposes of plotting, comparison, and data interpretation, all samples were normalized to the input solution value, resulting in $\delta^{60}Ni_{NiCl2} = 0.00 \pm 0.05$‰.

3.1.3. Solid-Phase Characterization.

Subsamples of the freeze-dried solid material were mounted in 0.5 mm ID polyimide capillaries (Cole-Parmer: 95820-04), which were sealed at both ends with glue (Loctite 454 Prism Gel, Henkel) and analysed with synchrotron-based powder X-ray diffraction (PXRD). PXRD patterns were collected at the Canadian Light Source (CLS), Canadian Macromolecular Crystallography Facility (CMCF) bend magnet beamline (08B1-1; Fodje et al., 2014). Two-dimensional (2D) diffraction data were collected on a Rayonix MX300HE detector, using a wavelength (λ) of 0.688 Å (photon energy ~ 18 keV). The sample-detector distance, detector

centering, and tilt were calibrated using a lanthanum hexaboride (LaB_6) standard reference material (NIST SRM 660a LaB6). The PXRD patterns were calibrated and integrated (2 to 40°, 2θ) using the GSASII software package (Toby and Von Dreele, 2013). Search/match phase identification was performed with Powder Diffraction File, PDF-4+ software (ICDD, 2019). Samples for whole-grain mounts were filtered with a Whatman® grade 4 (20 – 25 µm) cellulose filter to collect the precipitates for scanning electron microscopy and energy-dispersive X-ray spectroscopy (SEM-EDS) analyses. The precipitates were dried in an anaerobic glovebox for approximately 24-hr and then dispersed on conductive carbon tape applied to a metal sample stub. All sample preparation was completed in an anaerobic glovebox to prevent the oxidation of the precipitates which contain reduced sulfur and metal species. Mounted samples were removed from the anaerobic glovebox in sealed containers and opened immediately before SEM analysis. A conductive coating was not applied to whole-grain mount samples before analysis.

Grain mounts were characterized with a FEI Quanta™ 250 FEG-ESEM with an Oxford Instruments x-act silicon drift detector (SDD) for EDS. Back-scattered electron (BSE) and secondary electron (SE) images were acquired with an accelerating voltage of 20 kV and a sample distance of 10 mm from the detectors.

Samples for transmission electron microscopy (TEM) characterization were sonicated to disperse the precipitated nanoparticles in solution and then diluted 1:100 in ultrapure water (MilliQ A10 water system 18.2 MΩ cm @ 25 °C). The diluted solution was pipetted onto a Formvar/Carbon 400-mesh copper Pelco® TEM grid. The nanoparticles were characterized with a Zeiss Libra 200MC TEM equipped with an EDS detector. TEM images were acquired at an accelerating voltage of 200 kV. Images were processed using Digital Micrograph (Gatan Inc.) and lattice distances were calculated from the inverse fast Fourier Transform (FFT) patterns of selected areas after masking the FFT pattern to improve the delineation of atomic distances.

3.2. RESULTS AND DISCUSSION

3.2.1. Nickel removal by SRB culture.

Results from the batch experiments can be found in the Supporting Information (Table S3.1). The Ni removal efficiency achieved using different initial metal concentrations is shown in Figure S3.1. Nickel removal from solution reached almost 95% after 1 week in the batches with the lowest initial Ni concentration (10 mM). As the concentration of Ni was increased, Ni removal was progressively lower, and the batches with the highest initial Ni concentration (40 mM) had a removal rate of approximately 25%. The 25% removal rate remained relatively constant in the 1-day and 1-week samples likely due to the high metal concentration that inhibited sulfate reduction. Bacterial viability tests showed no bacterial growth in fresh Postgate B inoculated from the batches containing 40 mM of Ni and sampled after 1 day and 1 week. These results suggest the SRB were negatively impacted by the highest Ni concentration used in the experiments (40 mM).

Total sulfur concentrations in solution also decreased with time, showing a removal of ~50% after 1 week, common to all the batches regardless of the initial Ni amounts.

3.2.2. Characterization of the solid phase.

The final solid phase product was composed of a predominant black deposit that accumulated at the bottom of the serum bottles and a shiny metallic mirror-like precipitate concentrated on the sides of the bottles (Figure S3.2 a, b and c). The thin metallic precipitate was characterized by significant growth over the course of the experiments. The growth was inversely proportional to the initial concentration of Ni: the 10 mM samples were distinguished by the largest amount of the shiny deposit, whereas the 40 mM samples exhibited only a small amount of the same solid phase. During the experiments, the metallic precipitate started forming first on the side of the serum bottles and subsequently accumulated at the bottom of the bottles. At equal Ni concentrations, the 1-week samples showed the largest amount of the shiny precipitate

with the exception of the 40 mM batches which displayed an equal amount of the same precipitate at collection times of 1 day and 1 week.

Because of the delicate, thin, sheet-like nature of the metallic phase, it was impossible to effectively separate it from the black deposit. Thus, samples taken for the solid product characterization consisted of a mixture of these two solid phases.

The powder X-ray diffraction patterns for the 10 mM and 40 mM samples collected after 1 hour, 1 day, and 1 week are displayed in Figure 3.1. All patterns were characterized by broad peaks at ~14 degrees (d = ~ 2.8 Å) and ~22 degrees (d = ~1.8 Å). Similar features were also reported by previous abiotic (Jeong and Manthiram, 2001; Huang et al., 2009; Parigi et al., Chapter 2) and biotic (Sitte et al., 2013; Mansor et al., 2019) Ni sulfide precipitation studies and were attributed to poorly crystalline polyphasic Ni-sulfide precursors (Mansor et al., 2019). Such poorly-crystalline Ni sulfides were dominantly nanoparticulate material with the general formula $NiS \cdot 1.5H_2O$ which displayed an anhydrous core of crystalline millerite (β-NiS) surrounded by a hydrate shell (Huang et al., 2009). The Ni:S ratio of the hydrated NiS exhibited a slight excess of Ni over S, thus indicating the potential deposition of a $Ni(OH)_2$-like phase in the mantle layer (Huang, 2008). Some of the early time patterns (i.e., 10 mM at 1 hour, Figure 3.1Aa; 10 mM and 40 mM at 1 day, Figures 3.1Ba and 3.1Bb) showed an additional broad peak at ~8.5 degrees (d =~4.6 Å). As 4.6 Å corresponds to the Bragg reflection associated with the (001) planes of the mineral theophrastite ($Ni(OH)_2$), the presence of this peak is consistent with the potential precipitation of either a $Ni(OH)_2$-like phase or a hybrid material composed of both a millerite and a theophrastite structural components (Huang, 2008). Furthermore, Wilkin and Rogers (2010) demonstrated that freshly precipitated nickel sulfide is characterized by residual Ni-O coordination which is replaced by Ni-S coordination with ageing time.

Although the 1-day 10 mM and 1-day 40 mM patterns (Figures 3.1Ba and 3.1Bb) were also characterized by numerous Bragg reflections in addition to the broad features previously

indicated, no conclusive matches were identified for most of these peaks. These two samples appeared to share a low angle reflection at ~ 4.22 degrees (d = ~ 9.4 Å), but most of the other low angle reflections were not common to both patterns. We therefore suggest that the 1-day samples may be composed of a mixture of metastable phases that were not well characterized by previous studies. Most of the peaks observed in the 1-day patterns were not visible in the 1-week patterns, confirming the metastable nature of the 1-day precipitates.

The 1-week patterns (Figure 3.1Ca and 3.1Cb) and all the 40 mM samples displayed halite (NaCl) Bragg reflections; this is presumed to be from residual salts from the media. In addition to this, the 1-week 40 mM sample was also characterized by the presence of nickelboussingaultite $(NH_4)_2Ni(SO_4)_2(H_2O)_6$ plus additional un-matched reflections, whereas the 1-week 10 mM sample showed sharp reflections due to thenardite (Na_2SO_4). Lattice parameters for nickelboussingaultite were slightly different from the reference PDF card, due to either a different hydration state or slightly different ionic substitution. It is worth noting that the 1-week 10 mM diffraction pattern displayed sharper features associated with modifications of the poorly-crystalline NiS precursor (red asterisks in Figure 3.1Cb). These features were particularly accentuated at ~ 13.41 degrees (d ~ 2.95 Å) and ~ 23.37 degrees (d ~ 1.70 Å). No single nickel sulfide with peaks corresponding to both the 2.95 Å and 1.70 Å d-spacing was found. Polydymite [more intense reflections (311) and (440) at 2.87 Å and 1.68 Å, respectively] and α-NiS [reflections (100) and (110) at 2.98 Å and 1.72 Å, respectively] were the phases that displayed the most similar patterns (Figure 3.1Ca). The presence of these "sharper" peaks associated with modifications of the poorly crystalline NiS precursor may indicate evolution of the poorly crystalline precursor towards the development of higher-order Ni sulfides with time. In similar experiments, Mansor et al. (2019) observed a distinct increase in crystallinity of biogenic Ni sulfide nanoparticles over a period of ~6 days.

Comparison between biotic and abiotic Ni sulfide precipitation experiments indicated the biogenic products were characterized by enhanced dimensions and crystallinity relative to their

abiogenic counterparts (Mansor et al., 2019). Similar findings were reported for SRB-mediated Zn sulfide formation (Xu et al., 2016). The development of more crystalline phases associated with the biotic precipitation of sulfides was linked to the formation of a low pH micro-environment around the bacteria cell walls and to the presence of organic compounds secreted by SRB (Mansor et al., 2019). The micro-environment around the bacteria cell walls, which chemically differed from the bulk circumneutral pH experimental conditions, was also suggested to favour the precipitation of low-pH (pH ≤ 5) Ni sulfide minerals, such as polydymite and vaseite (Mansor et al., 2019). These minerals were characterized by a metastable nature under our experimental conditions.

All of the 40 mM powder X-ray diffraction patterns displayed broad, low angle reflections at ~2.25 degrees (d ~ 17.5 Å) and ~3.65 degrees (d ~ 10.8 Å). These reflections, which were probably from the same phase due to comparable broadening and intensity ratios, had similarities with the patterns of clays, although no obvious matches were found in the PDF database. Bacterial microcolonies are known to mediate the formation of clay minerals (Konhauser and Urrutia, 1999; Tazaki, 2005; Fiore et al., 2011). Formation of colloidal clay-like phases (often Fe-bearing aluminosilicates) is favoured by the presence of bacteria and their metabolic products (Fiore et al., 2011), and these poorly-crystalline precursors may convert to more ordered phases over time (Konhauser and Urrutia, 1999; Tazaki, 2005; Fiore et al., 2011). The presence of clay material was supported by SEM-EDS analysis (Figure S3.3).

SEM-EDS analysis, which was performed on both the freeze-dried and freshly sampled 10-mM and 40-mM 1-week solid materials, also showed that the larger grains, predominantly occurring as the shiny precipitate, were made of aggregates of Ni sulfides with different habits and composition (Figures S3.4 to S3.6), which is consistent with the PXRD results. These higher-order aggregates were closely associated with bacterial biofilms which formed predominantly on the bottle sides. Biofilms are microbial multicellular aggregates that attach to surfaces and can often immobilize metal ions (Singh et al., 2006). Although bacterially-mediated sulfate-

reduction by SRB was the main process responsible for Ni removal from solution in the present study, extracellular polymeric substances (EPS), secreted by bacteria and bacterial cell components, are able to bind Ni and other heavy metals thus creating additional precipitation sites (Sitte et al., 2013; Mansor et al., 2019; Kumar and Pakshirajan, 2020). The SEM-EDS analysis of *D. desulfuricans* in our study showed Ni-sulfide precipitates surrounding the microorganisms (Figure S3.7). Precipitation of metal sulfides on bacterial surface is known to act as a protection for SRB, enhancing their tolerance to the toxic effects of heavy metals (Castillo et al., 2012).

The finest grain-size portion of the solid product mainly occurred as black precipitates that accumulated at the bottom of the bottles. Lattice fringe spacing measurements, derived from the TEM study, confirmed the polycrystalline nature of these precipitates (Figure S3.8 A and B).

Although the final experimental batches were filled with a modified medium containing no Fe, SEM-EDS results indicated a small amount of Fe was carried over from previous batches during subculturing, and Fe coprecipitated with and/or substituted Ni in the solid phase (Figure S3.6).

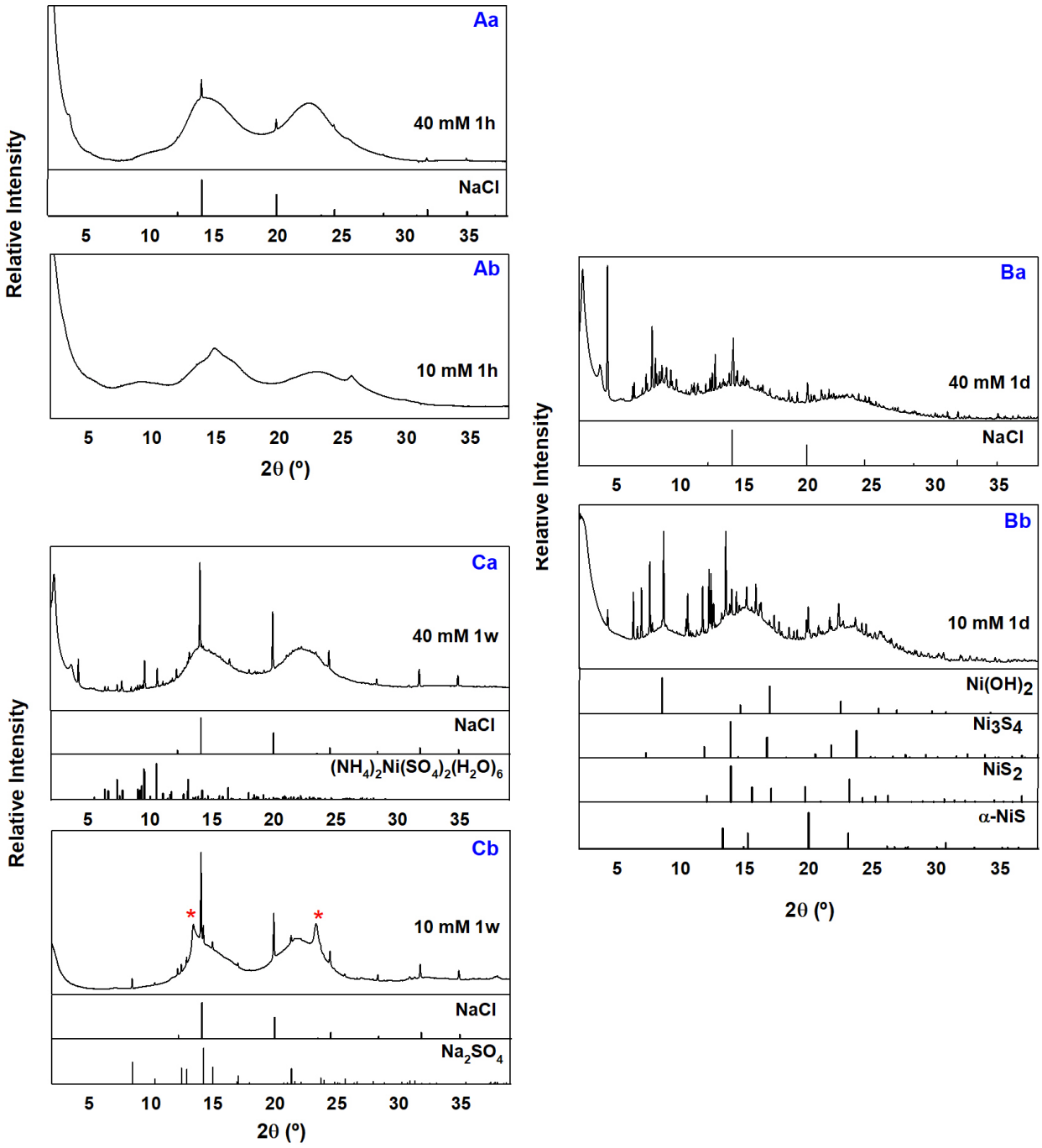

Figure 3.1: X-ray diffraction patterns of Ni precipitates: Aa) 40 mM Ni solid sample collected after 1 hour. Halite, NaCl (04-016-2944) Ab) 10 mM Ni solid sample collected after 1 hour. Ba) 40 mM Ni solid sample collected after 1 day. Halite, NaCl (04-016-2944) Bb) 10 mM Ni solid sample collected after 1 day. Theophrastite, $Ni(OH)_2$(04-013-3641), polydymite, Ni_3S_4 (04-004-5623), vaesite, NiS_2 (04-003-1992), α-NiS (04-002-6886). Ca) 40 mM Ni solid sample collected after 1 week. Halite, NaCl (04-016-2944), nickelboussingaultite, $(NH_4)_2Ni(SO_4)_2(H_2O)_6$ (04-007-5461). Cb) 10 mM Ni solid sample collected after 1 week. Halite, NaCl (04-016-2944), thenardite, Na_2SO_4 (04-010-2457). Red asterisk (*) indicates peaks corresponding to modifications of the poorly crystalline NiS precursor.

3.2.3. Isotope fractionation.

The magnitude of Ni isotope fractionation between Ni in solution and Ni associated with the solid phase was investigated by varying the initial concentrations of Ni in solution, which resulted in wide ranging amounts of Ni precipitate. The isotope results are reported in Table S3.1.

Figure 3.2 displays the measured δ^{60}Ni values corresponding to the fractions of Ni in solution and in the associated solid phase. The isotope data were fitted with both reversible equilibrium and Rayleigh fractionation models. The black solid lines are the linear best-fit to the data, whereas the black dashed curves are the best-fit Rayleigh trends $\varepsilon = -1‰$ (Fig. 3.2). According to the fitting results, it is reasonable to assume the data reflected equilibrium, closed-system fractionation (linear trends) with continuous exchange between the aqueous and the solid pools. An average magnitude of $\Delta^{60}Ni_{solid\text{-}aq} = -1.99‰$ was determined for the data set.

The data show a partition of light Ni isotopes in the solid phase compared to the initial solution, which is followed by enrichment in heavy isotopes of the residual aqueous Ni fractions. Enrichment in the heavier isotope associated with the aqueous fraction of Ni was observed in abiotic Ni sulfide precipitation experiments (Parigi et al., Chapter 2). The isotopic fractionation in the abiotic NiS precipitation experiments was fit with a Rayleigh curve yielding a fractionation factor of $\varepsilon = -0.73‰$ (Parigi et al., Chapter 2). Fujii et al. (2011) and (2014) also observed that lighter Ni isotopes preferentially partition into the sulfide species, reporting the equilibrium fractionation factors between the dissolved species Ni^{2+} and $Ni(HS)^{+}$ as $\Delta^{60}Ni_{Ni2+\text{-}Ni(HS)+} = +0.68‰$ and $\Delta^{60}Ni_{Ni2+\text{-}Ni(HS)+} = +0.66‰$ at 25°C, respectively.

Due to the complexity of the investigated system, it is not possible to attribute the magnitude of the isotopic fractionation to a single Ni sulfide precipitation process. Although Ni precipitation as sulfide phases was the main mechanism of Ni removal from solution, it is likely the fractionation measured in our experiments resulted from a combination of multiple Ni attenuation processes present in the SRB system. As previously discussed, bacteria cell walls

and EPS can bind heavy metals such as Ni, thus providing precipitation sites for metals and sulfide phases. Interactions between SRB and Ni might induce Ni isotope fractionation before the precipitation of sulfide phases occurs. Nickel adsorption to and coprecipitation with clay-like phases, whose bio-induced formation was detected in the experiment, might also contribute to the measured isotope fractionations. Ni adsorption to minerals was documented to cause the enrichment of heavy Ni isotopes in solution compared to the solid phases and to generate significant Ni isotope fractionation (Wasylenki et al., 2015; Wang and Wasylenki, 2017; Gueguen et al., 2018; Castillo Alvarez et al., 2020; Sorensen et al., 2020). For example, in a recent study, adsorption of Ni to the mineral birnessite induced the largest fractionation factors observed for Ni to date ($\Delta^{60}_{\text{min-aq}}$ ranging from −2.76‰ to −3.35‰; Sorensen et al., 2020). Furthermore, Liu et al. (2018) estimated the influence of Fe substitution on equilibrium Ni isotope fractionation in Ni sulfide minerals. Fe substitution for Ni yielded a decrease of the reduced partition function ratios of $^{60}Ni/^{58}Ni$. Thus, the presence of Fe, which characterized the investigated system, cannot be ignored as changes in the Fe/Ni ratio have a considerable influence on Ni isotope fractionation (Liu et al., 2018).

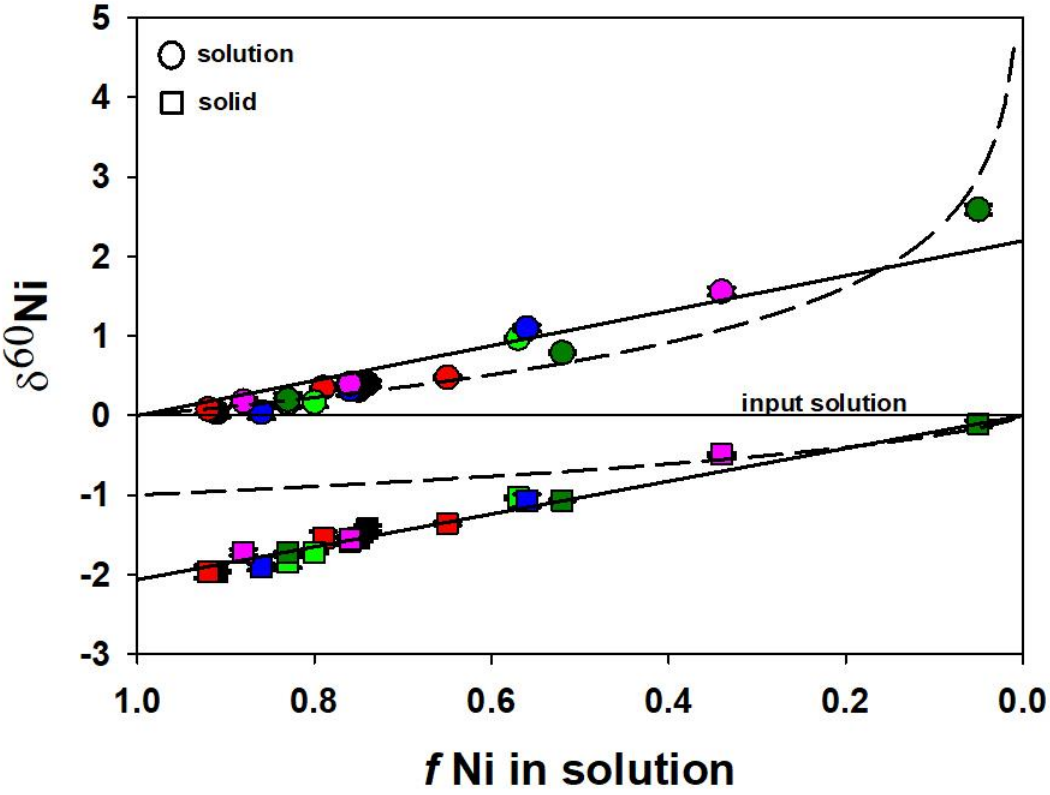

Figure 3.2: Ni (δ^{60}Ni) isotope fractionation relative to the input solution Ni concentration versus the fraction of Ni remaining in solution (f). The black straight lines represent the closed-system equilibrium fractionation trends yielding $\Delta^{60}Ni_{solid\text{-}aq}$ = −1.99‰; the dash curves are Rayleigh trends for ε^{60}Ni = −1‰. Black symbols correspond to the 40 mM samples; Red symbols correspond to the 30 mM samples; light green symbols correspond to the 25 mM samples; blue symbols correspond to the 20 mM samples; pink symbols correspond to the 15 mM samples; dark grey symbols correspond to the 10 mM samples. The error bars represent 2σ from three analytical events.

3.3. Environmental implications.

Due to the close interaction between biofilms and metal ions in solution, SRB are considered a valuable tool in passive treatment remediation processes. However, because of the complexity of processes occurring within biofilms, it is challenging to characterize the multiplicity of mechanisms involved in the bio-mediated attenuation of Ni and other heavy metals and to predict the long term stability and efficiency of bio-remediation systems (Chirwa, 2012). As a result, it is reasonable to ascribe the extent of fractionation measured in the present study to a combination of mechanisms involved in removing Ni from solution. Additionally, bacterial biofilm formation is influenced by changes in geochemical and physical parameters, such as: pH, nutrient availability and oxygen concentration (Singh et al., 2006). Interactions with

complex microbial communities (in contrast with pure cultures such as the one used in the present study) may also result in differences in the isotopic signatures. Thus, future studies, that aim to determine Ni isotope fractionation under varying experimental initial conditions, would be beneficial to further understand which mechanisms have the greatest impact on Ni isotope signatures in the SRB system and in more complex microbial communities.

CHAPTER 4

Mechanisms of Ni removal from contaminated groundwater by calcite using X-ray absorption spectroscopy and Ni isotope measurements

Roberta Parigi, Ning Chen, Peng Liu, Carol J. Ptaceck and David W. Blowes

Summary

A flow-through cell experiment was conducted to identify mechanisms of Ni removal by calcite through study of changes in Ni speciation during the treatment of simulated Ni-contaminated groundwater. Synthetic Ni-contaminated groundwater was pumped through a custom-made polyethylene (HDPE) flow-through cell packed with crushed natural calcite minerals. Effluent samples were collected to determine concentrations of anions, cations, and for Ni isotope-ratio measurement. X-ray absorption spectroscopy (XAS) analysis was performed on chosen spots of the solid phase along the length of the flow-through cell. Isotope data indicated multiple mechanisms affect Ni removal in the FTC system. Ni adsorption to and coprecipitation with calcite dominated the early part of the FTC experiment and yielded a fractionation factor of $\varepsilon = -0.5‰$. Subsequently, Ni precipitation as a Ni-hydroxide phase became the major process controlling Ni removal, resulting in a fractionation factor $\varepsilon = -0.4‰$. XAS analysis confirmed the presence of both $Ni(OH)_2$ and $(Ni,Ca)CO_3$ types of Ni local structural environments. Results from the present study highlight the potential of Ni isotope analysis as an auxiliary tool in the characterization of the processes involved in the attenuation of Ni from the environment.

4.1. INTRODUCTION

Contamination of water bodies by heavy metals is a major concern associated with metal finishing, mining and mineral processing, coal mining and oil refining (Jha et al., 2005). Nickel and Ni compounds have many industrial and commercial uses, thus significant amounts of Ni

can be released to the environment, possibly posing a severe threat to ecosystems. Nickel is a nutritionally essential trace metal for several organisms and plants, however it has been shown that the exposure to highly Ni-polluted environments can yield to a variety of pathological effects in living organisms (Genchi et al., 2020). Consequently, implementing Ni control measures is of great importance to minimize the potential environmental impacts.

Passive remediation techniques provide a site-specific, low-cost and effective approach to treat contaminated groundwater (Blowes et al., 2000). Permeable reactive barriers (PRBs) containing different types of reactive material (i.e: Zero-valent iron (ZVI), limestone, and biological barriers) have been used to treat dissolved metals (Blowes et al., 2000). Specifically, calcite has shown to play a significant role in the immobilization of divalent metal cations affecting water bodies (Morse, 1986; Comans and Middelburg, 1987; Davis et al., 1987; Zachara et al., 1989; Zachara et al., 1991; Stipp et al., 1992; Martin-Garin et al., 2003), and studies involving calcite interactions (Zachara et al., 1989; Zavarin and Doner, 1998; Hoffmann and Stipp, 2001; Lakshtanov and Stipp, 2007; Belova et al., 2014) have highlighted the potential sequestration of Ni with $CaCO_3$.

Metal stable isotope analysis has emerged as a promising tool to discern metal attenuation processes. Recent studies have applied non-traditional stable isotope analysis to assess the efficacy of remediation activities with a focus on subsurface environments (Jamieson-Hanes et al., 2014 and 2017; Veeramani et al., 2015; Shrimpton et al., 2018; Parigi et al., Chapter 2 and Chapter 3).Various chemical processes (redox reactions, precipitation, dissolution, sorption, and complexation) are known to generate distinctive metal stable isotope fractionations (Wiederhold, 2015). Recent research has evaluated Ni isotope fractionation during adsorption (Wasylenki et al., 2015; Wang and Wasylenki, 2017; Gueguen et al., 2018; Castillo Alvarez et al., 2020; Sorensen et al.; 2020) and (co)precipitation (Wasylenki et al., 2015; Wang and Wasylenki, 2017; Parigi et al., Chapter 2 and Chapter 3) experiments, showing a preferential enrichment of heavier Ni isotopes into solution for almost all the systems investigated. Results

displayed fractionation factors $\Delta^{60}Ni_{min\text{-}aq}$ as high as −2.76 and −3.35‰, associated with sorption of Ni to the mineral birnessite[26], whereas a magnitude of $\Delta^{60}Ni_{solid\text{-}sol}$ = −1.99‰ was determined for microbially-mediated attenuation of Ni from solution (Parigi et al., Chapter 3). The present study focuses on the mechanisms of Ni removal during the treatment of simulated Ni-contaminated groundwater flowing through calcite, material utilized in PRBs, with the support of nickel isotope analysis and X-ray absorption spectroscopy. The study of Ni isotope fractionation during interaction with calcite under dynamic flow conditions will further improve our understanding of the possible mechanisms affecting Ni isotope signatures in environmental settings such as passive remediation systems.

4.2. MATERIALS AND METHOD

4.2.1. Experimental Design

A custom-made high-density polyethylene (HDPE) flow-through cell (FTC) was packed with crushed natural calcite mineral (size: ≤ 300 μm; BET surface area: 0.0818 $m^2\ g^{-1}$). The cell dimensions were 14.0 × 17.8 × 6.4 cm, with an open window (3.8 × 7.6 × 1.3 cm) on one side to contain the material used in the experiment. This window was covered with Kapton film (0.0762 mm thick) to allow collection of X-ray Absorption Spectroscopy (XAS) spectra. A HDPE frame was secured onto the face of the cell to hold the Kapton film in place and a rubber O-ring was used to prevent any potential gas and/or water leaks. Sealed connections were installed at the bottom and top of the cell for inflow and outflow, respectively. Glass wool and Nitex screen (mesh opening: 210 μm) were installed at the influent and effluent ports to prevent clogging. A similar FTC design was also implemented in previous experiments (Jamieson-Hanes et al., 2014 and 2017; Shrimpton et al., 2018).

Once saturation conditions were reached by pumping ultrapure water (<18 μS) through the cell, an input solution, consisting of 48 mg L^{-1} Ni, was pumped upward through the cell using a peristaltic pump (Ismatec, Cole-Palmer, Montreal, QC) with 0.25 mm ID Pharmed pump tubing (Cole-Palmer, Vernon Hills, IL). A pump speed of 10 rpm (flow rate of ~ 3 mL/hr) was

chosen and led to Ni breakthrough after around 80 hrs (Figure 4.1). Effluent samples were collected with a fraction collector.

The input solution, prepared by dissolving pure grade $NiCl_2 \cdot 6H_2O$ salt in ultrapure water, was bubbled with air during the experiment to improve gas exchange and to keep the initial pH stable.

Effluent samples were filtered (0.2 μm filters from Acrodisc, Pall, UK) and refrigerated at 4 °C. Samples for cation and isotope determination were acidified with trace-metal grade HNO_3 (Omnitrace ultra, EMD Millipore), whereas samples for anion analysis were not acidified. Due to the low volume of the effluent samples (~ 3 mL/hour), measurements of pH were conducted on only some unfiltered samples, whereas alkalinity measurements could not be performed.

4.2.2. X-ray absorption spectroscopy (XAS)

X-ray absorption spectroscopy (XAS) analysis was performed on the FTC at the Hard X-ray Micro-Analysis (HXMA) beamline at the Canadian Light Source (CLS) synchrotron facility (Jiang et al., 2007). Before proceeding to the acquisition of the spectra, ultrapure water was pumped through the cell to facilitate the collection of spectra belonging to the Ni bound to the solid phase. XAS analysis was first performed on the input solution. The collection spots in the FTC were chosen after mapping the entire cell.

The CLS storage ring was run at the 250 mA operation mode with three injections per day. The HXMA beamline was configured in its focused mode with Rh mirrors (collimating and focusing mirrors) in the X-ray beam path. Monochromatic X-rays were provided using a double crystal Si (220) monochromator. The second crystal of the monochromator was detuned by 50% at the end of the X-ray absorption fine structure (XAFS) scan to minimize the higher harmonic compounds in the incident X-ray beam. The scan step size for the pre-edge, X-ray Absorption Near Edge Structure (XANES), and Extended X-ray Absorption Fine Structure (EXAFS) regions were 10 eV/step, 0.25 eV/step, and $0.05 Å^{-1}$/step, respectively. Multi-scan data were collected to improve signal-to-noise ratio and support reliable data analysis. During

the experiment the spectra were collected in fluorescence mode using a 32 element Ge detector. The initial monochromator energy was calibrated at 8333 eV of Ni K-edge by using Ni metallic foil from EXAFS Materials (http://exafsmaterials.com/). Afterwards, the same metallic foil was positioned throughout the entire experiment between the two ion chamber detectors, I1 and I2, downstream of the sample, to achieve in-step energy calibration for each individual XAFS scan. The ion chamber detectors were filled with pure He gas to keep the detecting system linear. Data reduction, including energy calibration, multiple scan averaging, background subtraction, and normalization, was accomplished by using the Athena software package (Ravel and Newville, 2005). FEFF7. 02 was employed to calculate phase and amplitude functions of the corresponding XAFS backscattering (Rehr and Albers, 2000). R space curve fitting was performed by using WinXAS version 2.3 (Ressler, 1997).

Confocal micro-X-ray fluorescence imaging (CMXRFI) analysis was performed at the Advanced Photon Source (APS; Argonne National Laboratory, USA Lemont, IL), Beamline 20-ID, on calcite particles sampled from different spots of the FTC. The particles were attached to quartz slides (22 × 22 mm^2) with epoxy (Devcon 14250, USA) for analysis. The quartz slides were mounted on a stage oriented at an angle of 34° with the incident beam. The incident beam was focused with KB mirrors down to ~2 μm × 2 μm. X-ray fluorescence (XRF) spectra were collected by a Si-drift Vortex detector. A Ge collimating channel array optic unit was installed in front of the detector. Further details on CMXRFI setup and method for data collection can be found in Liu et al., 2017.

4.2.3. Isotope measurements

Preconcentration and Ni isotope analysis were performed following the procedures described in Parigi et al. (Chapter 2). Samples combined with a $^{61}Ni - ^{62}Ni$ double-spike solution were purified adopting a two-step chromatography procedure: (1) separation of Fe using the BioRad AG MP-1M (100 – 200 mesh, chloride form) anion exchange resin; (2) separation of Ni from

the remaining matrix elements using a Ni-specific resin from Eichrom Technologies. Eluted Ni fractions were evaporated and finally dissolved in 3% HNO_3 for isotope analysis.

Nickel isotope compositions were measured by a Thermo Scientific Neptune MC-ICP-MS coupled with an APEXQ desolvation introduction system (ESI). Polyatomic interferences were resolved by measuring on the low mass shoulders of the peaks in high resolution mode. Corrected ratios were calculated using the method described by Siebert et al. (2001), and Ni isotope values were expressed as δ^{60}Ni in per mill (‰) relative to the Ni international isotopic standard NIST SRM 986:

$$\delta^{60}\mathrm{Ni} = \left[\frac{(^{60}\mathrm{Ni}/^{58}\mathrm{Ni})_{\mathrm{sample}}}{(^{60}\mathrm{Ni}/^{58}\mathrm{Ni})_{\mathrm{standard}}} - 1\right] \mathrm{x}\, 1000 \qquad (1)$$

Results were normalized to the average value of NIST SRM 986 measured before and after each sample. The long-term analytical reproducibility of the standard NIST SRM986 was determined to be ±0.05‰. 2SD value of 0.05‰ (long-term reproducibility) was used when the 2SD, related to three measurements for each sample, was < 0.05‰.

The measured δ^{60}Ni for the input solution $NiCl_2$ was −0.17‰ ± 0.05‰. For the purposes of plotting, and data interpretation, samples were normalized to the input solution value, yielding a $\delta^{60}Ni_{NiCl2}$ = 0.00 ± 0.05‰.

4.3. RESULTS AND DISCUSSION

4.3.1. Geochemical Analysis

FTC effluent pH increased over the course of the experiment from input values of 5.8 until stabilizing at values of 7.8 after ~ 36 hours (Figure 4.1A).

From an initial complete removal of Ni from solution, Ni effluent concentrations began to increase approaching the input concentration after about 80 hours (Ni breakthrough curve, Figure 4.1A). In contrast, Ca effluent concentrations exhibited a rapid initial increase followed

by a slower decrease until reaching a plateau after ~ 40 hours. Details can be found in the Supporting Information (Table S4.1).

Figure 4.1B, which displays Ni concentrations plotted versus Ca concentrations expressed in mM, suggests the presence of three main stages (a, b, and c in Figure 4.1A and Figure 4.1B) constituting the FTC experiment. Stage a, which encompasses the first 12 hours of the experiment, is characterized by dissolution of the calcite present inside the cell due to undersaturation with respect to $CaCO_3$ of the input solution. Calcite dissolution resulted in a rise in pH and Ca release into solution, whereas Ni was removed likely by sorption to the carbonate mineral. Hoffman and Stipp (200)1 observed Ni being adsorbed by calcite in undersaturated solutions, despite calcite dissolution was taking place.

After stage a, dominated by calcite dissolution, and where Ca reached a maximum value of 40.9 mg L^{-1} in the effluent, Ca likely reprecipitated with CO_3^{2-} following supersaturation with respect to calcite (stage b). Stage b is characterized by Ni and Ca exhibiting a significant negative correlation ($R^2 = 0.99$; Figure 4.2), therefore suggesting Ni coprecipitation with calcite as the main mechanism of Ni removal during this phase. Ni is known to be incorporated into the calcite structure when the solution is undersaturated with respect to pure Ni phases, such as $NiCO_{3(s)}$, and $Ni(OH)_{2(s)}$ (Lakshtanov and Stipp, 2007; Andersson et al., 2014). However, if the precipitation rate of calcite is fast, some of the adsorbed Ni may be captured by the freshly formed calcium carbonate mineral (Lakshtanov and Stipp, 2007).

The change in the slope of Ni breakthrough and Ca curves, which is displayed at the boundary between stages b and c, suggests the presence of a different attenuation process/es which developed during the last stage (c) of the FTC experiment: it is possible Ni began precipitating as $Ni(OH)_2$. Studies conducted on Ni sorption experiments linked the slow reaction stage of the adsorption process to the formation of surface precipitates (Scheidegger and Sparks, 1996; Scheidegger et al., 1998; Scheinost et al., 1999). In particular, XAFS data analysis, performed on the aforementioned Ni sorption experiments, indicated the formation of Ni oxy- or hydroxy-

bridged multinuclear type of surface complexes at reaction conditions even below the solubility product of $Ni(OH)_{2(s)}$ (Scheidegger and Sparks, 1996; Scheidegger et al., 1998). An increase in the average size of multinuclear Ni clusters was also observed, suggested by the increase of Ni–Ni coordination number, with increased Ni loading (Scheidegger and Sparks, 1996; Scheidegger et al., 1998). Similar findings were reported by Zavarin and Doner (1998) in experiments involving Ni sorption to and coprecipitation with calcite.

4.3.2. Solid-phase Ni speciation.

The Ni spectra collected from the cell showed differences from the Ni spectra associated with the input solution, and although the measurements of the Ni K-edge signal indicated Ni relative concentration changes across the FTC system, experimental data from XANES, EXAFS in k space, and EXAFS in R space (Figure S4.1) showed no significant changes in the Ni spectra collected at different spots across the FTC system, suggesting no changes in Ni structural environment occurred inside the cell.

R space curve fitting, performed over the EXAFS data collected from 11 detecting points across the cell window, indicated a main theophrastite-type local structural environment for Ni (Table 4.1). The fitting quality (comparison between ExpData vs Feff modeling in both the magnitude and the imaginary part of the Fourier transform) can be found in Figure S4.2, in the Supporting Information.

The estimated Ni-O and Ni-Ni distances are in agreement with previously published data (Pandyia et al., 1990; Defontaine et al., 2003; Wilkin and Rogers, 2010; Han et al., 2019). Feff modeling based on the structural models reported in Figure 4.2 indicates that between the two types of Ni local structural environments, features A, D, and G are unique to a theophrastite-type of Ni species. The modeling also shows that the well resolved feature C can only be attributed to the calcite-type of Ni local structural environment, and suggests that Ni substitution at the Ca site of the calcite structure extended to the neighboring Ca sites. Ni in the FTC system is therefore characterized by two different types of local Ni structural

environments: a main one (theophrastite-type structural environment), and a secondary one (calcite-type structural environment).

Feff modeling was also performed to estimate the size of the theophrastite particles (Figure S4.3). Results suggest theophrastite precipitated in the FTC as surface coatings onto the calcite particles, and the coating displayed a thickness of, at least, 1 nm. Furthermore, Feff modeling indicated the presence of a 'transition zone' impacted by Ni-Ca replacement located between the surface coating layer and the calcite substrate. As the Ni-Ni bond distance was estimated to be 3.6 Å by Feff modeling, we suggest the 'transition zone' had a thickness of, at least, 0.5 nm (including the coordinated O and C atoms).

CMXRFI analysis showed the presence of Ni accumulated on the calcite surface (Figure 4.3). The spectra collected with confocal analysis at different depths on calcite particles did not show differences from the spectra related to the bulk solid phase at the HXMA beamline, confirming the presence of a $Ni(OH)_2$ layer covering the calcite particles. It is likely the 'transition zone' could not be reached during CMXRFI analysis due to the high Ni concentration in the theophrastite layer, and due to the high Ca absorbance.

Table 4.1: R space curve fitting results from 11 detecting points (FTC2) across the cell window

Name	CN1	R1 (Ni-O) Å	σ^2 (Å^2)1	CN2	R2(Ni-Ni) Å	σ^2 (Å^2)2
FTC2D	6.0	2.09	0.0035	6.0	3.12	0.0100*
FTC2C	6.0	2.13	0.0100*	6.0	3.14	0.0100*
FTC2G	6.0	2.03	0.0091	6.0	3.10	0.0100*
FTC2L	6.0	2.06	0.0061	6.0	3.11	0.0100*
FTC2B	6.0	2.11	0.0100*	6.0	3.13	0.0099
FTC2E	6.0	2.07	0.0054	6.0	3.11	0.0092
FTC2H	6.0	2.10	0.0071	6.0	3.13	0.0087
FTC2K	6.0	2.03	0.0090	6.0	3.09	0.0100*
FTC2A	6.0	2.09	0.0080	6.0	3.11	0.0100*
FTC2J	6.0	2.05	0.0043	6.0	3.10	0.0087
FTC2I	6.0	2.07	0.0035	6.0	3.10	0.0097
Ave		2.08			3.11	

R1= Ni-O distance in Å ; R2= Ni-Ni distance in Å; CN1= Ni-O coordination number; CN2= Ni-Ni coordination number; σ^2 = Debye Waller factor. *Upper limit for σ^2 floating; CN1 and CN2 were constrained to 6.0 following the theophrastite crystal structure.

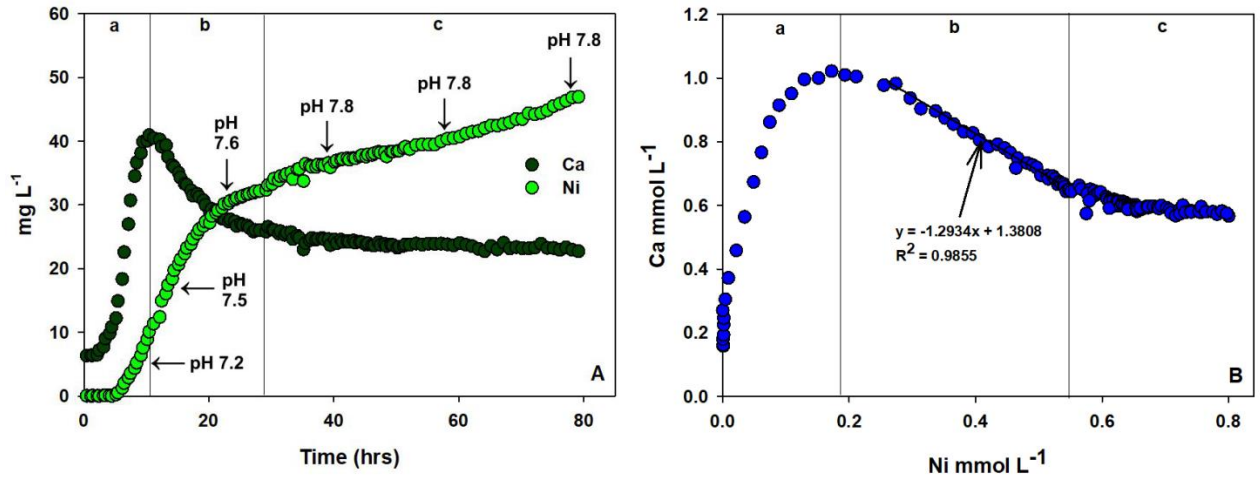

Figure 4.1: A) Effluent Ni and Ca concentrations (mg L^{-1}) vs. time (hours). B) Ni (mmol L^{-1}) vs. Ca (mmol L^{-1}). Three stages (a, b, c) were identified and are reported for the FTC system. Stage a: undersaturation with respect to calcite of the input solution leads to calcite dissolution. Ca release into solution and increase of pH. Sorption of Ni onto dissolving calcite. Stage b: FTC system reaches supersaturation with respect to calcite. $CaCO_3$ precipitation with Ni incorporation. Sorption of Ni onto calcite. Stage c: changes in the slopes of Ca and Ni breakthrough curves. Possible precipitation of Ni as $Ni(OH)_2$.

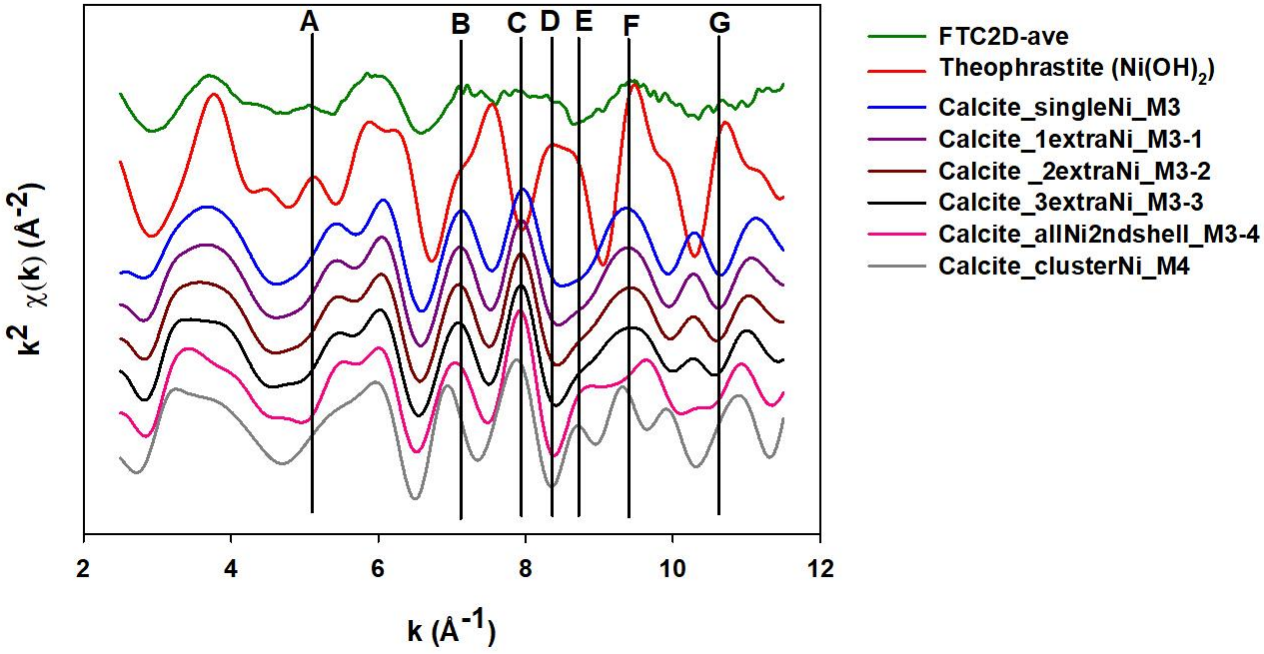

Figure 4.2: Feff modeling results based on the following structural models: M3) Isolated Ni replacing Ca in the calcite 2nd shell; M3-1) based on M3, 1 extra Ni replacing Ca in the calcite 2nd shell; M3-2) based on M3, 2 extra Ni replacing Ca in the calcite 2nd shell; M3-3) based on M3, 3 extra Ni replacing Ca in the calcite 2nd shell; M3-4) based on M3, full (6) Ni occupancy of the calcite 2nd shell; M4) R6.0Å cluster of calcite with all Ca sites within the cluster occupied by Ni. Finger print features were identified for Ni theophrastite-type local structural environment (A, D, and G), and Ni calcite-type local structural environment (B, C, and F). B and E features also reveal the extent of Ni occupancy in the calcite 2nd shell (up to half occupancy).

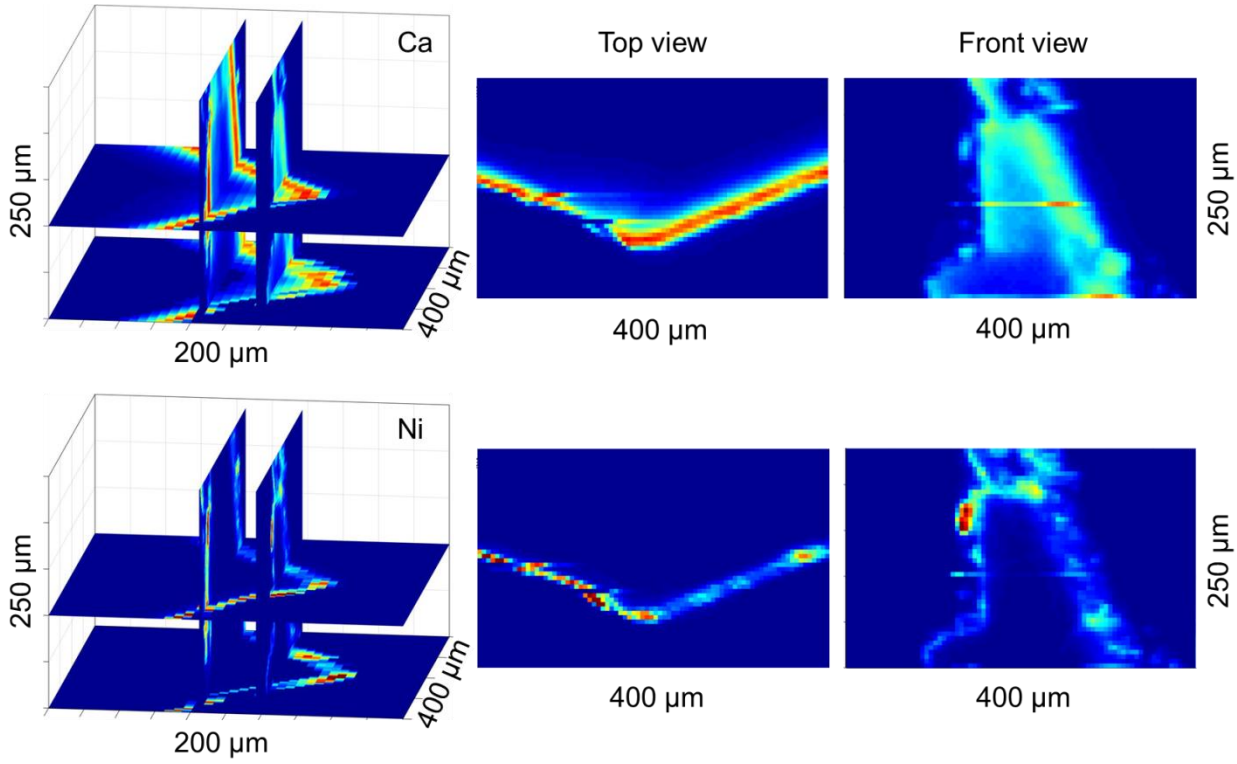

Figure 4.3: Confocal micro-X-ray fluorescence imaging (CMXRFI) displaying the attenuation-corrected absorbance distribution of Ca and Ni in a calcite particle from the FTC system. Left: three-dimensional view of the calcite particle. Right: top and front view of chosen slides of the calcite particle. Ni is accumulated on the particle surface.

4.3.3. Ni isotope fractionation.

Isotope compositions of dissolved Ni and the fraction of Ni remaining in solution (C/C_0) are plotted as a function of time (hrs) in Figure 4.4. The results indicate lighter Ni isotopes were preferentially retained by the solid phase, which resulted in the enrichment in heavier isotopes of the remaining unreacted Ni pool. Greater enrichment of ^{60}Ni over ^{58}Ni in the effluent compared to the input solution, was associated with higher rates of Ni removal (a and b stages). Isotope results show a change in the isotope trend at the boundary between stages b and c. The change in the trend of Ni isotope data could be associated with a change in the removal mechanism affecting Ni in solution between the two stages b and c, as also suggested by the change in the slopes of Ca and Ni curves happening at the same time (Figure 4.1A). $\delta^{60}Ni$ values plotted versus C/C_0 are displayed in Figure 4.5. Ni isotope data were modelled using a Rayleigh equation, and best-fit α values were calculated via linear regression. The best-fit curve, including all isotope data, yielded a fractionation factor ε of −0.5‰ (black dashed line in Figure 4.5). Because the isotope results associated with stage c seemed to slightly deviate from the best-fit Rayleigh fractionation curve (ε = −0.5‰), isotope data were split in two groups (stages a+b, and stage c) and modelled independently (Figure S4.4 A, B, and C). Although resulting in a fractionation factor ε of −0.5‰ equal to the fractionation factor determined for the whole set of data, the best-fit Rayleigh trend for the "stages a+b" isotope data showed a significant improvement in the regression R^2 value (from 0.85 to 0.99; Figure S4.4A and B). In contrast, "stage c" isotope data were best represented by a Rayleigh curve yielding a fractionation factor ε of −0.4‰ (green solid line in Figure 4.5). It must be noted the linear best fit to "stage c" isotope values was not forced to intersect the initial stock composition (Figure S4.4C), therefore the ε = −0.4‰ curve does not intersect the origin in Figure 4.5. These results indicate the mechanism affecting stage c of the FTC, were subsequent to the stage a and b mechanism/s, and represent Ni fractionation from a residual solution already enriched in heavier Ni isotopes (~0.1‰).

Ni isotope behaviour during Ni hydroxide and Ni hydroxycarbonate precipitation was evaluated by Parigi et al. (Chapter 2), during a series of batch experiments. Isotope results from these batch experiments were fit using the Rayleigh equation and yielded fractionation factors ε = −0.40‰ and −0.50‰ associated with Ni hydroxide and Ni hydroxycarbonate systems, respectively. The preferential partition of light Ni isotopes into the solid phases was suggested to be related to the distortion of the Ni-O octahedra constituting the structure of the Ni hydroxide and Ni hydroxycarbonate minerals (Parigi et al., Chapter 2). Studies conducted on Ni isotope fractionation during Ni adsorption to (Castillo Alvarez et al., 2020) and coprecipitation with (Castillo Alvarez, 2019) calcite have also documented the preferential association of lighter Ni isotopes with the solid phase. An equilibrium isotope fractionation factor $\Delta^{60}Ni_{calcite\text{-}fluid} = -0.52 \pm 0.16$‰ was determined for Ni adsorption to calcite (Castillo Alvarez et al., 2020), whereas the isotope fractionation factor related to Ni coprecipitation with calcite was reported to vary from −1 to −0.36‰ with increasing calcite precipitation rates (from −8.29 to −6.92 mol m^{-2} s^{-1}) (Castillo Alvarez, 2019).

The extent of Ni fractionation determined from these studies is consistent with the hypothesis of the occurrence of an early and an intermediate stage (stages a and b) characterized by Ni adsorption to and/or coprecipitation with calcite (ε = −0.5‰), and a final stage dominated by $Ni(OH)_2$ precipitation (ε = −0.4‰), in the FTC system.

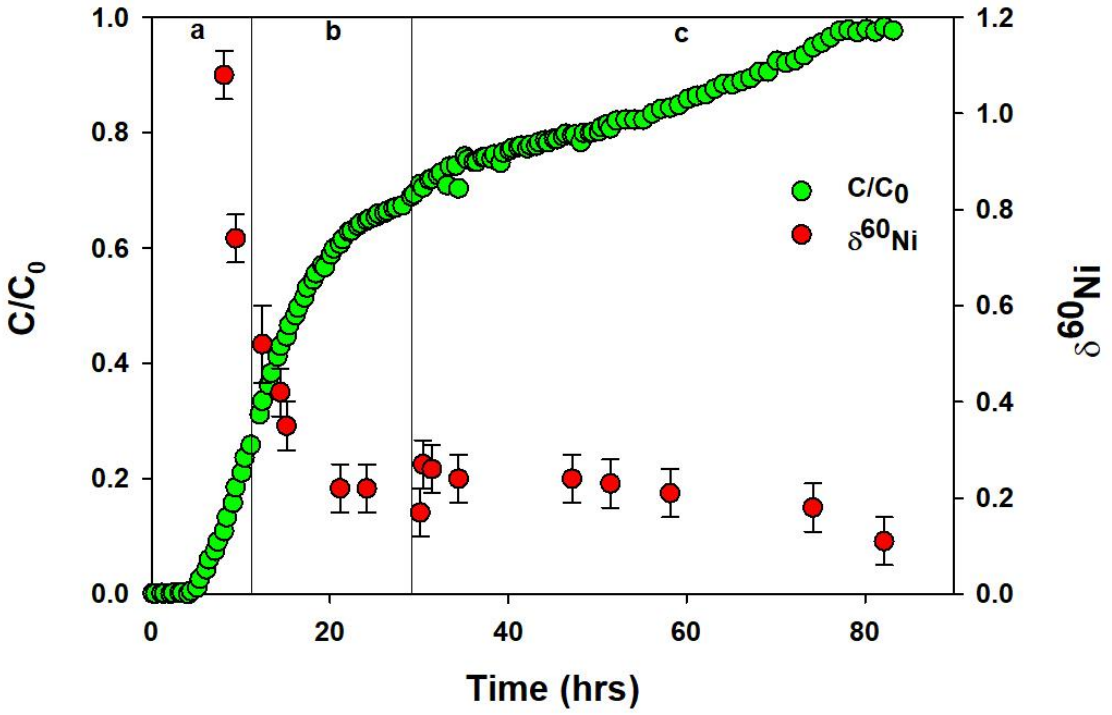

Figure 4.4: C/C_0 and $\delta^{60}Ni$ vs. time (hours). C are Ni effluent concentrations; C_0 is the initial Ni concentration. The error bars represent 2σ from three analytical events.

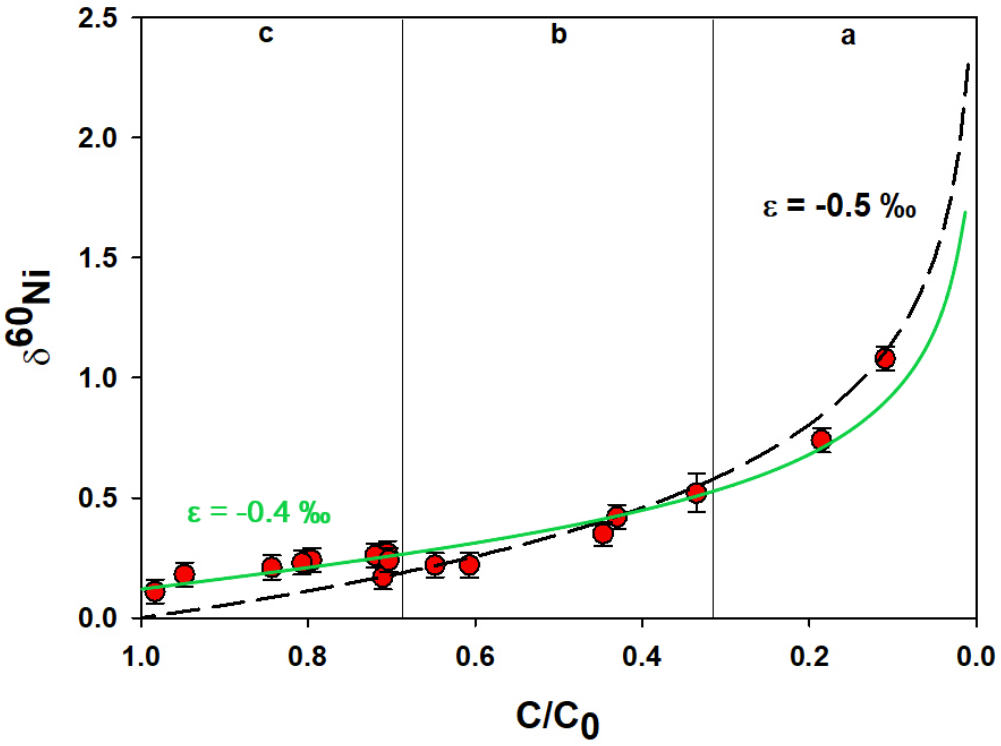

Figure 4.5: C/C_0 vs. $\delta^{60}Ni$. C are Ni effluent concentrations; C_0 is the initial concentration of Ni. The error bars represent 2σ from three analytical events. The dashed line shows the best-fit Rayleigh model yielding a fractionation factor ε = −0.5‰; the green solid line represents the best-fit Rayleigh model yielding a fractionation factor ε = −0.4‰.

4.4. Environmental implications.

Ni isotope analysis coupled with solid phase characterization can be an effective tool for the elucidation of the processes controlling the attenuation of Ni from the environment. Previous laboratory-scale research has employed batch experiments to determine the extent of Ni isotope fractionation associated with different processes, such as adsorption, complexation, and (co)precipitation. This study, involving Ni interaction with calcite under saturated flow conditions, offers an important addition to the characterization of Ni isotope behaviour in field systems, influenced by water flow and transport of dissolved components.

Understanding the processes governing Ni release, fate, and removal in the environment can yield benefits to and enhance the success of cost-effective and low-maintenance passive-treatment techniques applied to natural systems.

CHAPTER 5

Release and attenuation of Ni in mine tailings: X-ray absorption spectroscopy and Ni isotope measurements

Roberta Parigi, Justin R. Buis, Emily M. Saurette, Carol J. Ptacek and David W. Blowes

Summary

High concentrations of Ni and other dissolved constituents characterize the acidic pore-water in an unreclaimed portion of the Strathcona tailings impoundment (near Sudbury, ON, Canada) as a result of sulfide-mineral oxidation reactions. Understanding the processes which control the concentrations of the pore-water dissolved constituents can assist in the planning and evaluation of reclamation activities. Nickel stable isotope analysis of pore-water samples was used as an auxiliary tool to investigate the geochemical processes controlling Ni mobility within the Strathcona tailings impoundment. S and Ni X-ray absorption near edge structure (XANES) analyses, together with other geochemical and mineralogical techniques, were implemented to characterize solid tailings samples. Results indicate the presence of recent and paleo-oxidation phases related to multiple, subsequent tailings deposition events in the investigated area. The good correlation between Ni isotopic signatures and alteration zones highlights the potential of Ni stable isotope analysis as a tool to trace Ni cycling in the environment.

5.1. INTRODUCTION

Vast quantities of mineral processing waste are generated during the mining and processing of sulfide ores (Holmström et al., 1999; Lindsay et al., 2015). Tailings are a mixture of finely ground rocks (25 µm to 1.0 mm) and processing fluids produced from mills, washeries or concentrators during ore mineral extraction (Blowes et al., 2014; Kossoff, 2014; Lindsay et al., 2015).

Canadian Ni-Cu ore deposits have been exploited for over than 120 years (Rezaeia et al., 2017). Pyrrhotite (Po, $Fe_{1-x}S$), which contains up 1% Ni (Garg et al., 2017; Rezaeia et al., 2017), and pyrite (Py, FeS_2) are usually rejected to the tailings with other gangue minerals during the extraction of Ni and Cu from the ores (Blowes et al., 1991; Blowes et al., 2014). These sulfide minerals, which are unstable and oxidize when exposed to atmospheric oxygen, may generate acid mine drainage (AMD), metal-rich low-quality acidic water, from tailings impoundments into proximal ground- and surface water, thus potentially impacting these resources (Blowes and Jambor, 1990; Blowes et al., 1991; McGregor et al., 1998; Holmström et al., 1999; Johnson et al., 2000; Moncur et al., 2005; Gunsinger et al., 2006a and 2006b; Blowes et al., 2014; Lindsay et al., 2015).

AMD usually develops when the acid neutralization capacity of the tailings has terminated due to the complete dissolution and consumption of carbonate minerals present in the gangue material (Blowes, 1997; Lindsay et al., 2015). The acidic drainage and acid neutralization reactions occurring in mine tailings impoundments cause the release of high concentrations of dissolved metals (Fe, Al, Ni, Cu, Zn, Mn) and other constituents (mainly SO_4) to the tailings pore water (Blowes, 1997; Coggans et al., 1999; Lindsay et al., 2015). The fate of these dissolved constituents is closely influenced by precipitation-dissolution, sorption-desorption, and redox reactions developing in mine tailings systems (Blowes and Jambor, 1990; Blowes, 1997; McGregor et al., 1998; Gunsinger et al., 2006b; Lindsay et al., 2015). Precipitation of secondary minerals, such as Fe (oxy)hydroxides (jarosite, goethite, and ferrihydrite), Fe (hydroxy)sulfates (melanterite and rozenite), and gypsum [$CaSO_4 \bullet 2(H_2O)$], plays an important role in metal sequestration from tailings pore water. The precipitation of these secondary minerals can produce cemented zones, known as hard pan, which are sinks for dissolved metals (Blowes et al., 1991; Gunsinger et al., 2006b). Redox processes, including Fe oxidation and reduction, affect the thermodynamic stability of secondary minerals, and, consequently, determine the mobility of metals within the tailings. Dissolved Fe(III) is also

known to actively contribute to sulfide mineral oxidation (Blowes et al., 1991 and 1997; Moncur et al., 2005; Gunsinger et al., 2006a; Moncur et al., 2009; Blowes et al., 2014; Lindsay et al., 2015). Furthermore, microbially-mediated sulfate reduction and production of H_2S can lead to the precipitation of secondary metal-sulfide minerals under anoxic conditions. Pentlandite [Pn,$(Fe,Ni)_9S_8$], Ni-bearing pyrrhotite, and, to a lesser extent, nickeliferous pyrite and marcasite, are the main sources of dissolved Ni in mine tailings in the Sudbury region (Johnson et al.,2000). Leaching experiments conducted on tailings collected from two different sites in Sudbury (Ontario, Canada) concluded that 60% of the total Ni present in the tailings was hosted in pyrrhotite, whereas the remaining 40% was associated with pentlandite (Garg et al., 2017). It was also demonstrated that, in presence of Fe(III) and O_2, pyrrhotite and pentlandite were characterized by simultaneous dissolution, whereas, in the absence of Fe(III), preferential dissolution of pyrrhotite was taking place (Garg et al., 2017).

Metal stable isotope analysis has been demonstrated to provide valuable information on the cycling of metals and metalloids in the environment (Bullen, 2014; Wiederhold, 2015).

Ni stable isotope analysis has recently been applied to investigate Ni isotopic signatures during sorption (Wasylenki et al., 2015; Wang and Wasylenki, 2017; Gueguen et al., 2018; Castillo Alvarez et al., 2020; Sorensen et al., 2020) and (co)precipitation (Wasylenki et al., 2015; Wang and Wasylenki, 2017; Parigi et al., Chapters 2 and 3) processes, as well as to characterize Ni isotope fractionation during weathering of ultramafic rocks (Ratié et al., 2015 and 2018; Spivak-Birndorf et al., 2018), uptake by plants (Estrade et al., 2015; Ratié et al., 2019; Zelano et al., 2020), and microorganism activity (Cameron and Vance, 2009; Yang et al., 2020). Despite the recent advances and applications of Ni isotopes as environmental tracers, Ni isotope systematics is still at an early stage.

The objective of this study was to investigate the processes controlling the source and fate of Ni in mine waste systems by integrating Ni stable isotope analysis with synchrotron based spectroscopic studies and traditional geochemical and mineralogical techniques. The

application of Ni isotopic signatures to mine settings can provide insights into the release and natural attenuation of Ni, thus contributing to the improvement of appropriate remediation and containment plans.

5.2. MATERIALS AND METHODS

5.2.1. Sampling site

The Strathcona tailings impoundment is an active disposal facility situated near Sudbury (Ontario, Canada), and it has been receiving sulfide-rich tailings from the Strathcona mill, located about 1 km NE of the impoundment, since 1968 (Bain et al., 1998; Bain and Blowes, 2013). Although most of the tailings have been deposited subaqueously into Moose Lake from a spigot at the western end of the lake, as deposition has advanced, the area near the western spigotting point has become progressively elevated above lake level (Bain et al., 1998). The exposure of the tailings to oxygen caused the onset of sulfide oxidation reactions. Investigations conducted in the area determined that a 1 to 3 m thick unsaturated zone, developed in the beached tailings near the tailings deposition point, was affected by AMD (Bain and Blowes, 2013). Thus, with the purpose of decreasing the acidity and metal loadings from the tailings, a cover of low sulfur tailings slimes was placed over most of the beached tailings areas (Ecometrix, 2014).

The beached tailings samples, the object of the present study, were collected at the ML25 location (Fig.5.1) near the piezometer nests installed during an investigation conducted in 2012. The ML25 location is characterized by the presence of strongly oxidized tailings which were not covered by the slimes. ML25 is typical of weathered sulfide-rich tailings, providing a base case for the evaluation of reclamation activities.

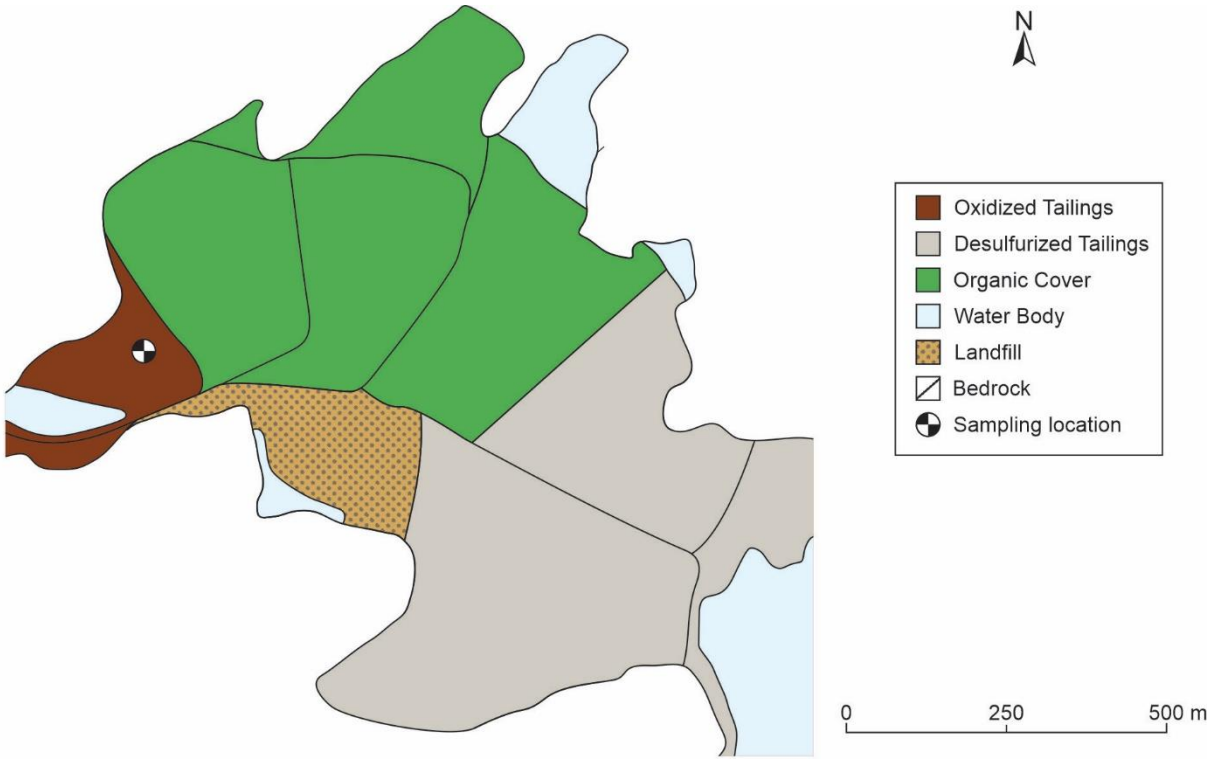

Figure 5.1: Map showing the ML25 location (oxidized tailings, not covered by the slimes) within the Strathcona tailings impoundment [modified from McAlary (2021), in preparation].

5.2.2. Geochemical analysis

Two sets of cores, one extending from the surface to a depth of 3.5 m, the other reaching a depth of 2.5 m, were sampled in August 2014 for pore-water extraction, and for the mineralogical characterization of the tailings, respectively. Core samples were collected using 7.62 cm (3 inch) ID thin wall aluminum tubing, which were vibrated into the ground by a gas powered hammer. The cores were kept frozen until analysis. Pore-water was extracted at the University of Waterloo using the immiscible displacement technique described by Moncur et al. (2013). The pH and Eh measurements were performed immediately after sampling. Due to the low pH and the limited volume of pore-water extracted from the cores, alkalinity measurements were not performed. Samples for cation, anion, and Ni isotope determination were collected using polyethylene syringes (BD, Franklin Lakes, NJ) and filtered with 0.45 µm cellulose acetate membranes. Samples for cation and Ni isotope analysis were also acidified using concentrated trace-metal grade HNO_3 (Omnitrace ultra, EMD Millipore).

The set of cores dedicated to the mineralogical characterization of the tailings was opened in an anaerobic chamber (Coy Laboratory Products Inc., Grass Lake, MI) to prevent contamination with atmospheric oxygen, and, subsequently, the tailings samples were collected in glass bottles and stored under anaerobic conditions. X-ray fluorescence (XRF) (Panalytical Ltd, MiniPal 4) and Carbon and Sulfur analysis (Eltra Ltd, CS 2000) were performed on subsamples of the tailings material.

5.2.3. X-ray Absorption Spectroscopy (XAS)

Pulverized and freeze-dried samples for S K-edge spectra collection were stored in 2 mL plastic tubes with snap-shut caps and transported to the Canadian Light Source in an anaerobic jar. Before analysis samples were spread onto double-sided carbon tape adhered to a copper sample plate. The copper sample plate was removed from the anaerobic environment directly before introduction to the sample chamber, which was subsequently placed under vacuum. The samples were analyzed at Soft X-Ray Microcharacterization Beamline (SXRMB), a bending magnet beamline with a Si(111) crystal monochromator and a toroidal focusing mirror. The beam spot size was 1 × 4 mm and 2 scans were collected for each sample. The spectra were collected over the XANES region of interest from 2452 to 2542 eV, with a step size of 1 eV in the pre-edge region, 0.15 eV in the XANES region and 0.75 eV in the background (post-edge) region, an integration time of 2 s was used in all regions. A seven-element silicon drift diode detector was used to collect partial fluorescent yield (PFY) spectra. Total electron yield (TEY) spectra were collected simultaneously. PFY and TEY spectra were compared on a per-sample basis to determine the optimal detection method for the individual sample matrix and S concentration. Standard reference spectra were collected for gypsum ($CaSO_4 \cdot H_2O$) to perform energy calibration.

Pulverized and freeze-dried samples for Ni K-edge spectra collection were packed into a 3-mm thick Teflon holder with circular openings (10 mm radius). Both ends of the Teflon holder were sealed with Kapton tape. Samples were kept in anaerobic conditions until analysis which was

performed at the Advanced Photon Source (APS), Sector 20-Bending Magnet beamline (20-BM), Argonne, USA. Spectra were collected in fluorescence mode. Multiple scans were taken for each sample to improve the signal-to-noise ratio and provide more reliable data analysis. Both S and Ni XANES data analysis was performed using the Athena software package (Ravel and Newville, 2005)

5.2.4. Preconcentration and Ni isotope analysis

Sample purification and Ni isotope analysis were conducted following the procedure presented in Parigi et al. (Chapter 2). Samples, amended with a $^{61}Ni - ^{62}Ni$ double-spike solution, were purified adopting a two-step chromatography approach: (1) Fe, Zn, and Cu were removed by using the BioRad AG MP-1M (100 – 200 mesh, chloride form) anion exchange resin; (2) Ni was separated from the remaining matrix elements using a Ni-specific resin from Eichrom Technologies. Samples were subsequently oxidized to break the Ni-DMG (dimethylglyoximes) complexes eluted from the Ni-resin step. Purified Ni fractions were evaporated and finally dissolved in 3% HNO_3 for isotope analysis.

Nickel isotope determination was performed on a Thermo Scientific Neptune MC-ICP-MS coupled with an APEXQ desolvation introduction system (ESI). Measurements were conducted on the low mass shoulders of the peaks in high resolution mode to avoid polyatomic interferences.

True Ni isotope ratios were determined using the method described by Siebert et al. (2001). Ni isotope values were expressed as $\delta^{60}Ni$ in per mill (‰) relative to the Ni international isotopic standard NIST SRM 986:

$$\delta^{60}\mathrm{Ni} = \left[\frac{(^{60}\mathrm{Ni}/^{58}\mathrm{Ni})_{\mathrm{sample}}}{(^{60}\mathrm{Ni}/^{58}\mathrm{Ni})_{\mathrm{SRM986}}} - 1\right] \mathrm{x}\, 1000 \qquad (1)$$

Results were normalized to the average value of NIST SRM 986 measured before and after each sample and having the same concentration and spike-to-standard ratio as the samples.

The long-term analytical reproducibility of the standard NIST SRM986 was determined to be ±0.05‰. When the 2SD values, calculated on three measurements/sample, were < 0.05‰ (long-term reproducibility), the value of the long-term reproducibility was used.

5.3. RESULTS

5.3.1. Unsaturated zone geochemistry

Results from the pore-water and tailings characterization are summarized in the SI (Table S5.1 and S5.2, and Fig. 5.2 and 5.3, respectively). The water table was measured in August 2014 and October 2015 from the piezometer nests installed at the ML25 location, and it showed an average value of 2.93 m bgs.

Measured pH values ranged from 3.2 to 5.2 at depths of 0.86 and 2.83 m bgs, respectively. Eh values ranged from 569 mV at the tailings surface and to 206 mV below 2.24 m bgs.

The dominant dissolved component in the pore-water samples was represented by the anion SO_4, which displayed a maximum concentration of 20936 mg L^{-1} at 0.86 m bgs. Dissolved Ni and Al concentrations reached maximum values of 579 and 2809 mg L^{-1}, respectively, at the same depth. In contrast, dissolved Fe showed a maximum concentration of 2300 mg L^{-1} at a depth of 1.88 m bgs.

The highest concentrations of Ni in the tailings correlate with the highest S peaks in the solid samples. Both Ni and S exhibited maximum concentrations of 5007 mg kg^{-1} and 5.37 wt %, respectively, at 1.78 m bgs. Carbon, although depleted across the entire depth profile, reached a maximum concentration of 0.07 wt % at 2.08 m bgs.

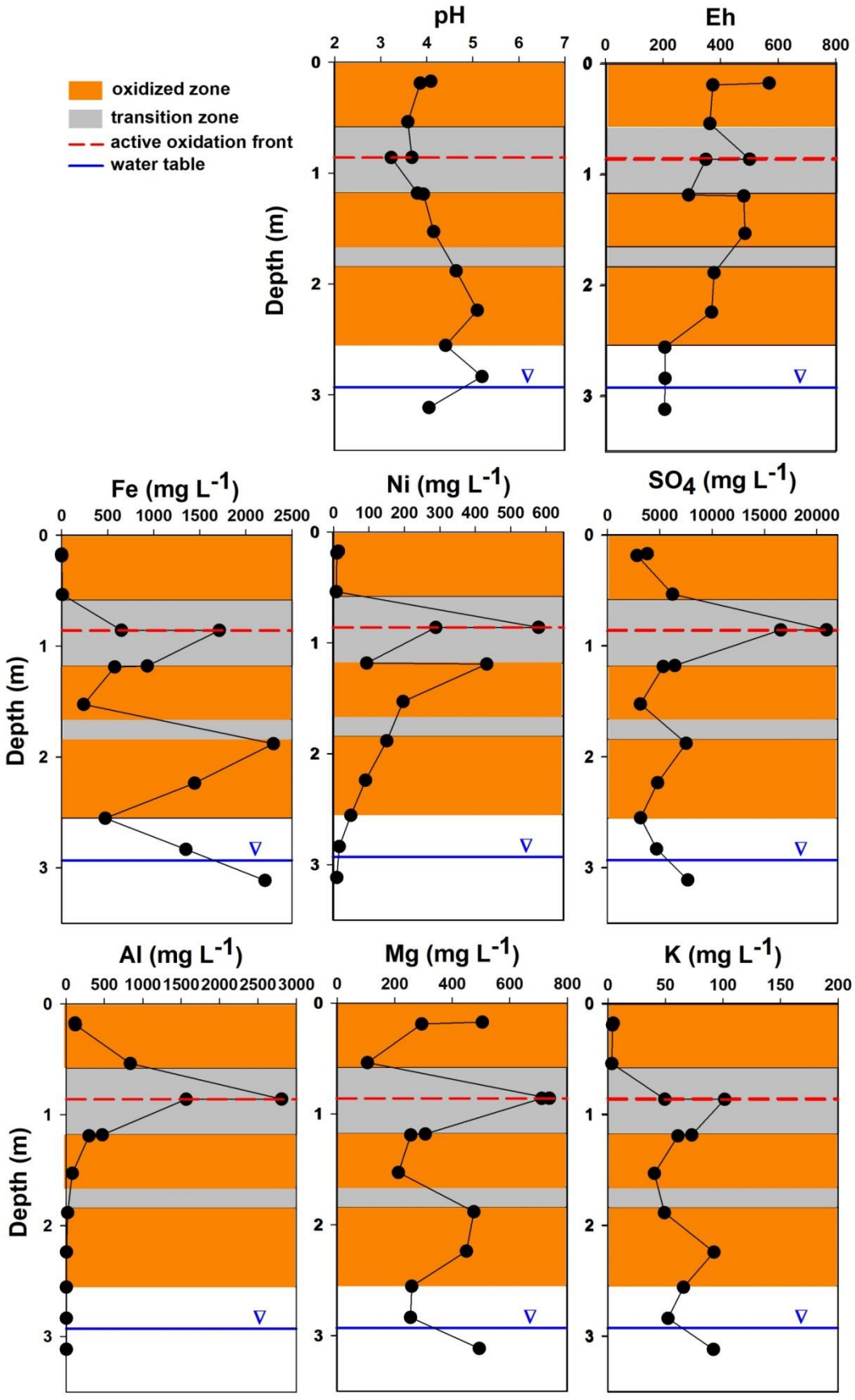

Figure 5.2: Pore-water geochemical depth profiles of pH, Eh, Fe, Ni, SO_4, Al, Mg, and K, and associated oxidation zones. The red dashed-line represents the active oxidation zone. The blue horizontal line indicates the water table.

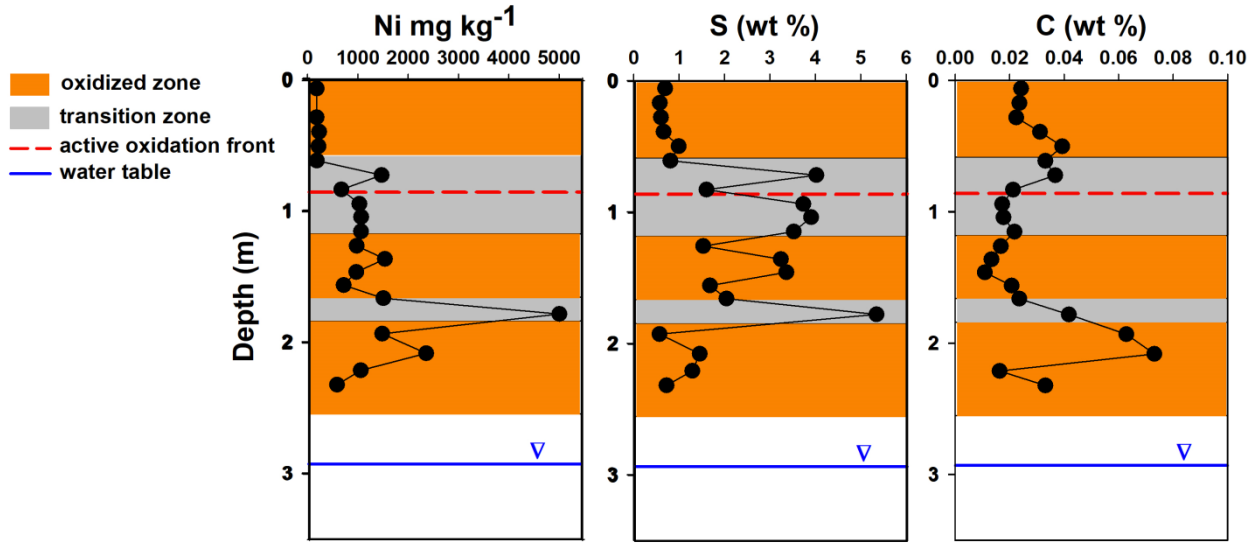

Figure 5.3: Geochemical depth profiles of Ni, S, and C from the tailings solid material and associated oxidation zones. The red dashed-line represents the active oxidation zone. The blue horizontal line indicates the water table. Detection limits: 0.005% C; 0.3% S; <2 mg kg^{-1}.

5.3.2. X-ray Absorption Spectroscopy (XAS)

Sulfur K-edge spectra measurements were performed on samples collected at different depths in the tailings profile (Fig.5.4). Linear combination fitting (LCF) was carried out to identify the main S species present in each sample. Sulfur standards used for LCF represent the principal S species encountered in similar mine tailings impoundments.

Pyrrhotite, although being depleted in the first 30 cm bgs, was the dominant species in the tailings samples, and it ranged from 38 to 72% (Table 5.1). Pyrite contribution to the sample spectra ranged from 5 to 53%, and it was mainly present at depths below 1.56 m bgs, whereas pentlandite was identified in tailings samples from between 0.94 to 1.56 m bgs (3 to 7%). Among the secondary minerals, ferrous sulfate exhibited the largest contribution to the samples (from 18 to 69%).

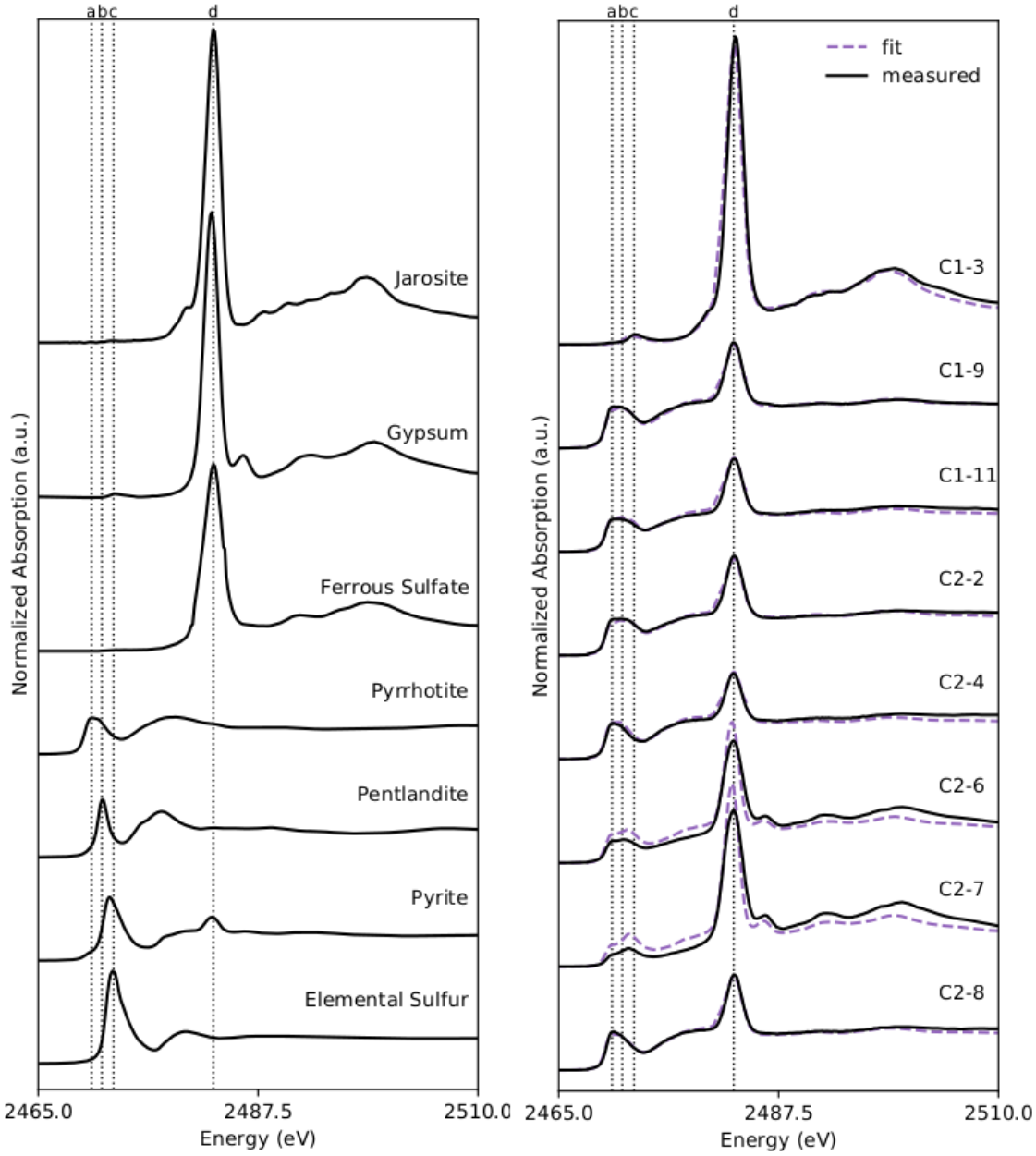

Figure 5.4: Sulfur K-edge spectra from sulfur standards (left) and tailings samples collected at different depths (right); C1-3, depth 0.28 m bgs; C1-9, depth 0.94 m bgs; C1-11, depth 1.15 m bgs; C2-2, depth 1.36 m bgs; C2-4, depth 1.56 m bgs; C2-6, depth 1.78 m bgs; C2-7, depth 1.93 m bgs; C2-8, depth 2.08 m bgs. Solid lines and dashed purple lines represent experimental and fitted spectra, respectively. Vertical dotted lines represent measured S k-edge white line maxima for (a) pyrrhotite, (b) pentlandite, (c) elemental sulfur, (d) sulfate (jarosite and/or ferrous sulfate and/or gypsum).

Table 5.1: Results of least squares linear combination fit for the S spectra. Values reported as 0.00 represent minerals that were not necessary to achieve an acceptable fit for the sample spectra, however, they may be present in the sample in low concentrations.

Sample ID	Depth (m)	Gypsum	Jarosite	Elemental S	Ferrous Sulfate	Pentlandite	Pyrite	Pyrrhotite	Sum
C1-3	0.28	0.00	0.23	0.00	0.69	0.00	0.08	0.00	1
C1-9	0.94	0.00	0.00	0.08	0.22	0.07	0.00	0.63	1
C1-11	1.15	0.00	0.00	0.09	0.23	0.05	0.00	0.62	1
C2-2	1.36	0.00	0.00	0.11	0.24	0.06	0.00	0.60	1
C2-4	1.56	0.00	0.00	0.00	0.21	0.03	0.05	0.71	1
C2-6	1.78	0.27	0.00	0.00	0.00	0.00	0.19	0.54	1
C2-7	1.93	0.39	0.00	0.00	0.00	0.00	0.23	0.38	1
C2-8	2.08	0.00	0.04	0.00	0.18	0.00	0.07	0.72	1

Nickel K-edge spectra, collected on selected samples, are plotted together with Ni standards (Fig. 5.5) to evaluate changes in Ni coordination (Ni-S to Ni-O) during sulfide minerals oxidation (Fig. 5.6). Results from LCF are shown in Table 5.2 and Fig. 5.6.

$Ni(OH)_2$, NiO, and, to a lesser extent, $NiSO_4$ are the only Ni species present in the upper 0.50 m bgs of the tailings. Although to varying degrees, the presence of $Ni(OH)_2$ and NiO, which indicates the contribution of Ni-O features to the samples, is visible in all of the samples. Among the Ni sulfides species, which characterize the whole depth profile below 0.70 m bgs, NiS_2 dominates (from ~ 25 to 60% contribution to the samples spectra; Table 5.2 and Fig. 5.6) followed by pentlandite $(Fe,Ni)_9S_8$ (from ~ 1 to 30% contribution to the samples spectra; Table 5.2 and Fig. 5.6). NiS (millerite) is only present at depth 0.83 m bgs within the tailings impoundment, showing a contribution of ~ 20% to the samples spectra.

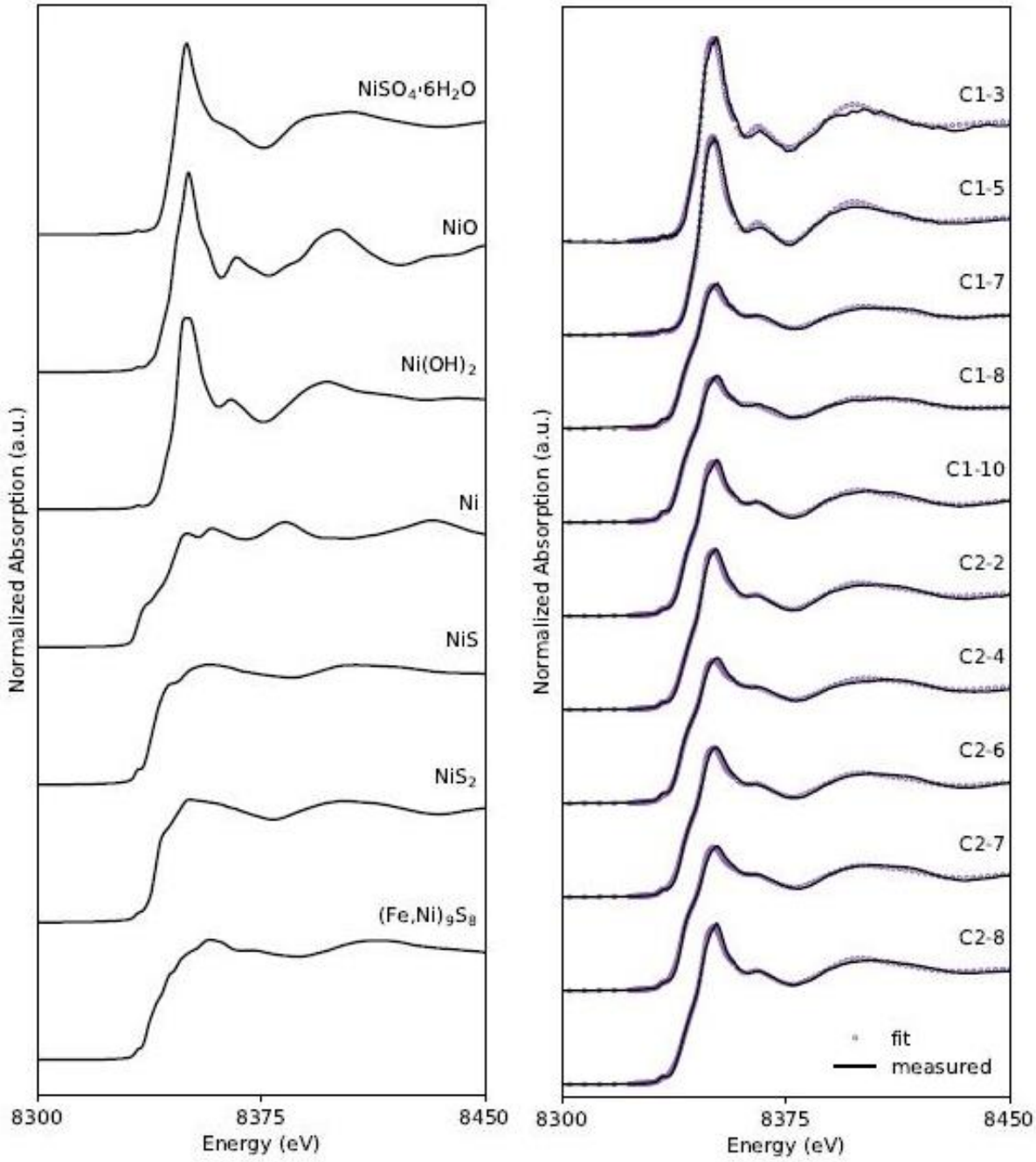

Figure 5.5: Nickel K-edge spectra from Ni standards with coordinations Ni-O and Ni-S (left) and Ni K-edge spectra from tailings samples collected at different depths (middle and right); C1-3, depth 0.28 m bgs; C1-5, depth 0.50 m bgs; C1-7, depth 0.72 m bgs; C1-8, depth 0.83 m bgs; C1-10, depth 1.04 m bgs; C2-2, depth 1.36 m bgs; C2-4, depth 1.56 m bgs; C2-6, depth 1.78 m bgs; C2-7, depth 1.93 m bgs; C2-8, depth 2.08 m bgs.

Table 5.2: Results of least squares linear combination fit for the Ni spectra.

Sample ID	Depth (m)	$(Fe,Ni)_9S_8$ [pentlandite]	NiO	$Ni(OH)_2$	NiS	NiS_2	$NiSO_4$	Sum
ML25C1-3	0.28	0.00	0.25	0.75	0.00	0.00	0.00	1
ML25C1-5	0.5	0.00	0.24	0.64	0.00	0.00	0.12	1
ML25C1-7	0.72	0.29	0.09	0.25	0.00	0.37	0.00	1
ML25C1-8	0.83	0.19	0.00	0.3	0.21	0.3	0.00	1
ML25C1-10	1.04	0.09	0.1	0.33	0.00	0.48	0.00	1
ML25C2-2	1.36	0.19	0.09	0.4	0.00	0.32	0.00	1
ML25C2-4	1.56	0.24	0.05	0.22	0.00	0.49	0.00	1
ML25C2-6	1.78	0.19	0.08	0.31	0.00	0.42	0.00	1
ML25C2-7	1.93	0.16	0.06	0.21	0.00	0.57	0.00	1
ML25C2-8	2.08	0.23	0.14	0.35	0.00	0.28	0.00	1

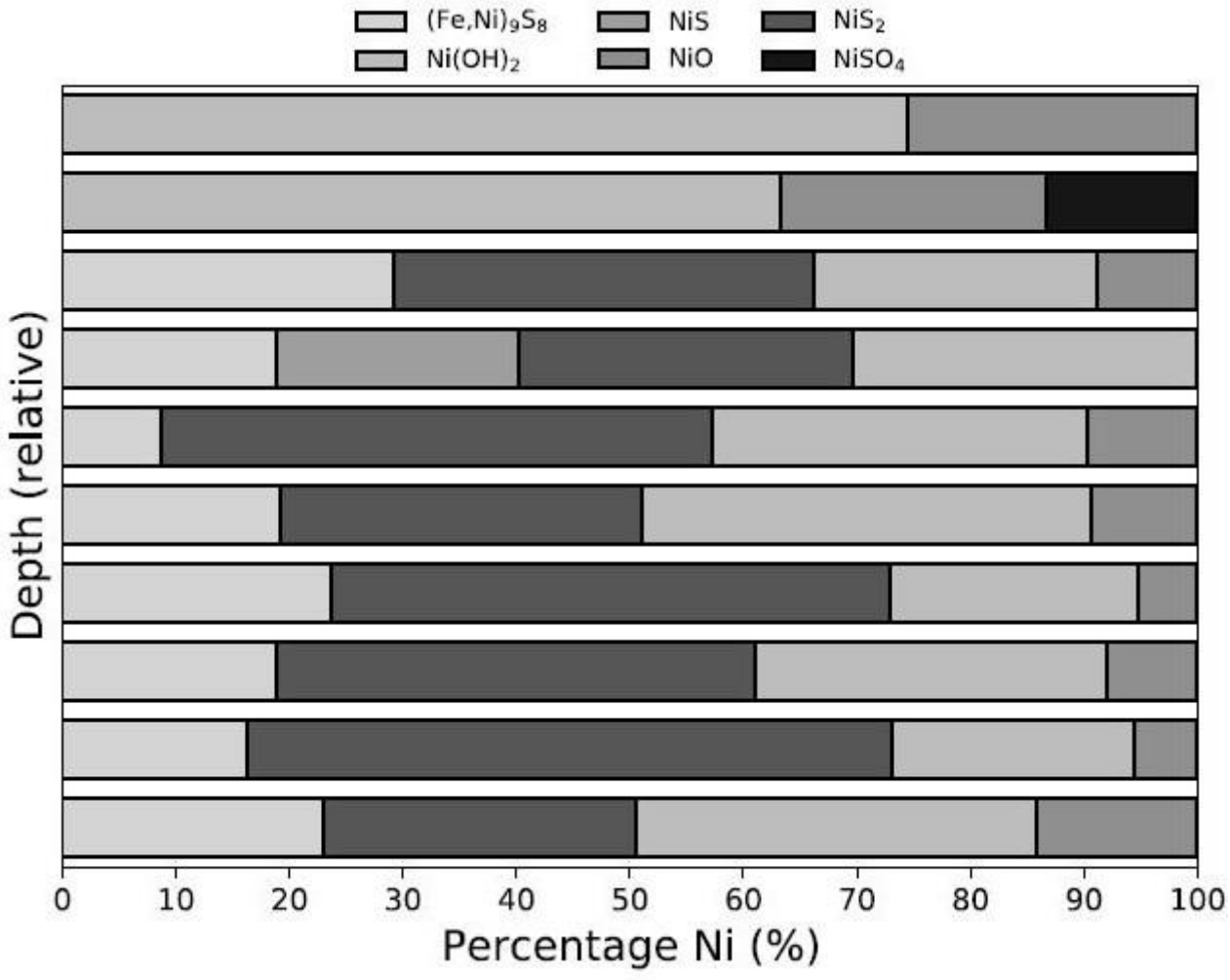

Figure 5.6: Bar chart showing the percentage of each standard used in linear combination fitting performed on Ni spectra.

5.3.3. Ni isotope fractionation

The δ^{60}Ni values ranged from -1.92 ±0.05 ‰ to 2.29 ±0.06 ‰ (Fig. 5.7). Nickel isotopic ratios showed enrichment in ^{60}Ni at the tailings surface and at depths below 2.24 m bgs, exhibiting the maximum value below the water table, at 3.11 m bgs. In contrast, negative δ^{60}Ni values characterized the tailings at depths between 0.54 and 2.24 m bgs, reaching the lowest Ni isotope ratio at 1.53 m bgs.

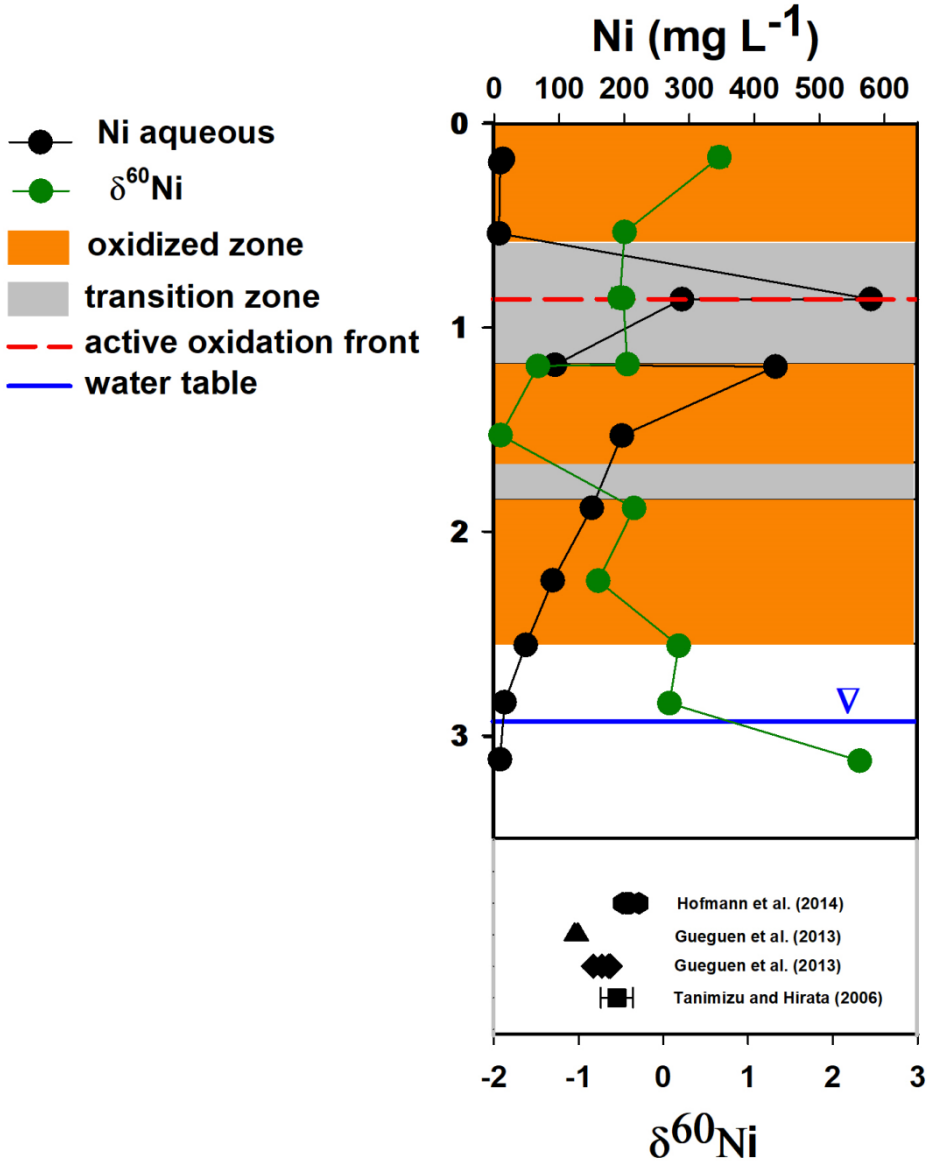

Figure 5.7: δ^{60}Ni depth profile and associated oxidation zones. The error bars represent 2σ from three analytical events. The red dashed-line represents the active oxidation zone. The blue horizontal line indicates the water table. Hexagons: δ^{60}Ni values relative to pyrrhotite–pentlandite ore from Zimbabwe (Hofmann et al., 2014); triangles: δ^{60}Ni values relative to Ni-sulfide ores from the Alexo mine, Abitibi, Canada (Gueguen et al., 2013); diamonds: δ^{60}Ni values relative Ni-sulfide ores from Western Australia (Gueguen et al., 2013); square: δ^{60}Ni value relative to a pentlandite sample from the Strathcona mine, Sudbury, Canada (Tanimizu and Hirata, 2006).

DISCUSSION

5.3.4. Sulfide oxidation depth profiles

Results from pore-water analysis and characterization of the tailings solid material indicate the presence of paleo-oxidation zones, intercalated with a paleo-transition layer, which underlie the recent oxidation and transition zones (Fig. 5.2 and 5.3). Similar paleo-surfaces, which were also found in the course of investigations conducted on other tailings impoundments (Blowes and Jambor, 1990; Gunsinger et al., 2006a), suggest that long periods of time, during which extensive sulfide oxidation could develop in the impoundment, occurred in between depositions of fresh tailings. Although unaltered zones, represented by negligible sulfide oxidation, are often present at depth, mineralogical analysis indicates the entire 2.5 m of the investigated ML25 tailings was affected by alteration reactions. The tailings from the ML25 storage location are coarse grained and fairly dry, therefore more susceptible to oxidation. Blowes and Jambor (1990) reported that transition/intermediate zones, characterized by moderate to weak alteration, are thicker in coarse-grained tailings with deep water table due to a higher O_2 diffusivity.

The upper 0.58 m of the core was affected by strong oxidation and exhibited near obliteration of all sulfide minerals (Fig. 5.3). This zone was characterized by a rusty-red color and the presence of discontinuous layers of jarosite ($KFe_3(SO_4)_2(OH)_6$; Table 5.1) and ferric oxyhydroxide, common secondary minerals observed in oxidized tailings, which likely represent primitive stages of hardpan development (Blowes and Jambor, 1990; Blowes et al., 1991). LCF conducted on S XANES also indicate a high contribution of Fe(II) sulfate to the S spectra in the upper 0.28 m of the oxidized zone (Table 5.1). The Fe(II) sulfate, usually melanterite [$FeSO_4 \bullet 7(H_2O)$], can either form highly soluble precipitates on the sun-baked surface of the tailings (Blowes and Jambor, 1990) or constitute blackish Fe(II) hardpan layers (Moncur et al., 2005). The widespread presence of Fe(II) sulfate in ML25 tailings samples (Table 5.1) suggests most of the Fe in the pore-water was present as Fe(II). Similar findings

have been explained by the presence in the tailings of high sulfide contents which promote the consumption of O_2 and the reduction of Fe(III) to Fe(II) (Blowes et al, 1991; Moncur et al., 2005). LCF results associated with the Ni spectra show Ni species present in the upper 0.58 m of the tailings are characterized by 100% Ni-O coordination environment (Table 5.2 and Fig. 5.6) due to the high sulfide oxidation rate of this layer. Although the presence of discrete secondary Ni minerals have not been detected in tailings impoundments (Blowes and Jambor, 1990; Alpers et al., 1994; Johnson et al., 2000), $Ni(OH)_2$, NiO and $NiSO_4$ phases were used as standards in LCF analysis for the following reasons: EXAFS analyses conducted on sorption of Ni onto calcareous aridisol soil (Qiang et al., 2017) and hydrous ferric oxide (Xu et al., 2007) showed the structure of sorbed Ni was comparable to that of $Ni(OH)_{2(s)}$. Xu et al. (2007) also indicated similar interatomic Ni-O and Ni-Ni distances between Ni coprecipitated with hydrous ferric oxide and $Ni(OH)_{2(s)}$. Langman et al. (2015) demonstrated that during pyrrhotite weathering, Ni-S changed to Ni-O coordination to form NiO and/or $NiSO_4$ species.

A transition zone, which extends to a depth of 1.19 m bgs, was identified below the superficial oxidized layer. A front of active oxidation (red dashed line in Fig.5.2) developed in this zone and was characterized by elevated concentrations of dissolved constituents, in particular SO_4, Fe, Ni, and Al, and by low pH (3.2, the lowest value measured at ML25). The dissolution of aluminosilicate and/or Al hydroxide, which leads to the release of high Al concentrations, could cause the rise in pH (from 3.2 to 3.9) at the boundary between the transition and the paleo-oxidized zones (1.19 m bgs). This boundary is also characterized by an abrupt rise in Eh. S and Ni XANES associated with this transition layer show an increased contribution of Ni-bearing sulfides (pentlandite, pyrrhotite, NiS, and NiS_2; Tables 5.1 and 5.2, and Fig. 5.5 and 5.6) to the sample spectra. As millerite (NiS) is only present at a depth of 0.83 m bgs within the profile investigated, it is reasonable to assume NiS reprecipitated from solution during sulfide mineral oxidation and dissolution processes characterizing the transition layer. In the Sudbury ore deposits millerite is found in minor amounts compared to pyrrhotite, pentlandite, and pyrite

and usually concentrated locally in mineralized veins (Naldrett, 1984). Furthermore, the precipitation of secondary sulfides is common within weathered sulfide deposits where metals are leached and transported to zones of more reducing conditions (Alpers et al., 1994).

It must be noted that the spectra of NiS_2 does not indicate the presence of vaesite within the impoundment, as vaseite is generally a minor phase of the Sudbury sulfide ore. The NiS_2 spectra more likely represents the fraction of Ni associated with FeS_2 polymorphs, pyrite and marcasite. As vaesite is characterized by the pyrite-type structure (Tossell et al., 1981), Ni XANES of NiS_2 and pyrite are similar. Furtermore, Swanner et al., 2019 reported similarities between Fe XANES belonging to pyrite and marcasite. Nickeliferous pyrite and nickeliferous marcasite have been documented in tailings impoundments from the Sudbury area (Johnson et al., 2000) and their presence is indicator of sulfide mineral oxidation: pyrite is characterized by a high resistance to sulfide oxidation among sulfides (Moncur et al., 2009), whereas marcasite is commonly found as a secondary mineral during early stages of pyrrhotite oxidation (Blowes and Jambor, 1990; Moncur et al., 2009).

The paleo-oxidized zone extends from 1.19 to 1.66 m bgs and it was represented by a decrease in the concentrations of the major dissolved constituents.

A paleo-transition zone was identified between 1.66 m and 1.84 m bgs. This intermediate layer was dominated by the highest concentrations of Ni and S in the tailings (Fig.5.3). The lower oxidation rate could be linked to the finer grain texture of the tailings in this depth interval (Fig. S5.1).

A deeper paleo-oxidized layer, identified from the mineralogical study, was located between 1.84 m and 2.55 m bgs. This zone was characterized by the highest concentration of dissolved Fe (2300 mg L^{-1}), and by an increase in other dissolved constituents (SO_4, Mg, and K). The release of these dissolved elements could be generated by the dissolution of secondary Fe minerals, such as jarosite, Fe(III) oxyhydroxides, and Fe(II)sulfate, which may no longer be stable due to changes in chemical conditions. The highest dissolved Fe concentration in pore-

water is correlated with the absence of Fe(II) sulfate minerals in the tailings, which characterizes S XANES only at this depth interval, thus supporting this hypothesis. Similar Fe trends with depth have been reported by other researchers (Moncur et al., 2005; Gunsinger et al., 2006a; Lindsay et al., 2009).

The rise in pH (5.1) registered at 2.24 m bgs coincides with an increase in the abundance of C content of the tailings which occurs at around 2 m bgs.

Immediately below the deeper paleo-oxidized zone, Eh decreased sharply to more reducing values (206 mV). At 3 m bgs pore-water physical and chemical characteristics were influenced by fluctuations in the water table.

5.3.5. Nickel isotopes as environmental tracers

Oxidation reactions involving Ni-bearing pyrrhotite and pentlandite are the primary source for high concentrations of Ni in the tailings pore-water. The isotopic composition of a sample of pentlandite from the Strathcona Mine, in Sudbury, was characterized by Tanimizu and Hirata (2006), and exhibited a δ^{60}Ni of −0.54 ± 0.19‰. Gueguen et al. (2013) measured the Ni isotope composition of Ni-sulfide ores which resulted in a wide range of Ni isotope values (from −0.10 to −1.03‰). Samples from the Abitibi region (western Québec, Canada), characterized by elevated content of pentlandite, displayed the most negative Ni isotopic signatures (from −0.62 to −1.03‰). Ni isotope analysis of pyrrhotite–pentlandite ore in Zimbabwe yielded δ^{60}Ni values as low as −0.47‰ (Hofmann et al., 2014).

Ni isotope results of the pore-water extracted from the ML25 core and the Ni isotopic signatures of the above mentioned samples of Ni-bearing sulfides are visible in Fig. 5.7.

The δ^{60}Ni measured at the top of the recent oxidized zone (0.17 m bgs) exhibited a positive value of 0.66 ± 0.09‰. Ni concentrations and mobility within the shallower zone of the tailings impoundment are affected by rainfall and snowmelt, which also influence Ni isotopic signatures at these depths. Weathering processes are known to enrich dissolved Ni in heavier

isotopes (Cameron and Vance, 2014; Ratié et al., 2015, 2016, and 2018; Spivak-Birndorf et al., 2018). Cameron and Vance (2014) reported an average δ^{60}Ni value for rivers of 0.8‰.

The positive δ^{60}Ni characterizing the shallower part of the contemporary oxidized layer, which coincides with low concentrations of dissolved Ni, could also be explained by Ni adsorption to and/or coprecipitation with the secondary Fe oxyhydroxide minerals which are commonly found in strongly oxidized zones. Experiments conducted on Ni adsorption to and coprecipitation with ferrihydrite and goethite, and transformation of ferrihydrite to hematite, resulted in an increase in the relative abundance of heavier Ni isotopes in solution (Wasylenki et al., 2015; Wang and Wasylenki, 2017; Gueguen et al., 2018). Nickel XANES spectra for samples collected at depths of 0.28 and 0.50 m, (C1-3 and C1-5 respectively), are characterized by the sole presence of Ni-O coordination features (Fig.5.6 and S5.2), consistently with the high degree of oxidation characteristic of this layer. As the presence of Ni secondary minerals in mine tailings affected by sulfide oxidation has not been detected in previous studies, decreases in Ni concentration in pore-water samples have been attributed to adsorption to and/or coprecipitation of Ni with secondary Fe(III) oxyhydroxide minerals (Blowes and Jambor, 1990; Alpers et al., 1994; Johnson et al., 2000). Ni hydroxide spectra shows similarities with the spectra of Ni sorbed to and/or coprecipitated with hydrous ferric oxide, as mentioned in the previous section,

At the boundary between the oxidized and the transition zones (0.54 m bgs) dissolved Ni concentrations increased sharply, whereas δ^{60}Ni decreased to −0.46‰ ± 0.05‰. Similar δ^{60}Ni values (ranging from −0.51‰ to −0.42‰) were observed across the entire transition layer. These values falls within the range of the δ^{60}Ni associated with Ni sulfides rich in pentlandite, and, together with high dissolved Ni concentrations, could be the result of the oxidative dissolution of these Ni-bearing minerals due to the advance of the oxidation front. Ni XANES spectra of the samples located in this transition zone are less affected by replacement of Ni-S with Ni-O than the spectra collected from the oxidized zone (Fig. 5.6). Transition zones,

distinct from oxidized layers, are characterized by various degrees of sulfide-mineral oxidation (moderate to weak alteration), and do not show the complete obliteration of sulfide minerals (Blowes and Jambor, 1990; McGregor et al., 1998; Moncur et al., 2005).

Changes in redox conditions in the upper part of the paleo-oxidized layer (1.19 m bgs) seem to be correlated with an increase in Ni concentration in the pore-water at the same depth (Fig. 5.2). The pore-water sample exhibiting this peak in concentration (433 mg L^{-1}), which is not present in the depth profiles of the other major pore-water constituents, and the sample immediately after (1.53 m bgs), were characterized by low δ^{60}Ni of −1.48‰ and −1.92‰, respectively. These Ni isotopic signatures, which were more negative than δ^{60}Ni values associated with Ni-bearing sulfides, could be the result of the release of Ni adsorbed onto or coprecipitated with Fe oxyhydroxides, Al, and possibly Mn hydroxide minerals, caused by changes in chemical conditions in the paleo-oxidized zone. Although Ni isotope fractionation during Ni adsorption to Al and Mn hydroxides has not yet been investigated, research conducted on Ni adsorption onto Fe oxyhydroxide and Mn oxide minerals has reported the preferential retention of lighter Ni isotopes by the solid phase (Wasylenki et al., 2015; Wang and Wasylenki, 2017; Gueguen et al., 2018; Sorensen et al., 2020). Ni adsorption onto birnessite [$(Mn^{4+},Mn^{3+})_2O_4 \bullet \cdot 1.5\ H_2O$] resulted in fractionation factors $\Delta^{60}Ni_{min\text{-}aq}$ ranging from −2.76‰ to −3.35‰ (Sorensen et al., 2020). The presence of secondary Fe(III) oxyhydroxide minerals is confirmed by the rusty red colour of the tailings sampled at this paleo-oxidized layer depths (Fig. S5.3). Furthermore, S XANES spectra at these same depths are characterized by the presence of elemental S and Fe(II) sulfate, common secondary products of sulfide-mineral oxidation reactions.

The pore-water sample located at the boundary between the paleo-transition layer and the deeper paleo-oxidized zone (1.84 m bgs) displayed a δ^{60}Ni value of −0.34‰. This Ni isotope value, as it seems to align to the trend of the samples collected from the recent transition zone, could be related to oxidative dissolution of Ni-bearing sulfides. Ni XANES spectra of samples

from the paleo-transition layer also show similar replacement of Ni-S with Ni-O to the spectra of the recent transition zone samples (samples C1-8 and C2-6; Fig. 5.6 and S5.2). The low δ^{60}Ni value of −0.77‰ characterizing the pore-water found in the middle of the deeper paleo-oxidized zone (2.24 m bgs), corresponding to declining concentrations of dissolved Ni, could be associated with the partial desorption of Ni bound to Fe(III) oxyhydroxyde minerals; similarly for the samples located in the upper paleo-oxidized zone. The Ni spectra show comparable degrees of oxidation (Fig. 5.6 and S5.2) relative to the upper and lower paleo-oxidized layers (samples C2-2 and C2-8, respectively).

Ni isotope fractionation measurements performed on the two samples situated below the deeper paleo-oxidized layer (at 2.55 and 2.83 m bgs) resulted in δ^{60}Ni of 0.18‰ and 0.1‰, respectively. These positive isotopic values together with the decrease of Ni in the pore-water could be the result of Ni removal from solution by adsorption and/or coprecipitation processes. The pore-water sample collected from the saturated zone, at 3.11 m bgs, exhibited a δ^{60}Ni of 2.29‰. Very similar heavy Ni isotope values of 2.27 ± 0.08‰ and 2.20 ± 0.09‰ were found in groundwater samples from the Barro Alto Ni deposit, in Brazil, and were considered the result of consecutive weathering processes involving the overlying layers (Ratié et al., 2018).

5.4. SUMMARY OF RESEARCH RESULTS

Mobility of Ni was investigated using Ni stable isotope analysis performed on pore-water samples collected at different depths within the Strathcona tailings impoundment, at location ML25. Ni isotopic signatures of water samples coupled with solid tailings analyses resulted in the identification of consecutive zones affected by different degrees of alteration. Beneath a shallow, strongly oxidized layer, a front of active sulfide-mineral oxidation characterized a recent transition zone. Presence of paleo-oxidized and paleo-transition layers, related to multiple tailings discharge events, were found below the transition zone. Layers of unaltered waste material were not found, possibly due to the coarse grained texture of the tailings which makes them more susceptible to oxidation. Results from this study show Ni isotope

measurements as good indicators of the processes affecting Ni release and fate in mine environments.

CHAPTER 6

Conclusions

6.1. SUMMARY OF RESEARCH

Due to analytical and methodological advances, “non-traditional” stable isotope analysis has been successfully applied to the investigation of the source and fate of trace metals in the environment.

Despite the recent interest in Ni stable isotope analysis, Ni stable isotope systematics is still at an early stage of development. Further research, which focuses on the characterization of Ni isotopic fingerprints associated with important biogeochemical processes controlling Ni mobility, is needed before Ni isotopes can be applied as environmental tracers. In this respect, the present thesis first aimed to identify Ni isotopic signatures associated with Ni attenuation processes, which were not previously studied, and subsequently involved the application of Ni stable isotope analysis to elucidate the processes influencing Ni release and attenuation at a mine site affected by extensive sulfide mineral oxidation.

Batch experiments were performed to evaluate Ni isotope fractionation during precipitation of secondary mineral phases (i.e., Ni hydroxide, Ni hydroxycarbonate and Ni sulfide) which are involved in Ni attenuation from the environment. All three systems were characterized by a preferential retention of lighter Ni isotopes by the solid phase and showed fractionation factors ε of −0.40‰, −0.50‰ and −0.73‰ relative to the hydroxide, carbonate and sulfide systems, respectively. The preferential partition of lighter isotopes into the solid phase was associated with distortions of the Ni-O octahedra in the Ni hydroxide and Ni hydroxycarbonate systems, whereas transitions from Ni-O to Ni-S coordination environment in solution were connected with the fractionation measured in the Ni sulfide system.

Due to the important role played by sulfate-reducing bacteria (SRB) in the attenuation of metals in impacted groundwater, Ni isotope fractionation associated with precipitation of Ni-sulfides in the presence of *Desulfovibrio desulfuricans* ^{T} (DSM-642) was investigated. Results appeared to follow closed-system equilibrium isotope fractionation, showing a fractionation factor of $\Delta^{60}Ni_{solid\text{-}aq} = -1.99‰$. Due to the complexity of the SRB system, multiple processes, including sulfide precipitation, adsorption, complexation, and substitution, were associated with the measured Ni isotope ratios.

A flow-through cell (FTC) experiment was implemented to study the interaction between synthetic Ni-contaminated groundwater and natural crushed calcite mineral under saturated flow conditions. Results from Ni isotope analysis coupled with EXAFS modeling indicated multiple processes were involved in Ni attenuation. After a first stage dominated by Ni adsorption to and coprecipitation with calcite, which yielded a fractionation factor of $\varepsilon = -0.5‰$, Ni removal from solution as a Ni hydroxide phase characterized the second stage of the experiment, resulting in a fractionation factor of $\varepsilon = -0.4\%$.

Release and attenuation of Ni was investigated in an unreclaimed portion of a mine tailings impoundment affected by strong sulfide-mineral oxidation. Ni stable isotope analysis conducted on pore-water samples integrated with synchrotron-based studies and traditional geochemical and mineralogical techniques of solid tailings material resulted in the characterization of tailings depth profiles up to 3.5 m bgs. Layers showing varying degrees of recent, and paleo-sulfide-mineral oxidation, which were connected with multiple tailings deposition phases, were identified in the investigated area. Results from Ni stable isotope analysis of the pore-water samples related well with the weathering profiles of the tailings impoundment, thus showing the potential of Ni stable isotopes as tracers in field settings.

6.2. SCIENTIFIC CONTRIBUTIONS AND FUTURE DIRECTIONS

Although the recent attention gained by Ni stable isotope analysis, Ni stable isotope systematics is just starting to develop, thus new research is needed for its further characterization. Current research on Ni isotope fractionation has focused on a variety of applications, including investigations on the Ni global mass balance, which involved studies on the input and output fluxes of Ni to and from the ocean, the delineation of the roles played by microbial activity and different types of vegetation on Ni isotopic signatures, and the measurements of Ni stable isotopes during adsorption to and coprecipitation with minerals implicated in the Ni global cycle (Fe oxyhydroxides, Mn oxides, and calcite). Studies have also been conducted on the identification of Ni isotopic signatures of different type of rocks, with few applications of Ni stable isotope analysis to field settings. Research on fractionation related to Ni attenuation processes, both at the laboratory scale and in the field, is lacking.

The present thesis contributed to fill some of the gaps associated with Ni stable isotope research conducted so far. The first two manuscripts offered the very first attempt to constrain Ni isotope fractionation during the precipitation of Ni secondary minerals under ambient conditions and in abiotic systems, and during interactions with SRB, bacteria used in passive treatment remediation techniques, respectively. The third manuscript (FTC system) allowed the investigation of Ni isotope behaviour associated with removal mechnisms under saturated flow conditions which are characteristic of field systems, whereas the fourth manuscript involved the use of Ni stable isotope analysis to characterize the processes controlling the source and the fate of Ni in mine waste systems, which have not been previously investigated.

Since the extent of Ni stable isotope fractionation could be influenced by changes in experimental conditions, future research steps will focus on the evaluation of the role played by other variables, including pH, temperature, solution concentrations, and the presence of Ni-competing elements in the system (i.e. Fe, and Al) on measured Ni isotope ratios.

References

Alpers, C.N., Blowes, D.W., Nordstrom, D.K., Jambor, J.L., 1994. Secondary minerals and acid minewater chemistry. In: Jambor, J.L.; Blowes, D.W. eds. Short course handbook on environmental geochemistry of sulfide mine-wastes. Mineral. Assoc. Can., 247-270.

Andersson, M.P., Sakuma, H., Stipp, S. L.S., 2014 Strontium, nickel, cadmium, and lead substitution into calcite, studied by density functional theory. Langmuir 30, 6129−6133.

Baeyens, B., Bradbury, M.H., Hummel, W., 2003. Determination of aqueous Nickel – carbonate and Nickel – oxalate complexation constants. J. Solution Chem. 32, 319–339.

Bain, J.G., Blowes, D.W., Robertson, W.D., 1998. 1996-1997 Groundwater quality – Strathcona (Moose Lake) tailings area. Report prepared for Falconbridge Ltd., Department of Earth Sciences, University of Waterloo.

Bain, J.G., Blowes, D.W., 2013. 2012 Water chemistry at the Strathcona tailings treatment system. Report Prepared for Xstrata Nickel, Department of Earth Sciences, University of Waterloo.

Balayevaa, O.O, Azizova, A.A, Muradovb, M.B, Maharramova, A.M., Eyvazovab, G.M., Alosmanova, R.M., Mamiyevc, Z.Q., Aghamaliyev, Z.A., 2016. β-NiS and Ni_3S_4 nanostructures: Fabrication and characterization. Mater. Res. Bull. 75, 155-161.

Ball, J.W., Nordstrom, D.K., 1991. WATEQ4F—User's manual with revised thermodynamic data base and test cases for calculating speciation of major, trace and redox elements in natural waters. U.S. Geological Survey Open-File Report 90–129, 185 p.

Ballesteros, F.C., Salcedo, A.F.S., Vilando, A.C., Huang, Y-H., Lu, M-C., 2016. Removal of nickel by homogeneous granulation in a fluidized-bed reactor. Chemosphere 164, 59-67.

Barim, G., Smock, S. R., Antunez, P. D., Glaser, D., Brutchey, R. L., 2018. Phase control in the colloidal synthesis of well-defined nickel sulfide nanocrystals. Nanoscale 10, 16298-16306.

Belova, D. A., Lakshtanov, L. Z., Carneiro, J. F., Stipp, S. L. S., 2014. Nickel adsorption on chalk and calcite. J. Contam. Hydrol. 170, 1–9.

Benner, S. G., Blowes, D. W., Ptacek, C. J., 1997. A full-scale porous reactive wall for prevention of acid mine drainage. Ground Water Monit. R. 17 (4), 99–107.

Benner, S.G., Blowes, D.W., Gould, W.D., Herbert, R.B., Ptacek, C.J., Herbert, R., 1999. Geochemistry of a permeable reactive barrier for metals and acid mine drainage. Environ. Sci. Technol. 33 (16), 2793–2799.

Benner, S.G., Blowes, D.W., Ptacek, C.J., Mayer, K.U., 2002. Rates of sulfate reduction and metal sulfide precipitation in a permeable reactive barrier. Appl. Geochem. 17 (3), 301–320.

Bhojane, P., Sinha, L., Goutam, U.K., Shirage, P.M., 2019. A 3D mesoporous flowers of nickel carbonate hydroxide hydrate for high-performance electrochemical energy storage application. Electrochim. Acta 269, 112-119.

Blowes, D.W., 1997. The environmental effects of mine wastes. In: Gubins, A.G. (Ed.), Proc. Exploration ‘97, 4th Decennial Internat. Conf. Mineral Exploration. Prospectors and Developers Association of Canada, Toronto, ON, pp. 887–892.

Blowes, D.W. and Jambor, J.L., 1990. The pore-water geochemistry and the mineralogy of the vadose zone of sulfide tailings, Waite Amulet, Quebec, Canada. Appl. Geochem. 5, 327-346.

Blowes, D.W., Reardon, E.J., Jambor, J.L., Cherry, J.A., 1991. The formation and potential importance of cemented layers in inactive sulfide mine tailings. Geochim. Cosmochim. Acta 55, 965-978.

Blowes, D.W., Ptacek, C.J., Benner, S.G., McRae, C.W.T., Bennett, T.A., Puls R.W., 2000. Treatment of inorganic contaminants using permeable reactive barriers. J. Contam. Hydrol. 45, 123–137.

Blowes, D.W., Ptacek, C.J., Jambor, J.L., Weisener, C.G., Paktunc, D., Gould, W.D., Johnson, D.B., 2014. The geochemistry of acid mine drainage. In: Holland, H.D., Turekian, K.K. (Eds.), Treatise on Geochemistry, Second edition Elsevier, Oxford, pp. 131–190.

Bullen, T.D., 2014. Metal stable isotopes in weathering and hydrology. In: Holland, H.D., Turekian, K.K. (Eds.), Treatise on Geochemistry, Second edition Elsevier, Oxford, pp. 329–359.

Butler, I.B., Archer, C., Vance, D., Oldroyd, A., Rickard D., 2005. Fe isotope fractionation on FeS formation in ambient aqueous solution. Earth Planet. Sci. Lett. 236, 430−442.

Cameron, V., Vance, D., Archer, C., House, C.H., 2009. A biomarker based on the stable isotopes of nickel. Proc. Natl. Acad. Sci. 106, 10944–10948.

Cameron, V., Vance, D., 2014. Heavy nickel isotope compositions in rivers and the oceans. Geochim. Cosmochim. Acta 128 (0), 195–211.

Casas-Cabanas, M., Palacín, M.R., Rodríguez-Carvajala, J., 2005. Microstructural analysis of nickel hydroxide: Anisotropic size versus stacking faults. Powder Diffr. 20 (4), 334-344.

Castillo, J., Perez-Lopez, R., Caraballo, M.A., Nieto, J.M., Martins, M., Costa, M.C., Olias, M., Ceron, J.C., Tucoulou, R., 2012. Biologically-induced precipitation of sphalerite-wurtzite nanoparticles by sulfate-reducing bacteria: Implications for acid mine drainage treatment. Sci. Total Environ. 423, 176–184.

Castillo Alvarez, M.C., 2019. Nickel isotope fractionation during adsorption on the calcite surface and coprecipitation with calcite. Ph.D. Dissertation. Université Toulouse 3 - Paul Sabatier, Toulouse, France.

Castillo Alvarez, C., Quitte´, G., Schott, J., Oelkers, E.H., 2020. Experimental determination of Ni isotope fractionation during Ni adsorption from an aqueous fluid onto calcite surfaces. Geochim. Cosmochim. Acta 273, 26–36.

Chirwa E.M.N., 2012. Bioremediation of uranium, transuranic waste and fission products. In Microbial Biotechnology: Energy and Environment. Arora, R; CABI pp.416.

Ciscato, E.R., Bontognali, T.R.R.,Vance, D., 2018. Nickel and its isotopes in organic-rich sediments: Implications for oceanic budgets and a potential record of ancient seawater. Earth Planet. Sci. Lett. 494, 239-250.

Coggans, C.J., Blowes, D.W., Robertson, W.D., Jambor, J.L.,1999. The hydrogeochemistry of a nickel-mine tailings impoundment – Copper Cliff, Ontario. In: Filipek, L.H., Plumlee, G.S. (Eds.), The Environmental Geochemistry of Mineral Deposits, Part B: Case Studies and Research Topics, Rev. Econ. Geol., 6B, pp. 447–465.

Comans, R.N.J., Middelburg, J.J., 1987. Sorption of trace metals on calcite: Applicability of the surface precipitation model. Geochim. Cosmochim. Acta 51(9), 2587–2591.

Costodes, V.C., Lewis, A.E., 2006. Reactive crystallisation of nickel-hydroxycarbonate in a fluidised bed reactor: 1. Fines production and column design. Chem. Eng. Sc. 61, 1377 - 1385.

Coudun, C., Grillon, F., Hochepied, J-F., 2006. Surfactant effects on pH-controlled synthesis of nickel hydroxides. Colloids Surf., A 280, 23–31.

Davis, J.A., Fuller, C.C., Cook, A.D., 1987. A model for trace metal sorption processes at the calcite surface: Adsorption of Cd2+ and subsequent solid solution formation. Geochim. Cosmochim. Acta 51 (6), 1477–1490.

Das, K.K., Reddy, R.C., Bagoji, I.B., Das, S., Bagali, S., Mullur, L., Khodnapur, J.P., Biradar M.S., 2019. Primary concept of nickel toxicity – an overview. J. Basic Clin. Physiol. Pharmacol. 30 (2), 141-152.

Delmas, C., Tessier, C., 1997. Stacking faults in the structure of nickel hydroxide: A rationale of its high electrochemical activity. J. Mater. Chem. 7, 1439–1443.

Defontaine, G., Michot, L.J., Bihannic, I., Ghanbaja, J., Briois, V., 2003. Synthesis of NiGa Layered Double Hydroxides. A combined extended X-ray absorption fine structure, small-angle X-ray scattering, and transmission electron microscopy study. 1. Hydrolysis in the pure Ni^{2+} system. Langmuir 19, 10588-10600.

Denkhaus, E., Salnikow, K., 2002. Nickel essentiality, toxicity, and carcinogenicity. Crit. Rev. Oncol. Hematol. 42(1), 35–56.

EcoMetrix, 2014. Field investigation of a tailings cover at the Strathcona impoundment, Report Submitted to Sudbury Integrated Nickel Operations A Glencore Company, July 2014.

Elliott, T., Steele, R.C., 2017. The isotope geochemistry of Ni. Rev. Mineral. Geochem. 82, 511–542.

Estrade, N., Cloquet, C., Echevarria, G., Sterckeman, T., Deng, T., Tang, Y., Morel J.L., 2015. Weathering and vegetation controls on nickel isotope fractionation in surface ultramafic environments (Albania). Earth Planet. Sci. Lett. 423, 24–35.

Faure, C., Delmas, C., Fouassier, M., 1991. Characterization of a turbostratic α-nickel hydroxide quantitatively obtained from an $NiSO_4$ solution. J. Power Sources. 35, 279–290.

Ferris, F.G., Fyfe, W.S., Beveridge, T.J., 1987. Bacterial as nucleation sites for authigenic minerals in a metal-contaminated lake sediment. Chem Geol. 63, 225–232.

Fiore, S., Dumontet, S., Huertas, J., Pasquale, V., 2011. Bacteria-induced crystallization of kaolinite. Appl. Clay Sci. 53, 566–571.

Fodje, M., Grochulski, P., Janzen, K., Labiuk, S., Gorin, J., Berg, R., 2014. 08B1-1: An automated beamline for macromolecular crystallography experiments at the Canadian Light Source. J. Synchrotron Rad. 21, 633–637.

Fortin, D., Southam, G., Beveridge, T.J., 1994. Nickel sulfide, iron-nickel sulfide and iron sulfide precipitation by a newly isolated Desulfotomaculum species and its relation to nickel resistance. Microb. Ecol. 14, 121-132.

Fujii, T., Moynier, F., Dauphas, N., Abe, M., 2011. Theoretical and experimental investigation of nickel isotopic fractionation in species relevant to modern and ancient oceans. Geochim. Cosmochim. Acta 75 (2), 469–482.

Fujii, T., Moynier, F., Blichert-Toft, J., Albarède, F., 2014. Density functional theory estimation of isotope fractionation of Fe, Ni, Cu and Zn among species relevant to geochemical and biological environments. Geochim. Cosmochim. Acta 140, 553–576.

Gall, L., Williams, H.M., Siebert, C., Halliday, 2012. Determination of mass-dependent variations in nickel isotope compositions using double spiking and MC-ICPMS. J. Anal. At. Spectrom. 27, 137-145.

Gall, L., Williams, H.M., Siebert, C., Halliday, A.N., Herrington, R.J., Hein J. R., 2013. Nickel isotopic compositions of ferromanganese crusts and the constancy of deep ocean inputs and continental weathering effects over the Cenozoic. Earth Planet. Sci. Lett. 375, 148–155.

Gall, L., Williams, Halliday, A.N., Kerr, A.C., 2017. Nickel isotopic composition of the mantle. Geochim. Cosmochim. Acta 199, 196–209.

Gamsjäger, H., Bugajski, J., Gajda, T., Lemire, R.J. and Preis, W.,2005. Chemical thermodynamics of Nickel, Nuclear Energy Agency Data Bank, Organisation for Economic Co-operation and Development, Ed., vol. 6, Chemical Thermodynamics, North Holland Elsevier Science Publishers B. V., Amsterdam, The Netherlands.

Garg, S., Judd, K., Mahadevan, R., Edwards, E., Papangelakis, V.G., 2017. Leaching characteristics of nickeliferous pyrrhotite tailings from the Sudbury, Ontario area. Can. Metall. Q. 56, (4), 372-381.

Genchi, G., Carocci, A., Lauria, G., Sinicropi, M.S., Catalano, A., 2020. Nickel: human health and environmental toxicology. Int. J. Environ. Res. Public Health 17(3), 679.

Gervas, C., Mlowe, S., Akerman, M.P., Itegbeyogene, E.I., Moyo, T., Revaprasadu, N., 2017. Synthesis of rare pure phase Ni_3S_4 and Ni_3S_2 nanoparticles in different primary amine coordinating solvents. Polyhedron 122, 16-24.

Gramp, J.P., Bigham, J.M., Sasaki, K., Tuovinen, O.H., 2007. Formation of Ni- and Zn-Sulfides in Cultures of Sulfate-Reducing Bacteria. Geomicrobiol. J. 24, 609–614.

Gueguen, B., Rouxel, O., Ponzevera, E., Bekker, A., Fouquet Y., 2013. Nickel isotope variations in terrestrial silicate rocks and geological reference materials measured by MC-ICP-MS. Geostand. Geoanalytical Res. 37, 297–317.

Gueguen, B., Rouxel, O., Rouget, M-L., Bollinger, C., Ponzevera, E., Germain, Y., Fouquet, Y., 2016. Comparative geochemistry of four ferromanganese crusts from the Pacific Ocean and significance for the use of Ni isotopes as paleoceanographic tracers. Geochim. Cosmochim. Acta 189, 214–235.

Gueguen, B., Sorensen, J.V., Lalonde, S.V., Peña J., Toner, B.M., Rouxel, O., 2018. Variable Ni isotope fractionation between Fe-oxyhydroxides and implications for the use of Ni isotopes as geochemical tracers. Chem. Geol. 481, 38-52.

Guillard, D., Lewis, A.E., 2001. Nickel hydroxy-carbonate precipitation in a pellet reactor. Ind. Eng. Chem. Res. 40 (23), 5564-5569.

Gunsinger, M.R., Ptacek, C.J., Blowes, D.W., Jambor, J.L., 2006a. Evaluation of long term sulfide oxidation processes within pyrrhotite-rich tailings, Lynn Lake, Manitoba. J. Contam. Hydrol. 83, 149–170.

Gunsinger, M.R., Ptacek, C.J., Blowes, D.W., Jambor, J.L., Moncur, M.C., 2006b. Mechanisms controlling acid neutralization and metal mobility within a Ni-rich tailings impoundment. Appl. Geochem. 21, 1301–1321.

Hall, D.S., Lockwood, D.J., Poirier, S., Bock, C., MacDougall B.R., 2012. Raman and Infrared spectroscopy of α and β phases of thin nickel hydroxide films electrochemically formed on nickel. J. Phys. Chem. A 116, 6771–6784.

Hall, D.S., Lockwood, D.J., Bock, C., MacDougall, B.R., 2014. Nickel hydroxides and related materials: a review of their structures, synthesis and properties. Proc. R. Soc. A. 471, 20140792.

Han, B., He, B., Genga, R., Zhao, X., Li, P., Liang, J., Fan Q., 2019. Ni(II) sorption mechanism at the vermiculite-water interface: Effects of interlayer. J. Mol. Liq. 274, 362-369.

Hayes, J.M., 2004. An introduction to isotopic calculations. http://www.whoi.edu/cms/files/jhayes/2005/9/IsoCalcs30Sept04_5183.pdf

Hoffmann, U., Stipp, S.L.S., 2001. The behavior of Ni^{2+} on calcite surfaces. Geochim. Cosmochim. Acta 65(22), 4131–4139.

Hofmann, A., Bekker, A., Dirks, P., Gueguen, B., Rumble, D., Rouxel O.J., 2014. Comparing orthomagmatic and hydrothermal mineralization models for komatiite-hosted nickel deposits in Zimbabwe using multiple-sulfur, iron, and nickel isotope data. Miner. Deposita 49, 75–100.

Holmström, H., Ljungberg, J., Ekström, M., Öhlander, B., 1999. Secondary copper enrichment in tailings at the Laver mine, northern Sweden. Environ. Geol. 38 (4), 327-342.

Huang, S., 2008. Nanoparticulate nickel sulfide. Ph.D. Dissertation, Cardiff University, Cardiff, Wales.

Huang, S., Harris, K.D.M., Lopez-Capel, E., Manning, D.A.C., Rickard, D., 2009. "Amorphous nickel sulfide" is hydrated nanocrystalline NiS with a core-shell structure. Inorg. Chem. 48, 11486–11488.

Huisman, J.L., Schouten, G., Schultz, C., 2006. Biologically produced sulphide for purification of process streams, effluent treatment and recovery of metals in the metal and mining industry. Hydrometallurgy 83, 106-113.

Hummel, W., Curti, E., 2003. Nickel aqueous speciation and solubility at ambient conditions: a thermodynamic elegy. Monatshefte für Chemie 134, 941–973.

ICDD (2019). PDF-4 + 2019 (Database). Edited by Dr. S. Kabekkodu. (International Centre for Diffraction Data, Newtown Square, PA, USA).

Isaacs, T., 1963. The mineralogy and chemistry of the nickel carbonates. Mineral. Mag. 33, 663-678.

Jamieson-Hanes, J.H., Lentz, A.M., Amos, R.T., Ptacek, C.J., Blowes, D.W., 2014. Examination of Cr(VI) treatment by zero-valent iron using in situ, real-time X-ray absorption spectroscopy and Cr isotope measurements. Geochim. Cosmochim. Acta 142, 299−313.

Jamieson-Hanes, J.H., Shrimpton, H.K., Veeramani, H., Ptacek, C.J., Lanzirotti, A., Newville, M., Blowes, D.W., 2017. Evaluating zinc isotope fractionation under sulfate reducing conditions using a flow-through cell and in situ XAS analysis. Geochim. Cosmochim. Acta 203, 1−14.

Jeong, Y.U., Manthiram A., 2001. Synthesis of nickel sulfides in aqueous solutions using sodium dithionite. Inorg. Chem. 40, 73–77.

Jha, V.K., Kameshima, Y., Nakajima, A., Okada, K., MacKenzie, K.J.D., 2005. Uptake Properties of Ni^{2+} by $nCaO{\cdot}Al_2O_3{\cdot}2SiO_2$ (n=1-4) prepared from solid-state reaction of kaolinite and calcite. J Hazard Mater. 123, 281-287.

Jia, Y., Luo, T., Yu, X.-Y., Liu, J-H., Huang, X-J., 2013. Surfactant-free preparation of nickel carbonate hydroxide in aqueous solution and its toxic ion-exchange properties. New J. Chem. 37 (2) 534-539.

Jiang, D.T., Chen, N., Sheng, W., 2007. Wiggler-based Hard X-ray Spectrocopy Beamline at CLS. AIP Proc. 879 (Accelerators and Beams), 800–803.

Johnson, R.H., Blowes, D.W., Robertson, W.D., Jambor, J.L., 2000. The hydrogeochemistry of the Nickel Rim mine tailings impoundment, Sudbury, Ontario. J. Contam. Hydrol. 41, 49–80.

Karadas, F., Yavuz, C.T., Zulfiqar, S., Aparicio, S., Stucky, G.D., Atilhan, M., 2011. CO_2 adsorption studies on hydroxy metal carbonates $M(CO_3)_x(OH)_y$ (M = Zn, Zn-Mg, Mg, Mg-Cu, Cu, Ni, and Pb) at high pressures up to 175 bar. Langmuir 27 (17), 10642–10647.

Kasprzak, K.S., Sunderman, F.W., Salnikow, K., 2003. Nickel carcinogenesis. Mutat. Res-fund. Mol. M. 533 (1-2), 67–97.

Konhauser, K.O., Urrutia, M.M., 1999. Bacterial clay authigenesis: a common biogeochemical process. Chem. Geol. 161, 399–413.

Kossoff, D., Dubbin, W.E., Alfredsson, M., Edwards, S.J., Macklin, M.G., Hudson-Edwards, K.A., 2014. Mine tailings dams: Characteristics, failure, environmental impacts, and remediation. Appl. Geochem. 51, 229-245.

Kumar, M., Pakshirajan, K., 2020. Novel insights into mechanism of biometal recovery from wastewater by sulfate reduction and its application in pollutant removal. Environ. Technol. Innov. 17, 100542.

Kyser, K., 2012. Isotopes as tracers of elements across the geosphere−biosphere interface. In Isotopic Analysis, Chapter 12; Vanhaecke, F., Degryse, P.; Eds.; Wiley-VCH: Weinheim, pp 351−372.

Lakshtanov, L.Z., Stipp, S.L.S., 2007. Experimental study of nickel (II) interaction with calcite : Adsorption and coprecipitation. Geochim. Cosmochim. Acta 71, 3686–3697.

Langman, J.B., Blowes, D.W., Veeramani, H., Wilson, D., Smith, L., Sego, D.C., Paktunc, D., 2015. The mineral and aqueous phase evolution of sulfur and nickel with weathering of pyrrhotite in a low sulfide, granitic waste rock. Chem. Geol. 401, 169-179.

Lewis, A.E., 2010. Review of metal sulphide precipitation. Hydrometallurgy 104, 222–234.

Lewis, A., van Hille, R., 2006. An exploration into the sulphide precipitation method and its effect on metal sulphide removal. Hydrometallurgy 81 (3-4), 197-204.

Lindsay, M.B. J., Moncur, M.C., Bain, J.G., Jambor, J.L., Ptacek, C.J., Blowes, D.W., 2015. Geochemical and mineralogical aspects of sulfide mine tailings. Appl. Geochem. 57, 157–177.

Liu, P., Ptacek, C.J., Blowes, D.W., Finfrock, Y.Z., 2017. A beam path-based method for attenuation correction of confocal micro-X-ray fluorescence imaging data. J. Anal. At. Spectrom. 32, 1582–1589.

Liu, S., Li, Y., Ju, Y., Liu, J., Shi, Y., 2018. Equilibrium nickel isotope fractionation in nickel sulfide minerals. Geochim. Cosmochim. Acta 222, 1–16.

Mansor, M., Winkler, C., Hochella, M.F., Xu, J., 2019. Nanoparticulate Nickel-Hosting Phases in Sulfidic Environments: Effects of Ferrous Iron and Bacterial Presence on Mineral Formation Mechanism and Solid-Phase Nickel Distribution. Front. Earth Sci. 7, 151.

Martin-Garin, A., Van Cappellen, P., Charlet, L., 2003. Aqueous cadmium uptake by calcite: A stirred flow-through reactor study. Geochim. Cosmochim. Acta 67(15), 2763–2774.

Mavromatis, V., Pearcea, C.R., Shirokova, L.S., Bundeleva, I.A., Pokrovsky, O.S., Benezeth, P., Oelkersa, E.H., 2012. Magnesium isotope fractionation during hydrous magnesium carbonate precipitation with and without cyanobacteria. Geochim. Cosmochim. Acta. 76, 161–174.

McAlary, M.K., 2021. Effectiveness of Organic Carbon Cover Systems on Sulfide-rich Tailings. Master's dissertation, University of Waterloo, ON, Canada. In preparation.

McGregor, R.G., Blowes, D.W., Jambor, J.L., Robertson, W.D., 1998. The solid phase controls on the mobility of heavy metals at the Copper Cliff tailings area, Sudbury, Ontario, Canada. J. Contam. Hydrol. 33, 247–271.

Mokone, T.P., van Hille, R., Lewis A.E., 2012. Metal sulphides from wastewater: Assessing the impact of supersaturation control strategies. Water Res. 46, 2088-2100.

Moncur, M.C., Ptacek, C.J., Blowes, D.W., Jambor, J.L., 2005. Release, transport and attenuation of metals from an old tailings impoundment. Appl. Geochem. 20, 639–659.

Moncur, M.C., Jambor, J.L., Ptacek, C.J., Blowes, D.W., 2009. Mine drainage from the weathering of sulfide minerals and magnetite. Appl. Geochem. 24, 2362–2373.

Moncur, M.C., Blowes, D.W., Ptacek, C.J. , 2013. Pore-water extraction from the unsaturated zone. Can. J. Earth Sci. 50, 1051-1058.

Morse, J.W., 1986. The surface chemistry of calcium carbonate minerals in natural waters: an overview. Mar. Chem. 20, 91-112.

Naldrett, A.J., 1984. Mineralogy and Composition of the Sudbury Ores. In: Geology and Mineral Deposits of the Sudbury Structure (Pye, E.G., A.J. Naldrett and P.E. Giblin, eds.). Ontario Geol. Surv., Spec. Vol. 1, 309–325.

Nickel, E.H., Hallbert, J.A., Halligan, R., 1979. Unusual nickel mineralisation at Nullagine, Western Australia. J Geol Soc Aust. 26, 61-71.

Nickel, E.H., Berry, L.G., 1981. The new mineral nullaginite and additional data on the related minerals rosasite and glaukosphaerite. Can. Min. 19, 315–324.

Nieminen, T.M., Ukonmaanaho, L., Rausch, N., Shotyk, W., 2007. Biogeochemistry of nickel and its release into the environment. Met. Ions Life Sci. 2, 1-30.

Olivas, A., Cruz-Reyes, J., Petranovski, V., Avalo,s M., Fuentes, S., 1998. Synthesis and characterization of nickel sulfide catalysts. J. Vac. Sci. Technol. 16, 3515-3520.

Pandyia, K. I., O'Grady, W. E., Corrigan, D. A., McBreen, J., Hoffman, R. W., 1990. Extended x-ray absorption fine structure investigations of nickel hydroxides. J. Phys. Chem. 94, 21-26.

Parkhurst, D.L., Appelo, C.A.J., 1999. User's Guide to PHREEQC (Version 2) – A computer program for speciation, batch- reaction, one-dimensional transport, and inverse geochemical calculations. U.S. Geological Survey Water-Resources Investigations Report 99–4259, 312 p.

Parigi, R., Chen, N., Reid, J. W., Ptacek, C. J., Blowes, D. W, 2020. Nickel isotope fractionation during precipitation of Ni secondary minerals and synchrotron-based analysis of the precipitates. In submission.

Pasava, J., Chrastný, V., Loukola-Ruskeeniemi, K., Šebek, O., 2019. Nickel isotopic variation in black shales from Bohemia, China, Canada,and Finland: a reconnaissance study. Miner. Deposita 54: 719.

Patterson, J.W., Allen, H.E., Scala, J.J., 1977. Carbonate precipitation for heavy metals pollutants. J. Water Pollut. Control Fed. 49 (12), 2397-410.

Perchiazzi, N., 2006. Crystal structure determination and Rietveld refinement of rosasite and mcguinnessite. Z. Kristallogr. Suppl. 23, 505-510.

Perchiazzi, N., Merlino, S., 2006. The malachite-rosasite group: crystal structures of glaukosphaerite and pokrovskite. Eur. J. Mineral. 18, 787-792.

Perchiazzi, N., Demitri, N., Fehér, B., Vignola, P., 2017. On the crystal-chemistry of rosasite and parádsasvárite. Can. Mineral. 55, 1-14.

Porter, S.J., Selby, D., Cameron, V., 2014. Characterising the nickel isotopic composition of organic-rich marine sediments. Chem. Geol. 387, 12–21.

Qian, J., Zhu, X., Tao, Y., Zhou, Y., He, X., and Li, D., 2015. Promotion of Ni2+ Removal by Masking Toxicity to Sulfate-Reducing Bacteria: Addition of Citrate. Int. J. Mol. Sci. 16, 7932-7943.

Qiang, S., Bin Han, B., Zhao, X., Yunbo, Y., Shao, D., Li, P., Liang, J., Fan Q., 2017. Sorption of Nickel(II) on a Calcareous Aridisol Soil, China: Batch, XPS, and EXAFS Spectroscopic Investigations. Sci. Rep. 7:46744.

Ramesh, T.N., Kamath P.V., 2006. Synthesis of nickel hydroxide: Effect of precipitation conditions on phase selectivity and structural disorder. J. Power Sources. 156, 655–661.

Ratié, G., Jouvin, D., Garnier, J., Rouxel, O., Miska, S., Guimaraes, E., Cruz Vieira, L., Sivry, Y., Zelano, I., Montarges-Pelletier, E., Thil, F., Quantin, C., 2015. Nickel isotope fractionation during tropical weathering of ultramafic rocks. Chem. Geol. 402 (0), 68–76.

Ratié, G., Quantin, C., Jouvin, D., Calmels, D., Ettler, V., Sivry, Y., Cruz Vieira, L., Ponzevera, E., Garnier, J., 2016. Nickel isotope fractionation during laterite Ni ore smelting and refining: implications for tracing the sources of Ni in smelter affected soils. Appl. Geochem 64, 136-145.

Ratié, G., Garnier, J., Calmels, D.,Vantelon, D., Guimarães, E., Monvoisin, G., Nouet, J., Ponzevera, E., Quantin, C., 2018. Nickel distribution and isotopic fractionation in a Brazilian lateritic regolith: Coupling Ni isotopes and Ni K-edge XANES. Geochim. Cosmochim. Acta 230, 137-154.

Ratié, G., Quantin, C., De Freitas, M.A., Echevarria, G., Ponzevera, E., Garnier, J., 2019. The behavior of nickel isotopes at the biogeochemical interface between ultramafic soils and Ni accumulator species. J. Geochem. Explor. 196, 182-191.

Ravel, B. and Newville, M., 2005. Athena, Artemis, Hephaestus: Data analysis for X-ray absorption spectroscopy using IFEFFIT. J. Synchrotron Radiat. 12, 537–541.

Rehr, J.J., Albers, R.C., 2000. Theoretical approaches to x-ray absorption fine structure. Rev. Mod. Phys. 72, 621-654.

Reis, F.D., Silva, A.M., Cunha, E.C., Leão, V.A., 2013. Application of sodium- and biogenic sulfide to the precipitation of nickel in a continuous reactor. Sep. Purif. Technol. 120, 346-353.

Ressler, T., 1997. WinXAS: a new software package not only for the analysis of energy dispersive XAS data. J. Phys. IV France 7 C2-269-C2-270.

Rezaeia, S., Liu, F., Marcuson, S., Muinonen, M., Lakshmanan, V.L., Sridhar, R., Barati, M., 2017. Canadian pyrrhotite treatment: the history, inventory and potential for tailings processing. Can. Metall. Q. 56, (4), 410-417.

Romanek, C.S., Beard, B., Anbar A.D., and Andrus C.F.T., 2010. Non-traditional stable isotopes in environmental sciences. In Environmental Isotopes in Biodegradation and Bioremediation, Chapter 12; Aelion C. M., Höhener P., Hunkeler D., Aravena R., Eds.; CRC Press: Boca Raton, 2010; pp 385−435.

Rudge, J.F., Reynolds, B.C., Bourdon B., 2013.The double spike toolbox. Chem. Geol. 265 (3), 420–431.

Salcedo, A.F.M, Ballesteros, F.C., Vilando, A.C., Lu M-C., 2016. Nickel recovery from synthetic Watts bath electroplating wastewater by homogeneous fluidized bed granulation process. Sep. Purif. Technol. 169, 128-136.

Schauble, E.A., 2004. Applying stable isotope fractionation theory to new systems. Rev. Mineral. Geochem. 55 (1), 65–111.

Schaumlöffel, D., 2012. Nickel species: analysis and toxic effects. J. Trace Elem. Med. Biol. 26 (1), 1-6.

Scheidegger, A.M., Sparks, D.L., 1996. Kinetics of the formation and the dissolution of nickel surface precipitates on pyrophyllite. Chem. Geol. 132, 157-164.

Scheidegger, A.M., Lamble, G.M., Sparks, D.L., 1998. The kinetics of mixed Ni-Al hydroxide formation on clay and aluminum oxide minerals: A time-resolved XAFS study. Geochim. Cosmochim. Acta 62, 2233–2245.

Scheinost, A.C., Ford, R.G., Sparks D.L., 1999. The role of Al in the formation of secondary Ni precipitates on pyrophyllite, gibbsite, talc, and amorphous silica: A DRS study. Geochim. Cosmochim. Acta 63, 3193–3203.

Shrimpton, H.K., Jamieson-Hanes, J.H., Ptacek, C.J., Blowes, D.W., 2018. Real-Time XANES measurement of Se reduction by zerovalent iron in a flow-through cell, and accompanying Se isotope measurements. Environ. Sci. Technol. Lett. 52, 9304–9310.

Siebert, C., Nägler, T.F., Kramers, J.D., 2001. Determination of molybdenum isotope fractionation by double-spike multicollector inductively coupled plasma mass spectrometry. Geochem. Geophys. Geosyst. 2, DOI: 10.1029/2000GC000124.

Singh, R., Paul, D., Jain, R. K., 2006. Biofilms: implications in bioremediation. Trends Microbiol. 14 (9), 389-397.

Sitte, J., Pollok, K., Langenhorst, F., and Küsel, K., 2013. Nanocrystalline nickel and cobalt sulfides formed by a heavy metal-tolerant, sulfate-reducing enrichment culture. Geomicrobiol. J. 30, 36–47.

Smith, R.S., Wiederhold, J.G., Kretzschmar, R., 2015. Mercury isotope fractionation during precipitation of metacinnabar (β-HgS) and montroydite (HgO). Environ. Sci. Technol. 49, 4325−4334.

Song, Q., Tang, Z., Guo, H., Chan, S.L.I., 2002. Structural characteristics of nickel hydroxide synthesized by a chemical precipitation route under different pH values. J. Power Sources. 112, 428–434.

Sorensen, J.V., Gueguen, B., Stewart, B.D., Peña, J., Rouxel, O., Toner, B.M., 2020. Large nickel isotope fractionation caused by surface complexation reactions with hexagonal birnessite. Chem. Geol. 537, 119481.

Spivak-Birndorf, L.J., Wang, S., Bish, D.L., Wasylenki, L.E., 2018. Nickel isotope fractionation during continental weathering. Chem. Geol. 476, 316-326.

Stipp, S. L., Hochella Jr., M. F., Parks, G. A., Leckie, J. O., 1992. Cd^{2+} uptake by calcite, solid-state diffusion, and the formation of solid-solution: Interface processes observed with near-surface sensitive techniques (XPS, LEED, and AES). Geochim. Cosmochim. Acta 56(5), 1941–1954.

Tanimizu, M., Hirata, T., 2006. Determination of natural isotopic variation in nickel using inductively coupled plasma mass spectrometry. J. Anal. At. Spectrom. 21, 1423–1426.

Tazaki, K., 2005. Microbial formation of a halloysite-like mineral. Clays Clay Miner. 53, 224–233.

Toby, B.H., Von Dreele, R.B., 2013. GSAS II: the genesis of a modern open-source all-purpose crystallography software package. J. Appl. Crystallogr. 46, 544–549.

Tossell, J.A., Vaughan, D.J., Burdett J.K.,1981. Pyrite, marcasite, and arsenopyrite type minerals: crystal chemical and structural principles. Phys. Chem. Minerals 7, 177-184.

Veeramani, H., Eagling, J., Jamieson-Hanes, J.H., Kong, L., Ptacek, C.J., Blowes, D.W., 2015. Zinc isotope fractionation as an indicator of geochemical attenuation processes. Environ. Sci. Technol. Lett. 2, 314–319.

Villegas-Jiménez, A., Mucci, A., Pokrovsky, O.S., Schott, J., 2010. Acid-base behavior of the gaspeite ($NiCO_3$(s)) surface in NaCl solutions. Langmuir 26 (15), 12626-12639.

Wang, S.J., Wasylenki, L.E., 2017. Experimental constraints on reconstruction of Archean seawater Ni isotopic composition from banded iron formations. Geochim. Cosmochim. Acta. 206, 137–150.

Wang, R.M., Archer, C., Bowie, A.R., Vance, D., 2019. Zinc and nickel isotopes in seawater from the Indian Sector of the Southern Ocean: The impact of natural iron fertilization versus Southern Ocean hydrography and biogeochemistry. Chem. Geol. 511, 452-464.

Wasylenki, L.E., Howe, H.D., Spivak-Birndorf, L.J., Bish, D.L., 2015. Ni isotope fractionation during sorption to ferrihydrite: implications for Ni in banded iron formations. Chem. Geol. 400 (0), 56–64.

Wiederhold, J. G, 2015.Metal stable isotope signatures as tracers in environmental geochemistry. Environ. Sci. Technol 49, 2606–2624.

Wiesli, R.A., Beard, B.L., Johnson C.M., 2004. Experimental determination of Fe isotope fractionation between aqueous Fe(II), siderite and "green rust" in abiotic systems. Chem. Geol. 211, 343−362.

Wilkin, R.T., Rogers, D.A., 2010. Nickel sulfide formation at low temperature: Initial precipitates, solubility and transformation products. Environ. Chem. 7, 514–523.

Xu, Y., Axe, L., Boonfueng, T., Tyson, T.A., Trivedi, P., Pandya, K., 2007. Ni(II) complexation to amorphous hydrous ferric oxide: an X-ray absorption spectroscopy study. J. Colloid Interface Sci. 314, 10–17.

Xu, J., Murayama, M., Roco, C. M., Veeramani, H., Michel, M., Rimstidt, J. D., Winkler, C., Hochella Jr., M. F., 2016. Highly-defective nanocrystals of ZnS formed via dissimilatory bacterial sulfate reduction: A comparative study with their abiogenic analogues. Geochim. Cosmochim. Acta. 180, 1-14.

Yang, S-C., Hawco, N.J., Pinedo- González, P., Bian, X., Huang, K-F., Zhang, R., John, S.G., 2020. A new purification method for Ni and Cu stable isotopes in seawater provides evidence for widespread Ni isotope fractionation by phytoplankton in the North Pacific. Chem. Geol. 547, 119662.

Yuan Tian, Y., Etschmann, B., Liu, W., Borg, S., Mei, Y., Testemale, D., O'Neill, B., Rae, N., Sherman, D.M., Ngothai, Y., Johannessen, B., Glover, C., Brugger J., 2012. Speciation of nickel (II) chloride complexes in hydrothermal fluids: In situ XAS study. Chem. Geol. 334, 345-363.

Zachara, J. M., Kittrick J. A., Dake, L. S., Harsh, J. B., 1989. Solubility and surface spectroscopy of zinc precipitates on calcite. Geochim. Cosmochim. Acta, 53(1), 9–19.

Zachara, J. M., Cowan, C. E., Resch, C. T., 1991. Sorption of divalent metals on calcite. Geochim. Cosmochim. Acta 55(6), 1549–1562.

Zavarin, M., Doner, H., 1998. Nickel and Manganese Interaction with Calcite. 1998 SSRL Activity Report. https://digital.library.unt.edu/ark:/67531/metadc626636/m1/3/.

Zelano, I.O., Cloquet, C., Fraysse, F., Dong, S., Janot, N., Echevarria, G., Montargès-Pelletier E., 2018. The influence of organic complexation on Ni isotopic fractionation and Ni recycling in the upper soil layers. Chem. Geol. 483, 47-55.

Zelano, I.O., Cloquet, C., Van der Ent, A., Echevarria, G., Gley, R., Landrot, G., Pollastri, S., Fraysse, F., Montargès-Pelletier, E., 2020. Coupling nickel chemical speciation and isotope ratios to decipher nickel dynamics in the Rinorea cf. bengalensis-soil system in Malaysian Borneo. Plant Soil 454, 225–243.

APPENDIX A

SUPPORTING INFORMATION FOR CHAPTER 2

Table S2.1: $Ni(OH)_2$ time to equilibrium experiment results. The molar ratio used was [Ni:OH] = 1.5:1

Time (hours)	Final pH	mmol L^{-1} Ni in solution	δ^{60}Ni solution	2σ (‰)
0	5.83	31.5	0	0.06
0.3	7.77	22.03	0.21	0.05
2.3	7.59	21.2	0.20	0.06
6	7.19	21.8	0.22	0.05
13	7.47	22.1	0.21	0.05
24	7.15	21.6	0.20	0.05
48	7.11	22.8	0.20	0.05
72	7.06	22.4	0.20	0.07
168	6.93	22.8	0.21	0.05
336	6.54	22.4	0.21	0.04
730	6.68	22.1	0.24	0.05
1460	6.85	21	0.21	0.05

Table S2.2: $NiCO_3$ time to equilibrium experiment results. The molar ratio used was [$Ni:CO_3$] = 2:1

Time (hours)	Final pH	mmol L^{-1} Ni in solution	δ^{60}Ni solution	2σ (‰)
0	5.83	37.8	0	0.06
0.3	7.65	22.9	0.26	0.05
2.3	7.71	23	0.27	0.05
6	7.67	23.3	0.25	0.05
13	7.60	23.04	0.31	0.06
24	7.64	23	0.24	0.05
48	7.61	22.8	0.22	0.05
72	7.65	22.4	0.20	0.06
168	7.60	22.7	0.21	0.05
336	7.59	22.7	0.18	0.06
730	7.54	22.9	0.22	0.05
1460	7.50	22.3	0.20	0.05

Table S2.3: NiS time to equilibrium experiment results. The molar ratio used was [Ni:S] = 2:1

Time (hours)	Final pH	mmol L^{-1} Ni in solution	δ^{60}Ni solution	2σ (‰)
0	6.02	38.3	0	0.05
0.3	4.06	18.3	0.95	0.05
2.3	3.75	18.1	0.98	0.05
6	3.80	18.5	0.86	0.06
13	3.60	18.3	0.96	0.05
24	4.27	18.5	0.97	0.05
48	5.58	18.5	0.97	0.07
72	6.15	18.7	0.96	0.05
168	6.72	18.4	0.96	0.06
336	7.08	17.3	0.97	0.05
730	7.37	18.5	0.96	0.05
1460	7.44	19.3	0.96	0.05

Table S2.4: Batch experiments results for varying [Ni/counteranion] molar ratios

Ni:OH	Final pH	Ni f in solution	δ^{60}Ni solution	2σ (‰)
4:1	6.5	0.83	0.03	0.05
3:1	6.62	0.82	0.08	0.05
1.6:1	6.96	0.68	0.22	0.05
1:1	7.17	0.38	0.52	0.05
1:1.8	8.5	0.17	0.73	0.05
1:2	8.4	0.08	0.92	0.05
Ni:CO_3	**Final pH**	**Ni f in solution**	**δ^{60}Ni solution**	**2σ (‰)**
5:1	7.33	0.86	0.06	0.08
4:1	7.37	0.84	0.08	0.08
3:1	7.41	0.73	0.14	0.06
2:1	7.47	0.58	0.25	0.05
1.6:1	7.69	0.50	0.43	0.06
1:1	7.93	0.15	0.94	0.05
Ni:S	**Final pH**	**Ni f in solution**	**δ^{60}Ni solution**	**2σ (‰)**
7:1	5.95	0.74	0.17	0.05
6:1	6.05	0.71	0.19	0.05
5:1	6.17	0.66	0.22	0.06
4:1	6.25	0.59	0.48	0.05
3:1	6.33	0.49	0.63	0.05
1.5:1	6.19	0.18	1.21	0.07

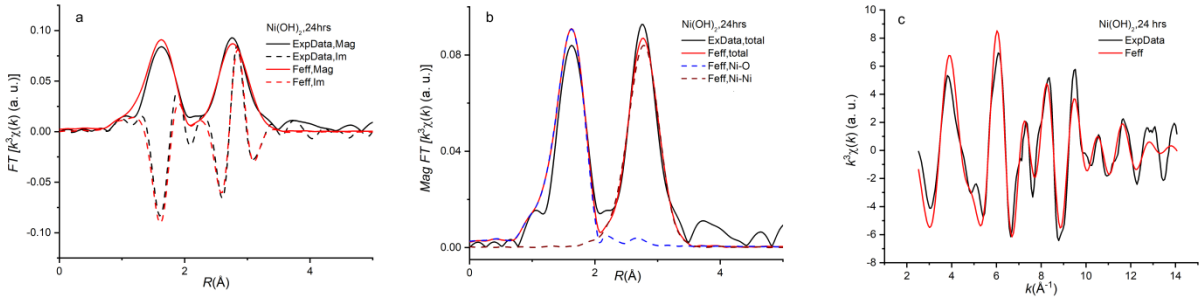

Figure S2.1: $Ni(OH)_2$-24 hrs sample results: a) Comparison between ExpData vs Feff modeling in both magnitude of the Fourier transform (FT) and the imaginary part of the FT; b) Comparison between ExpData vs Feff modeling of the FT magnitude for the total and individual scattering paths; c) Comparison in k space between ExpData vs Feff modeling based on the parameters from R space curve fitting.

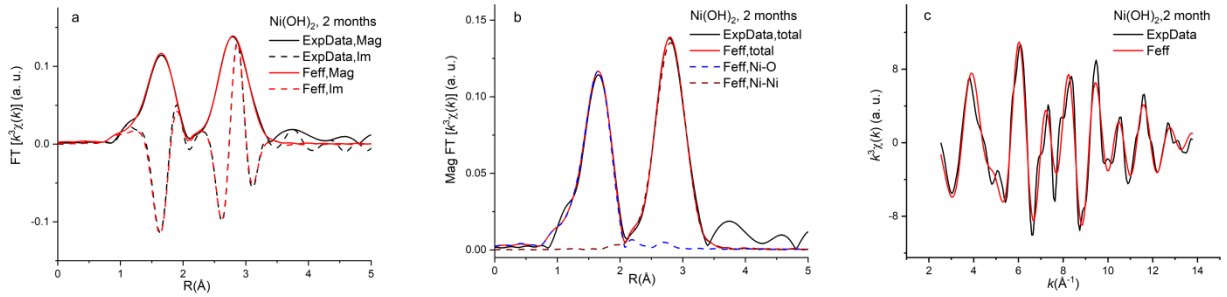

Figure S2.2: $Ni(OH)_2$-2months sample results: a) Comparison between ExpData vs Feff modeling in both magnitude of the Fourier transform (FT) and the imaginary part of the FT; b) Comparison between ExpData vs Feff modeling of the FT magnitude for the total and individual scattering paths; c) Comparison in k space between ExpData vs Feff modeling based on the parameters from R space curve fitting.

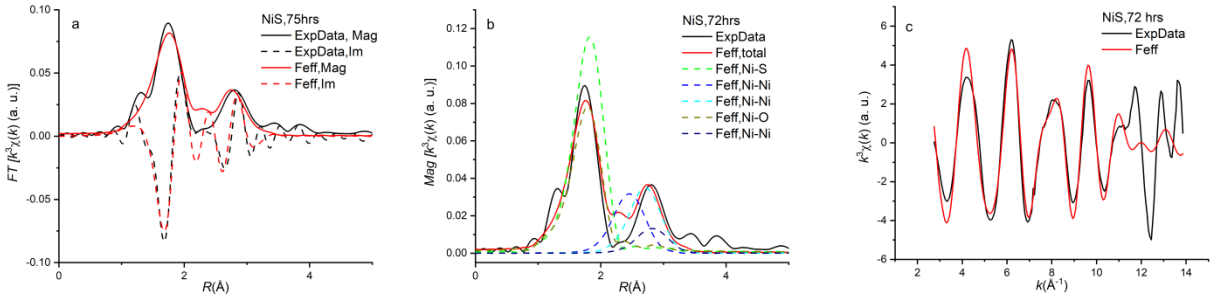

Figure S2.3: NiS-72 hrs sample results: a) Comparison between ExpData vs Feff modeling in both magnitude of the Fourier transform (FT) and the imaginary part of the FT; b) Comparison between ExpData vs Feff modeling of the FT magnitude for the total and individual scattering paths; c) Comparison in k space between ExpData vs Feff modeling based on the parameters from R space curve fitting.

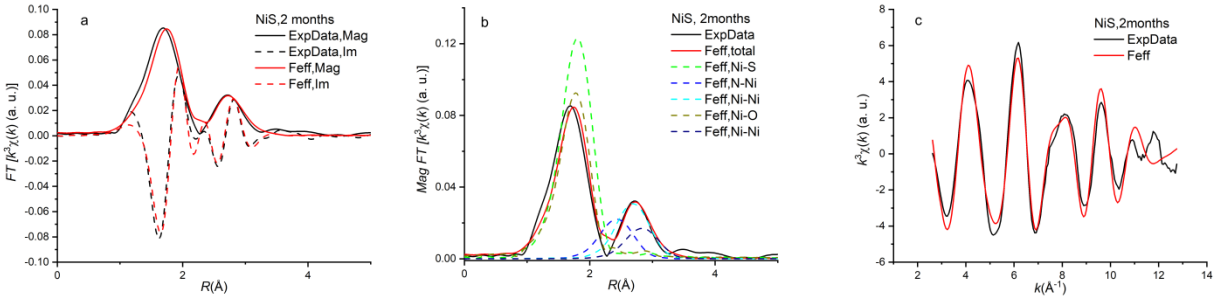

Figure S2.4: NiS-2 month sample results: a) Comparison between ExpData vs Feff modeling in both magnitude of the Fourier transform (FT) and the imaginary part of the FT; b) Comparison between ExpData vs Feff modeling of the FT magnitude for the total and individual scattering paths; c) Comparison in k space between ExpData vs Feff modeling based on the parameters from R space curve fitting.

APPENDIX B

SUPPORTING INFORMATION FOR CHAPTER 3

Table S3.1: Ni and S fraction in solution (f), pH and δ^{60}Ni relative to each sample collected after 1 hour, 1 day and 1 week. δ^{60}Ni values are expressed relative to the input solution.

Uncertainty on each isotope measurement is reported as two times the standard deviation (2σ) calculated on three analytical events.

Sample	Ni f in solution after 1 hour	Total S f in solution after 1 hour	pH after 1 hour	δ^{60}Ni (‰) solution 1 hour	2σ (‰)	δ^{60}Ni (‰) solid 1 hour	2σ (‰)	Ni f in solution after 1 day	Total S f in solution after 1 day	pH after 1 day	δ^{60}Ni (‰) solution 1 day	2σ (‰)	δ^{60}Ni (‰) solid 1 day	2σ (‰)	Ni f in solution after 1 week	Total S f in solution after 1 week	pH after 1 week	δ^{60}Ni (‰) solution 1 week	2σ (‰)	δ^{60}Ni (‰) solid 1 week	2σ (‰)
10 mM	0.83	0.65	6.1	0.20	0.08	-1.73	0.05	0.52	0.63	6.0	0.79	0.05	-1.07	0.05	0.05	0.53	5.9	2.59	0.06	-0.11	0.05
15 mM	0.88	0.64	6.1	0.18	0.05	-1.72	0.05	0.76	0.62	6.0	0.40	0.08	-1.56	0.05	0.34	0.53	5.8	1.56	0.05	-0.49	0.05
20 mM	0.86	0.62	6.0	0.04	0.08	-1.91	0.05	0.76	0.60	5.9	0.33	0.08	-1.58	0.05	0.56	0.51	5.7	1.10	0.05	-1.07	0.08
25 mM	0.83	0.62	5.9	0.16	0.06	-1.85	0.07	0.80	0.58	5.8	0.17	0.06	-1.72	0.05	0.57	0.50	5.7	0.97	0.05	-1.04	0.05
30 mM	0.92	0.62	5.8	0.08	0.06	-1.97	0.08	0.79	0.58	5.8	0.35	0.05	-1.54	0.08	0.65	0.50	5.6	0.48	0.05	-1.36	0.05
40 mM	0.91	0.61	5.8	0.04	0.06	-1.97	0.05	0.75	0.57	5.7	0.32	0.05	-1.54	0.05	0.74	0.49	5.6	0.40	0.05	-1.42	0.05

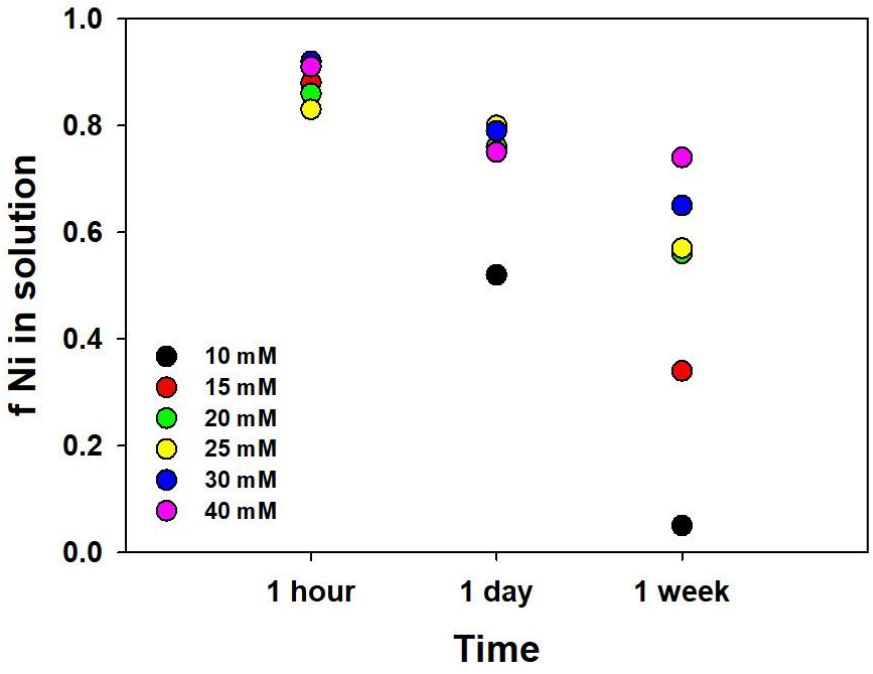

Figure S3.1: Fraction of Ni remaining in solution (f) relative to each sample collected after 1 hour, 1 day and 1 week.

Figure S3.2: A) Shiny metallic precipitate forming on 10mM sample bottle walls after 1 day. B) Shiny metallic precipitate forming on 10mM sample bottle walls after 3 days. C) Shiny metallic precipitate forming on 10mM sample bottle walls after 1 week.

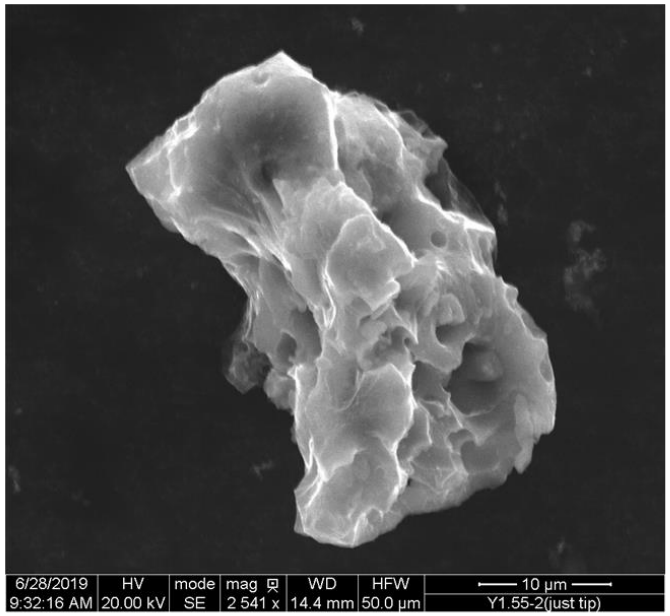

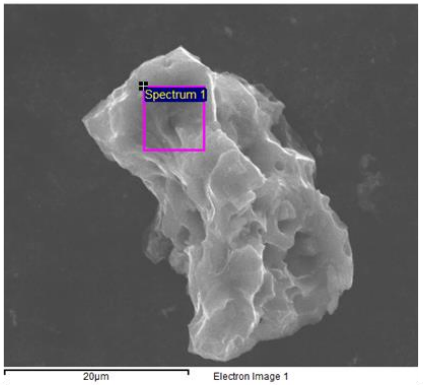

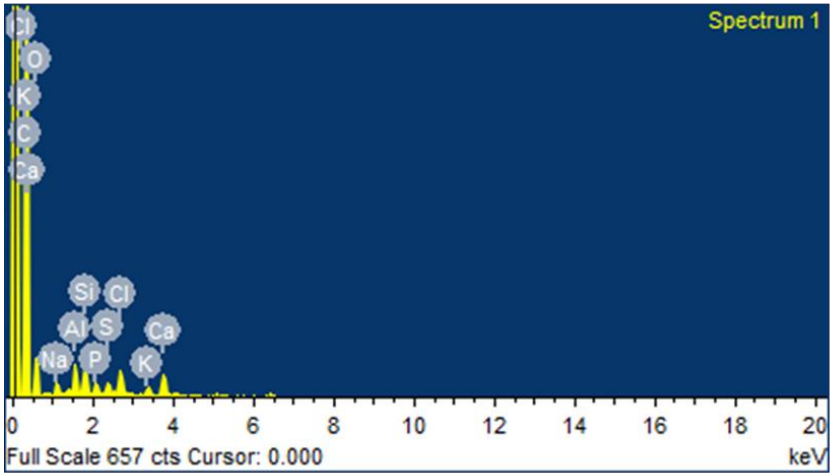

Element	Weight%	Atomic%	
C K	77.08	83.92	
O K	16.36	13.37	
Na K	0.52	0.29	
Al K	1.03	0.50	
Si K	0.97	0.45	
P K	0.48	0.20	
S K	0.57	0.23	
Cl K	1.09	0.40	
K K	0.44	0.15	
Ca K	1.45	0.47	
Totals	100.00		

Figure S3.3: SEM-EDS analysis of a grain which shows clay-like components.

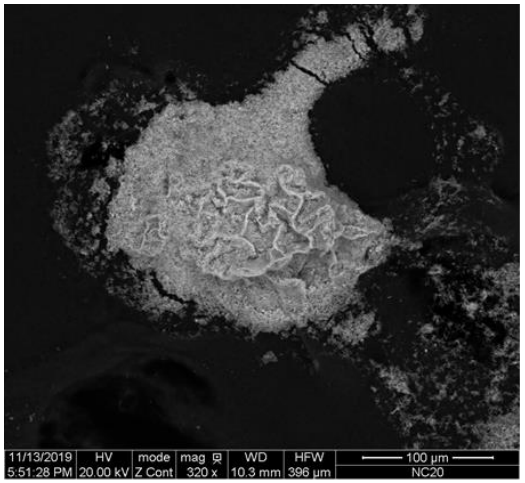

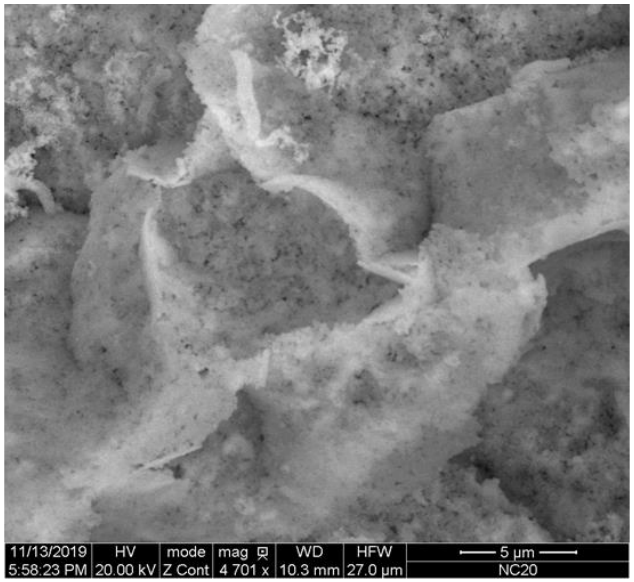

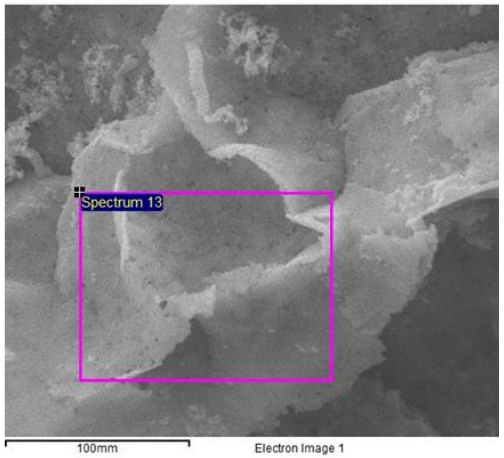

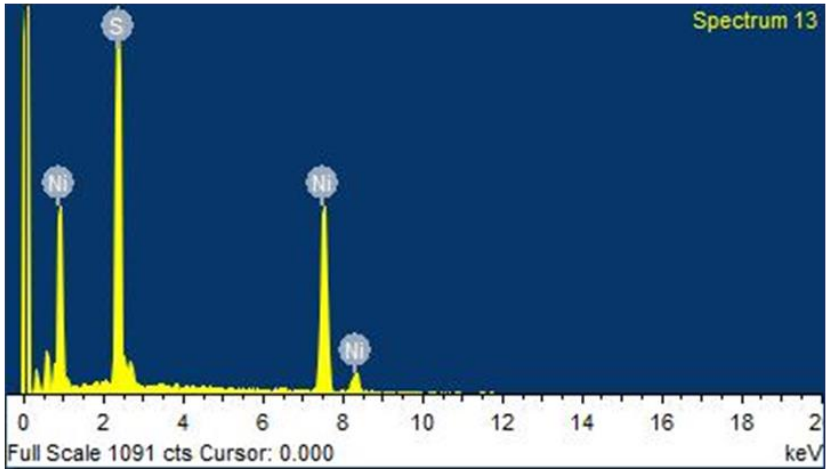

Element	Weight%	Atomic%	
S K	32.27	46.60	
Ni K	67.73	53.40	
Totals	100.00		

Figure S3.4: SEM-EDS analysis of a NiS grain which shows a flower–like appearance characteristic of α-NiS phase.

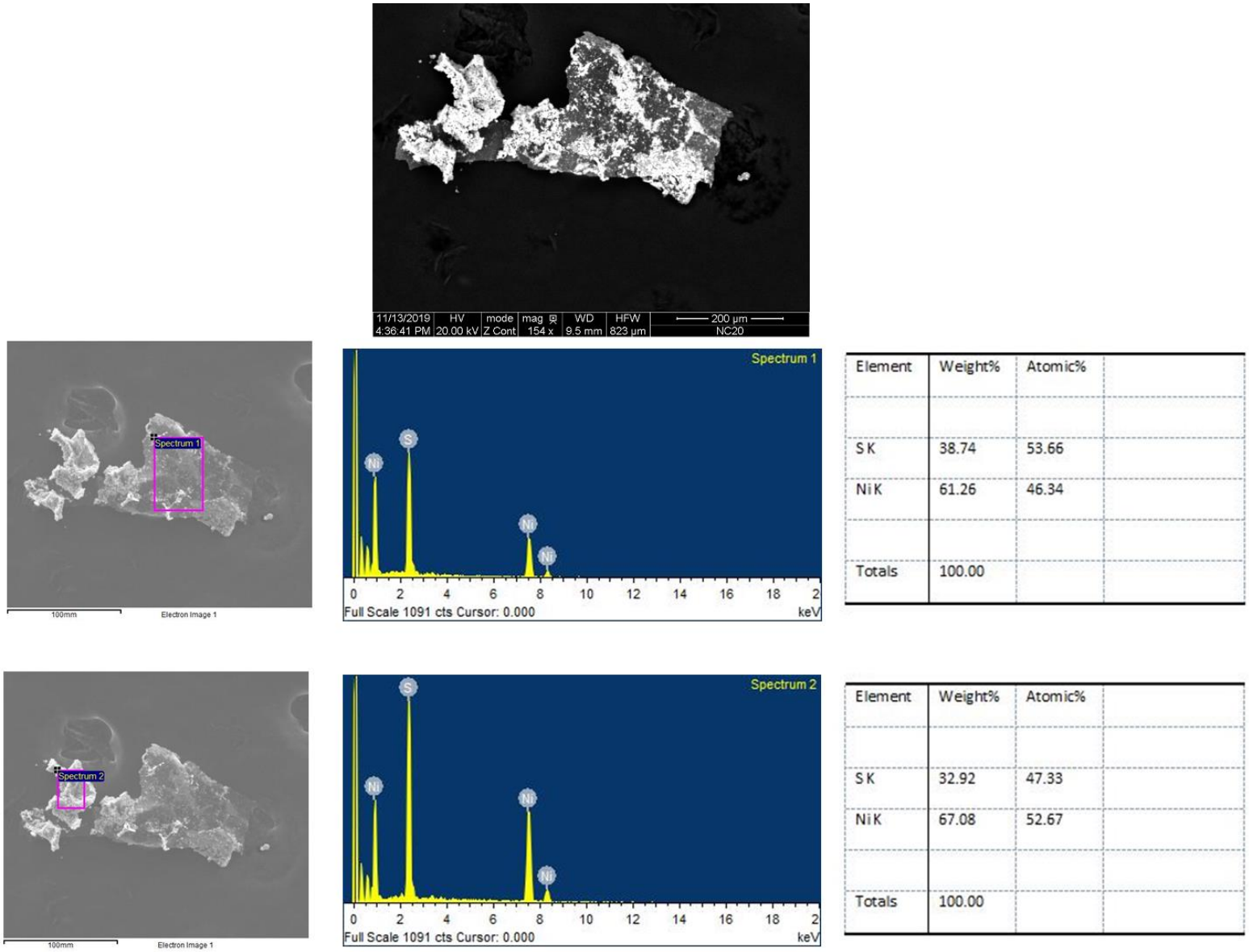

Figure S3.5: SEM-EDS analysis of a freeze-dried shiny precipitate aggregate showing NiS composition.

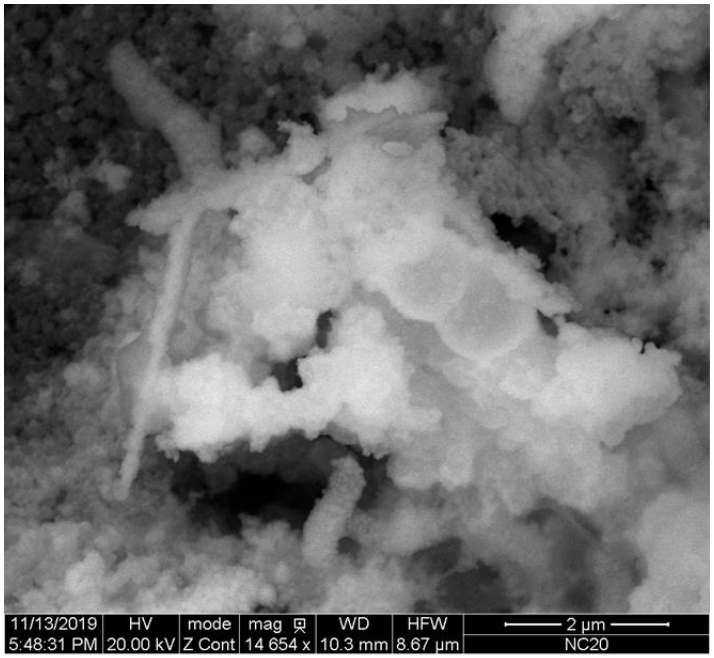

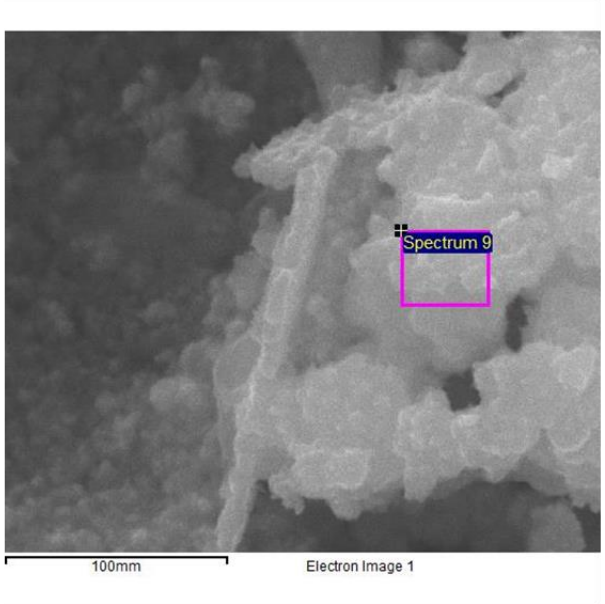

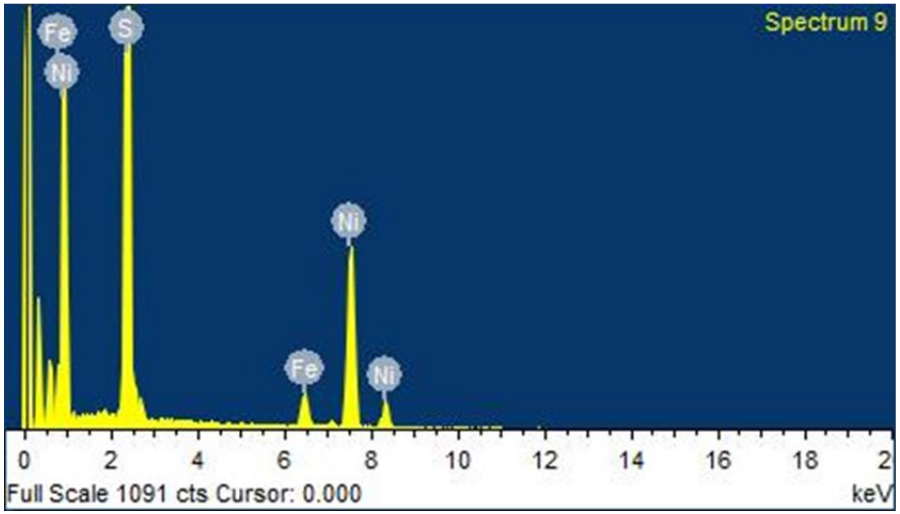

Element	Weight%	Atomic%	
S K	37.00	51.69	
Fe K	6.07	4.87	
Ni K	56.93	43.44	
Totals	100.00		

Figure S3.6: SEM-EDS analysis of a fresh shiny precipitate aggregate showing NiS composition with some Fe substituting for Ni.

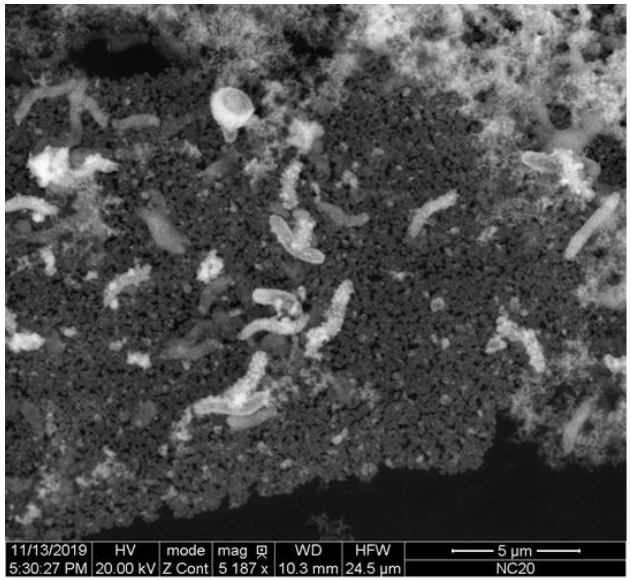

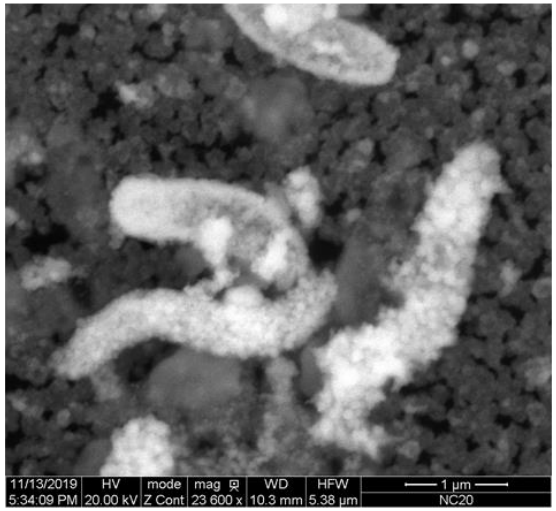

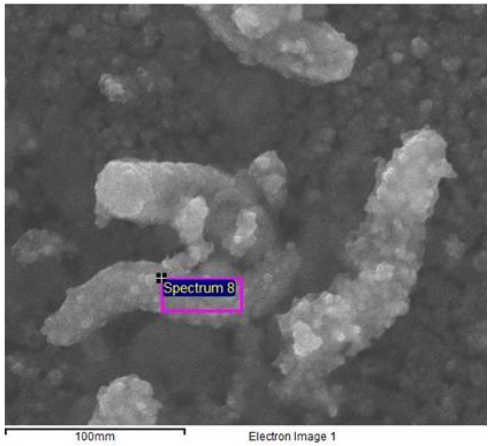

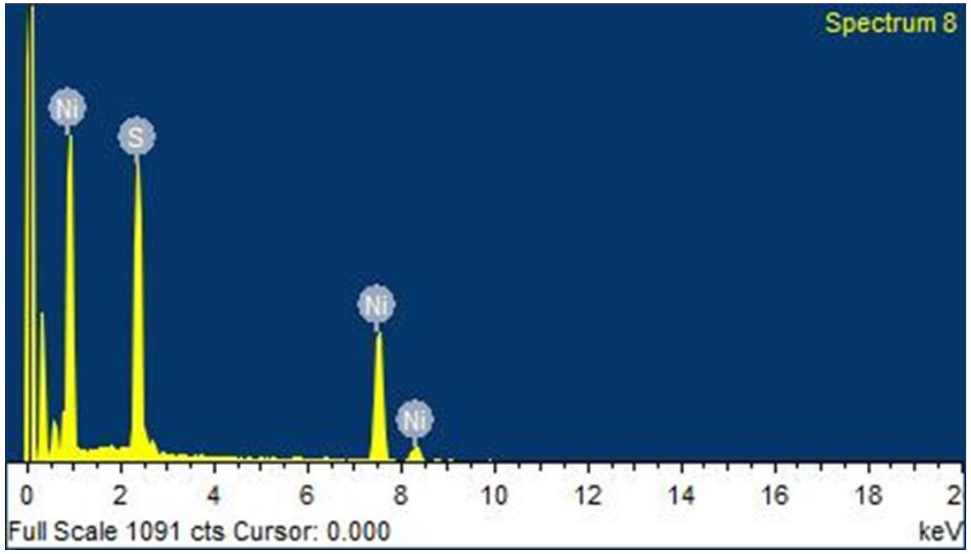

Element	Weight%	Atomic%	
S K	33.47	47.95	
Ni K	66.53	52.05	
Totals	100.00		

Figure S3.7: SEM-EDS analysis of the SRB showing NiS precipitate covering the bacteria.

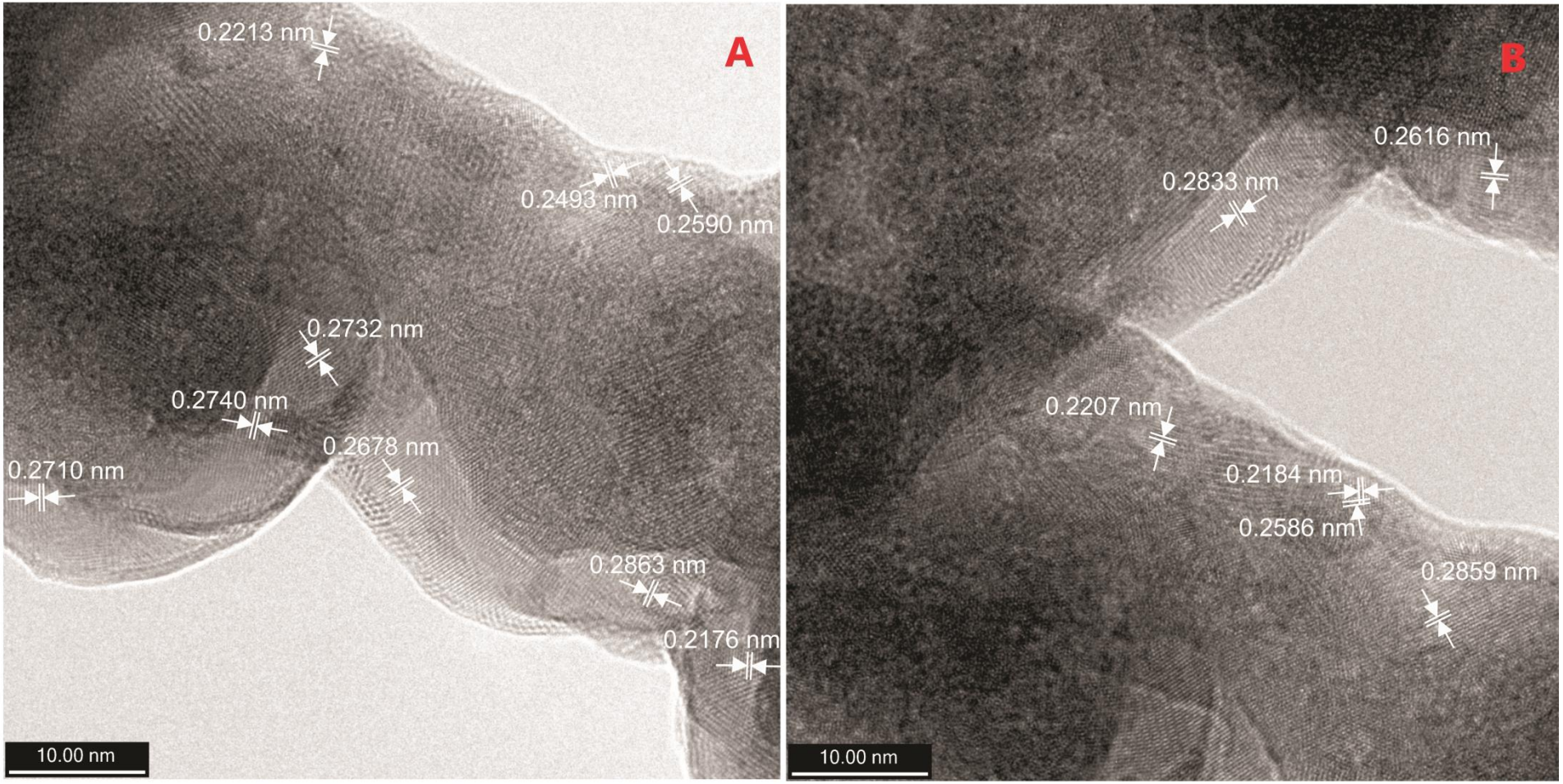

Figure S3.8: TEM images showing lattice fringe spacing measurements performed on the black precipitate at the bottom of the bottles which constituted the smallest grain-size portion of the solid product. The measured d-spacing values confirm the presence of multiple Ni sulfides, such as: millerite (β-NiS), d(Å)= 2.22 (211), 2.51 (021), and 2.77 (300); α-NiS, d(Å)= 2.60 (101); Vaesite (NiS2), d(Å)= 2.54 (210), and 2.84(200) ; polydymite (Ni_3S_4), d(Å)= 2.86 (311).

APPENDIX C

SUPPORTING INFORMATION FOR CHAPTER 4

Table S4.1: Results from the FTC experiments showing sampling time, Ca and Ni concentrations, pH, and δ^{60}Ni with associated standard deviation (2σ) of effluent samples.

Time (hrs)	Ca (mg L^{-1})	Ni (mg L^{-1})	pH	δ^{60}Ni	2σ
0.15	6.4	0.06			
0.45	6.4	0.04			
1.15	6.4	0.08			
1.45	6.5	0.07			
2.15	7.2	0.04			
2.45	7.7	0.1			
3.15	9.0	0.1			
3.45	9.9	0.1			
4.15	10.8	0.02			
4.45	12.2	0.3			
5.15	14.9	0.5			
5.45	18.4	1.3			
6.15	22.6	2.1			
6.45	27.0	2.9	7.2		
7.15	30.7	3.6			
7.45	34.5	4.4			
8.15	36.7	5.2		1.08	0.05
8.45	38.1	6.4			
9.15	39.9	7.6			
9.45	40.1	8.9		0.74	0.05
10.15	40.9	10.1			
10.45	40.5	11.4			
11.15	40.3	12.4			
12.15	39.2	15.0			
12.45	39.4	16.1		0.52	0.08
13.15	37.6	17.4	7.5		
13.45	36.2	18.4			
14.15	35.9	19.8			
14.45	35.0	20.7		0.42	0.05
15.15	34.3	21.4		0.35	0.05
15.45	33.3	22.4			

Time (hrs)	Ca (mg L^{-1})	Ni (mg L^{-1})	pH	δ^{60}Ni	2σ
16.15	33.2	23.2			
16.45	32.3	23.8			
17.15	31.5	24.7			
17.45	31.7	25.5			
18.15	31.3	26.2			
18.45	30.7	26.7			
19.15	30.0	27.4			
19.45	28.8	27.2			
20.15	29.4	28.3			
20.45	29.1	28.8			
21.15	28.8	29.1	7.6	0.22	0.05
21.45	27.8	29.5			
22.15	27.8	30.2			
22.45	27.4	30.2			
23.15	27.7	30.7			
23.45	27.4	30.9			
24.15	26.7	31.1		0.22	0.05
24.45	27.0	31.2			
25.15	26.9	31.4			
25.45	26.8	31.7			
26.15	26.4	31.7			
26.45	25.8	31.9			
27.15	26.1	32.1			
27.45	26.0	32.2			
28.15	25.8	32.4			
29.15	26.6	33.1			
29.45	26.1	33.3			
30.15	26.1	34.1		0.17	0.05
30.45	25.5	33.8		0.27	0.05
31.15	25.9	34.5			
31.45	25.3	34.6		0.26	0.05
32.15	25.6	34.9			
32.45	25.7	35.1			
33.15	24.7	34.0			
33.45	25.1	35.6			
34.15	24.9	35.7			
34.45	23.0	33.8		0.26	0.05

Time (hrs)	Ca (mg L^{-1})	Ni (mg L^{-1})	pH	δ^{60}Ni	2σ
35.15	24.0	36.4			
35.45	24.5	36.2			
36.15	24.8	36.0	7.8		
36.45	24.6	36.0			
37.15	24.7	36.3			
37.45	24.8	36.3			
38.15	24.6	36.2			
38.45	24.6	36.6			
39.15	23.7	35.9			
39.45	24.6	36.7			
40.15	24.0	36.9			
40.45	24.5	37.1			
41.15	24.2	37.2			
41.45	24.3	37.3			
42.15	24.2	37.1			
42.45	24.4	37.4			
43.15	24.1	37.3			
43.45	24.2	37.6			
44.15	24.1	37.8			
44.45	23.8	37.6			
45.15	24.0	37.9			
45.45	23.7	37.8			
46.15	23.6	38.1			
46.45	24.1	38.3			
47.15	23.7	38.2		0.24	0.05
47.45	23.9	38.2			
48.15	23.5	37.6			
48.45	23.8	38.4			
49.15	23.7	38.4			
49.45	23.3	38.4			
50.15	23.4	38.5			
50.45	23.6	38.9			
51.15	23.8	39.1			
51.45	23.7	38.7		0.23	0.05
52.15	23.9	39.4			
53.15	23.8	39.5			
54.15	23.9	39.5			

Time (hrs)	Ca (mg L^{-1})	Ni (mg L^{-1})	pH	δ^{60}Ni	2σ
55.15	23.9	39.5			
56.15	23.9	40.0	7.8		
57.15	23.8	40.4			
58.15	23.7	40.5		0.21	0.05
59.15	24.0	40.7			
60.15	23.7	41.2			
61.15	23.5	41.5			
62.15	23.1	41.6			
63.15	22.7	42.0			
64.15	23.6	42.4			
65.15	23.0	42.4			
66.15	24.1	42.7			
67.15	23.2	42.9			
68.15	23.4	43.5			
69.15	23.2	43.5			
70.15	23.2	44.4			
71.15	23.3	44.2			
72.15	23.9	44.4			
73.15	23.2	44.8			
74.15	23.2	45.5		0.18	0.05
75.15	22.9	45.9			
76.15	23.3	46.3			
77.15	22.9	46.9			
78.15	22.7	47.0	7.8		
79.15	23.0	46.8			
80.15	23.1	47.0			
81.15	23.0	46.8			
82.15	23.0	47.2		0.11	0.05
83.15	23.0	46.9			
84.15	23.0	47.3			

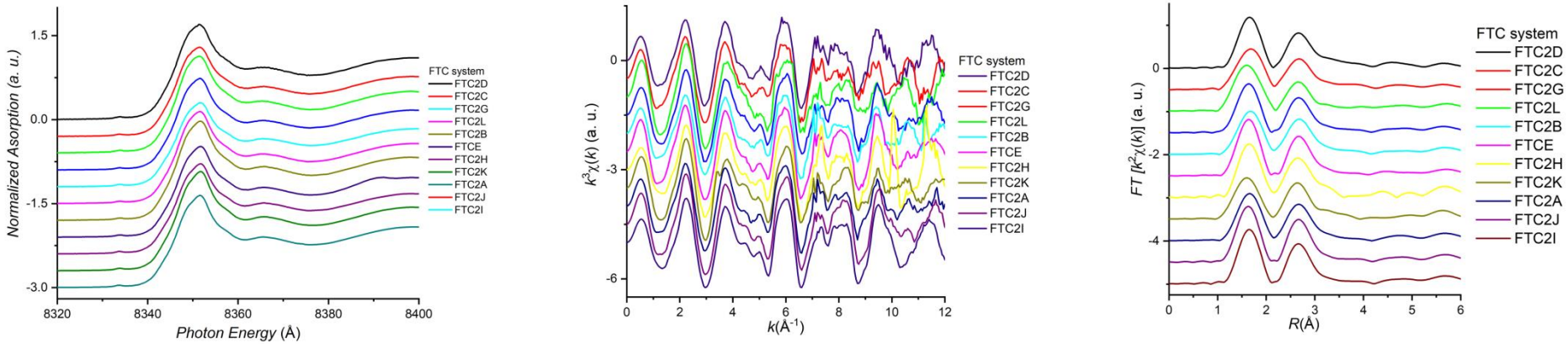

Figure S4.1: Experimental data of the 11 detected position: XANES (left), EXAFS in k space (middle), and EXAFS in R space (right) reveal no significant difference in XAFS across the FTC system.

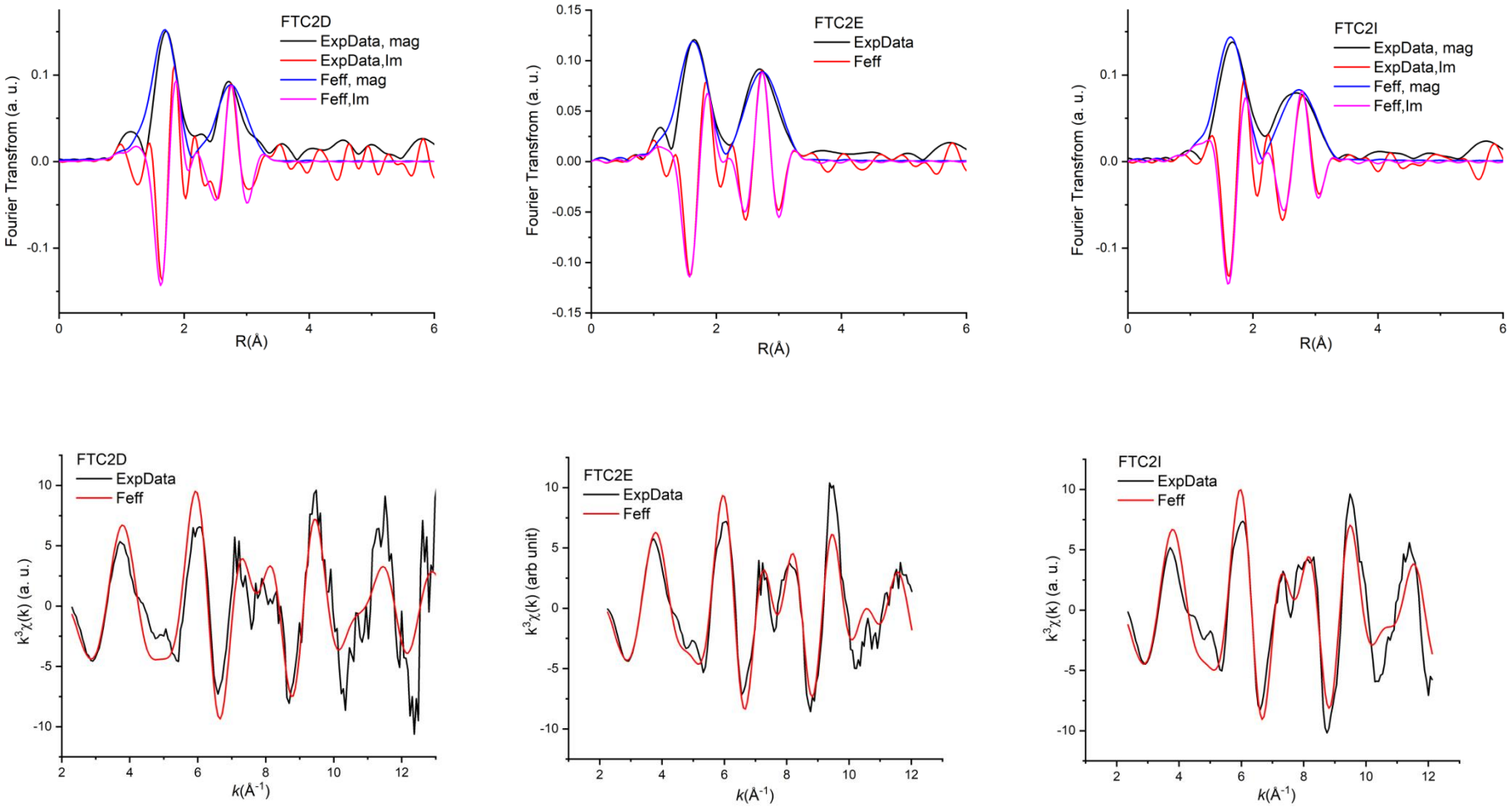

Figure S4.2: Top: comparison between ExpData vs Feff modeling in both magnitude of the Fourier transform (FT) and the imaginary part of the FT for data sets FTC2D, FTC2E, and FTC2I, which represent the FTC detected positions displaying the highest, the medium, and the lowest Ni concentration, respectively. Bottom: comparison in k space between ExpData vs Feff modeling based on the parameters from R space curve fitting for the same data sets.

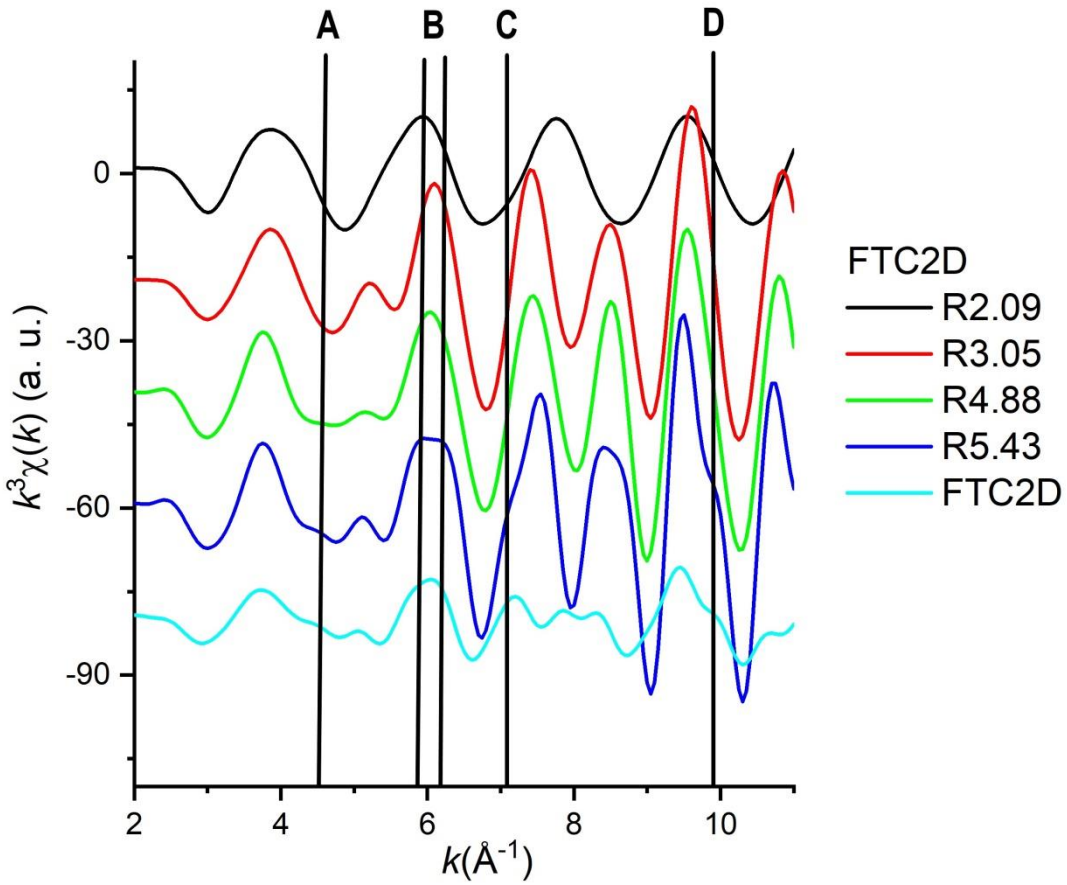

Figure S4.3: Feff modeling results for different theophrastite particle sizes (R of 2.09, 3.05, 4.88, and 5.43Å, respectively) compared to the FTC2D FT filtered ExpData (FT window=2.5-14.4 Å^{-1}; Backward FT window=1-6 Å). The features "A", "C", "D", and the splitting of "B" are resolved only when R reaches 5.43 Å, suggesting theophrastite particles have a thickness of, at least, 1 nm.

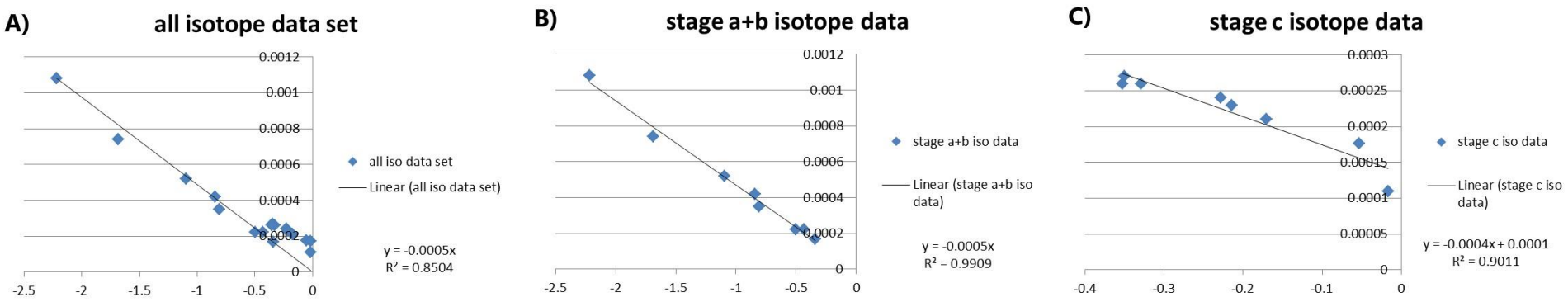

Figure S4.4: A) Linear regression including all FTC isotope data (ε = −0.5‰; R^2=0.85); B) Linear regression including FTC stages a and b isotope data (ε = −0.5‰; R^2=0.99); C) Linear regression including FTC stage c isotope data (ε = −0.4‰; R^2=0.90). Stage c isotope data regression line was not forced to intersect the origin (input solution values).

APPENDIX D

SUPPORTING INFORMATION FOR CHAPTER 5

Table S5.1: Pore-water results.

Depth (m)	pH	Eh (mV)	Ni ($mg\ L^{-1}$)	Fe ($mg\ L^{-1}$)	Al ($mg\ L^{-1}$)	SO_4 ($mg\ L^{-1}$)	Mg ($mg\ L^{-}$)	K ($mg\ L^{-1}$)	$\delta^{60}Ni$ (‰)	2σ
0.17	4.1	569	13.8	0.39	118	3808	505	4.8	0.66	0.09
0.19	3.9	373	9.5	1.5	122	2833	294	4.1	/	/
0.54	3.6	363	7.7	9	838	6229	106	3.6	-0.46	0.05
0.86	3.7	501	579	650	2809	20936	738	49.5	-0.51	0.09
0.86	3.2	349	289	1713	1566	16560	711	102	-0.47	0.05
1.18	3.8	289	93.7	931	473	6439	307	72.9	-0.42	0.05
1.19	3.9	481	433	578	300	5334	256	60.9	-1.48	0.05
1.53	4.2	485	196	240	81.9	3147	213	40.5	-1.92	0.05
1.88	4.6	378	151	2300	21.2	7524	475	49.2	-0.34	0.05
2.24	5.1	369	90.4	1444	6.2	4803	450	92.2	-0.77	0.05
2.55	4.4	206	48.8	474	5.5	3175	259	65.7	0.18	0.05
2.83	5.2	207	16.3	1350	4.3	4696	255	52.3	0.1	0.06
3.11	4.1	206	9.3	2209	4.5	7679	494	91.7	2.29	0.06

Table S5.0.1: Tailings solid material results.

Sample name	Depth (m)	Ni mg Kg^{-1}	S (wt %)	C (wt %)
C1-1	0.06	183	0.69	0.02
C1-2	0.17	177	0.58	0.02
C1-3	0.28	181	0.60	0.02
C1-4	0.39	232	0.66	0.03
C1-5	0.50	219	0.99	0.04
C1-6	0.61	186	0.81	0.03
C1-7	0.72	1473	4.03	0.04
C1-8	0.83	674	1.61	0.02
C1-9	0.94	1031	3.74	0.02
C1-10	1.04	1068	3.91	0.02
C1-11	1.15	1065	3.53	0.02
C2-1	1.26	979	1.53	0.02
C2-2	1.36	1539	3.24	0.01
C2-3	1.46	971	3.36	0.01
C2-4	1.56	720	1.68	0.02
C2-5	1.66	1509	2.05	0.02
C2-6	1.78	5007	5.35	0.04
C2-7	1.93	1485	0.57	0.06
C2-8	2.08	2358	1.46	0.07
C2-9	2.21	1061	1.29	0.02
C2-10	2.32	589	0.72	0.03

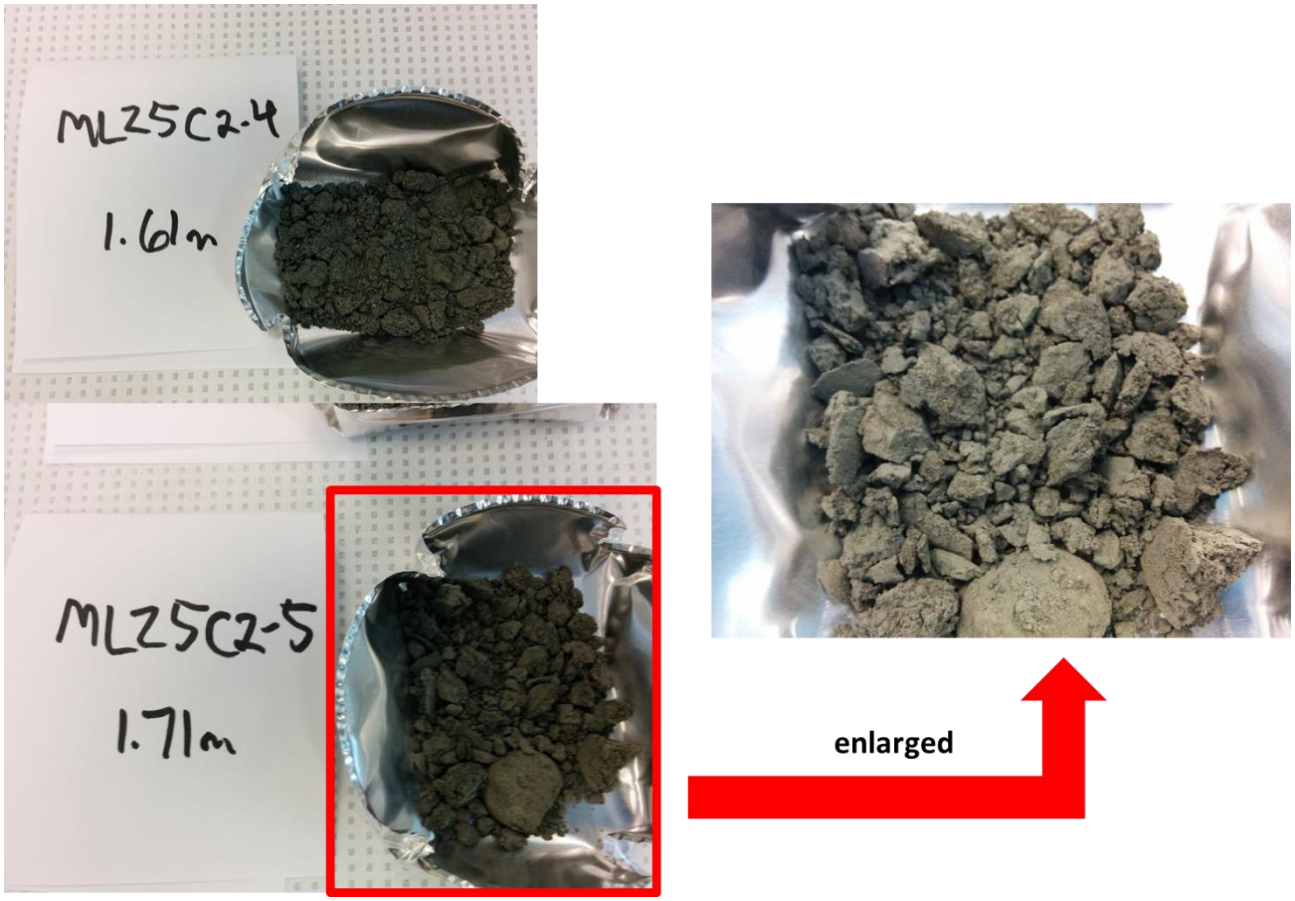

Figure S5.1: Photos of tailings samples collected from 1.61 and 1.71 m bgs, respectively. The sample located at 1.71 m bgs shows a finer grain texture compared to the one located at 1.61 m bgs.

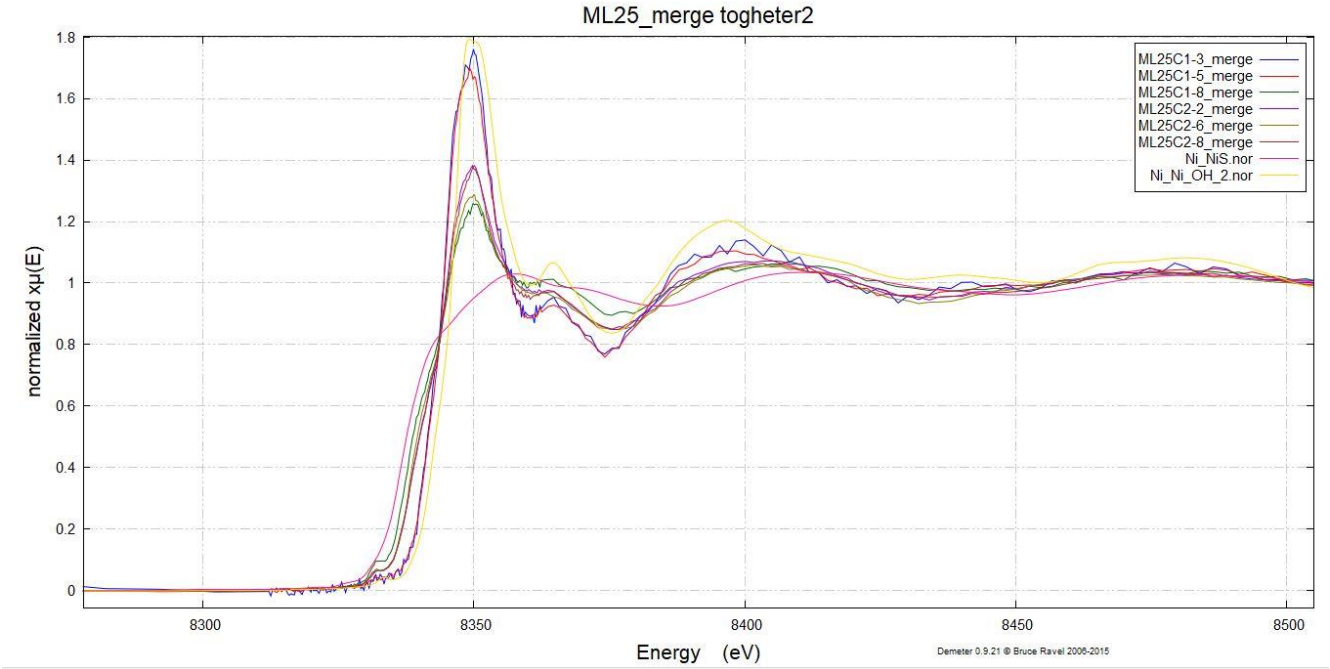

Figure S5.2: : Comparison between Ni K-edge spectra from Ni standards (NiS and $Ni(OH)_2$) and Ni K-edge spectra from tailings samples (C1-3, depth 0.28 m bgs; C1-5, depth 0.50 m bgs; C1-8, depth 0.83 m bgs; C2-2, depth 1.36 m bgs; C2-6, depth 1.78 m bgs; C2-8, depth 2.08 m bgs).

Figure S5.3: Photo of tailings samples collected from the upper part (from 1.18 to 1.36 m bgs) of the paleo-oxidized layer.